

## **ABSTRACT**

Ji, Xiang. Laser Interference Lithography for Fabrication of Gas Sensors. (Under the direction of Dr. John F. Muth).

The performance of metal oxide gas sensors is strongly connected to the material quality and microstructure of the metal oxide, with the device often heated to operating temperatures by an external thin film resistor. In this thesis, Laser Interference Lithography is explored as a way to pattern nanowire metal oxide gas sensors. This has several interesting implications.

- 1) Self-heating of the nanowires can potentially reduce the power consumption of the sensor
- 2) Compared to a flat metal oxide thin film the available surface area can be significantly increased improving sensitivity.

A laser interference lithography process was developed that uses a 355nm, 100mW ultraviolet laser. Features with length scales ranging from 125nm to 2 microns were produced as correspond to interference periods of 250nm to 4 microns.

To understand the laser interference lithography process an analytical model for a Lloyd's mirror experiment was developed and compared to Finite Difference Time Domain (FDTD) numerical simulation, allowing the period, and electric field distribution to be predicted as a function of beam angles and polarizations.

Experimentally the laser interference lithography was implemented with glass, silicon and ZnO thin film coated substrates allowing ZnO nanowires to be patterned. Varying the experimental configuration features ranging between 125nm to 2 microns were produced.

A gas sensor fabrication process was developed that allowed these patterns to be placed on low thermal conductivity silicon nitride membranes, or on interdigitated metal contacts. Preliminary results indicate that self-heating effects can be observed, as current passes through 1  $\mu\text{m}$  (2  $\mu\text{m}$  periods) ZnO wire produced by laser interference lithography and that the wires show photocatalytic response at room temperatures to gases when exposed to UV light, and that when heated by an external heater.

© Copyright 2013 by Xiang Ji

All Rights Reserved

# Laser Interference Lithography for Fabrication of Gas Sensors

by  
Xiang Ji

A thesis submitted to the Graduate Faculty of  
North Carolina State University  
in partial fulfillment of the  
requirements for the degree of  
Master of Science

Material Science and Engineering

Raleigh, North Carolina

2013

APPROVED BY:

---

Dr. John F. Muth  
Co - Chair

---

Dr. C. Lew Reynolds Jr.  
Co - Chair

---

Dr. Michael Kudenov

---

Dr. Jon-Paul Maria

## **BIOGRAPHY**

Xiang Ji completed B.S. in physics with double B.S. degree in economics in 2011 from Peking University, China.

He continued his study in Material Science and Engineering from North Carolina State University. He has worked under the guidance of Dr. John Muth on laser interference lithography and its application since summer 2012.

Xiang enjoys fishing and likes to play with electronics. He has recently developed an interest in using Raspberry Pi for robots. He likes writing simulation codes.

## ACKNOWLEDGMENTS

I want to sincerely thank my advisor Dr. John Muth for giving me the opportunity and support to work with him. I had big trouble before joining this group which diminished my passion towards research. I am grateful to Dr. Muth for his great knowledge and kind support to his students. I regained my enthusiasm towards scientific research by working with him. I also learnt the optimistic and humorous attitude towards life from him which is more important than research.

I want to thank Dr. Lew Reynolds for offering me the opportunity to work as his TA and directions from material science perspective on my research.

I want to thank Dr. Michael Kudenov for his guidance of reflection calculation in this project and his precious code as reference.

I want to thank Dr. Jon-Paul Maria for being a member in the committee and providing CuO samples for our research on releasing nanowires (not included in this thesis).

I want to thank Joe Matthews, our lab manager, who has been a super help through the project. I want to thank him for training me with facilities, helping with experiments and not getting too mad when I messed things up.

I want to thank Dr. Michael Escuti for allowing me to use his lab and laser. All laser interference lithography was done using his laser. I could not have finished without his help. I want to thank Dr. Ravi Komanduri from Dr. Escuti's group for training me the use of the

UV laser, helping me with setting up optics and inspiring discussions. I want to thank Matthew Miskiewicz for his help and thoughtful discussions. I want to thank all students from Dr. Escuti's group for sharing their optic table and laser with me.

I want to thank Leandra Brickson for her countless help of deposition of oxide and works together on the project. It has been a real honor for me to work with her together during the last year.

I want to thank Dr. Mehmet Ozturk, Marcio Cerullo from NNF for allowing me to use NNF clean room and facilities. I want to thank Steven Mills from Dr. Veena Misra's group for letting us use their heater for our device testing. I want to thank Dr. Haojun Luo, Wencong Zhu, Kory Grey, Dr. Hongguo Zhang for their help with experiments. I want to thank people in 112 MRC for making my stay here comfortable and productive.

I want to thank Edna Deas from MSE department for her help in the process of achieving this master degree.

I want to thank my parents for their support ever since my first breath in this world. I want to thank my friend Dr. Liwen Zou for her help. I want to thank my girlfriend Sibeixia for her support.

## TABLE OF CONTENTS

LIST OF TABLES .....	viii
LIST OF FIGURES .....	ix
Chapter 1 Introduction .....	1
Chapter 2 Metal Oxide Gas Sensors .....	6
2.1 Sensing Mechanism .....	7
2.2 Nanostructured metal oxide and their novel applications .....	10
2.2.1 Gas Sensing in Thin Films .....	10
2.2.2 Benefit of “Nano” : Self-heating.....	17
2.2.3 Room Temperature Gas Sensing: Photoelectrocatalysis .....	22
2.2.4 Zinc Oxide .....	25
Chapter 3 Laser Interference Lithography .....	30
3.1 Theoretical background of two beam interference .....	30
3.1.1 Two symmetrically incident beams .....	31
3.1.2 Two asymmetrically incident beams .....	33
3.1.3 Vertical standing wave caused by reflection .....	36
3.2 Lloyd’s Mirror Interferometer .....	40

3.3 Reflection Calculation and Anti-reflection Coating .....	42
3.3.1 The Importance of Reflection .....	42
3.3.2 Effective Index Methods for Reflection Coefficient Calculation .....	43
3.3.3 Reflection Calculation of an Assembly of Thin Films .....	49
3.4 Field Distribution .....	62
3.4.1 FDTD Calculation Method .....	63
3.4.2 Theoretical Field Distribution Calculation Method .....	69
3.4.3 Calculation Results .....	69
Chapter 4 Fabrication of ZnO Gas Sensor Using Laser Interference Lithography .....	78
4.1 Experiment Setup of laser interference lithography .....	78
4.2 Patterned photoresist with laser interference lithography .....	80
4.3 Process flow for metal oxide nanowire gas sensor fabrication .....	87
4.4 Mask Design of Metal Oxide Gas Sensor .....	94
4.4.1 Square contacts .....	95
4.4.2 Single digit contacts .....	97
4.4.3 Multiple interdigitated contacts .....	98
4.4.4 Silicon nitride membrane .....	100
4.4.5 Number system .....	100
4.5 Zinc Oxide Gas Sensor Prototype .....	101

4.6 Device characterization.....	106
4.6.1 Measurement system.....	106
4.6.2 Electrical properties of the sensor prototype .....	109
4.6.3 Qualitative gas sensing performance .....	115
Chapter 5 Conclusion.....	121
5.1 Conclusions.....	121
5.2 Suggestions for Future Work .....	122

## LIST OF TABLES

Table 3.1 Refractive Index list for Materials at 355nm wavelength.....	48
Table 4.1 Thickness of 1:1 (AZ5214E: PGMEA) volume ratio diluted photoresist of varied spin speed.....	85
Table 4.2 Thickness of ARC of varied spin speed.....	86
Table 4.3 Distance table of square contact .....	96
Table 4.4 Distance table of single digit contact.....	97
Table 4.5 Distance table of single digit contact.....	99
Table 4.6 Step height measurements .....	103

## LIST OF FIGURES

Figure 2.1 Three factors determining the response of semiconductor gas sensors.....	8
Figure 2.2 Resistance of device under selected partial pressures of oxygen as measured at various temperatures .....	9
Figure 2.3 Schematic model of the effect of the crystallite size on the sensitivity of metal-oxide gas sensors .....	10
Figure 2.4 Schematic representation of a compact sensing layer with geometry and energy band representations.....	12
Figure 2.5 Schematic representation of a porous sensing .....	14
Figure 2.6 Schematic representation of a porous sensing layer with geometry and surface energy band-case with necks between grains. ....	16
Figure 2.7(a) SEM image of a single multiwalled carbon nanotube electrothermal gas sensor. (b) Continuous resistance change versus time with a pressure control of every 10s in a nitrogen environment. ....	18
Figure 2.8 (a) Schematic representation of the device and its operational principle. (b) Optical images of the real device; (c) Theoretical evaluation of the partitioning of thermal losses .....	19
Figure 2.9 I-V measurements on SnO <sub>2</sub> nanobelt in oxygen environment.....	21

Figure 2.10 Diagram illustrating the UV-activated room temperature gas sensing mechanism .....	23
Figure 2.11 Response of RT-UV assisted ZnO sensor to different concentrations of ozone in the range of 70-10 ppb. ....	25
Figure 3.1 Interference between a pair of s-polarized incident plane waves .....	31
Figure 3.2 the horizontal and vertical components combine separately to create the desired horizontal standing wave and undesired vertical standing wave. ....	37
Figure 3.3 Lloyd's mirror interferometer setup .....	40
Figure 3.4 Geometric relationship between angles.....	41
Figure 3.5 coordinate system for measuring the E vectors of a plane wave reflected and refracted at a boundary .....	44
Figure 3.6 Angle dependence of reflection coefficient of light with 355nm wavelength upon different materials: gold, silicon and glass, a) p-polarized incident light, b) s-polarized incident light .....	49
Figure 3.7 Schematic of plane wave incident on an assembly of thin films .....	50
Figure 3.8 Reflection dependence of s and p polarized light on ARC thickness on silicon substrate. The incident angle is 45 degrees.....	53
Figure 3.9 Reflection dependence of s and p polarized light on ARC thickness on glass. The incident angle is 45 degrees .....	54

Figure 3.10 Reflection calculation of different ARC thickness on silicon substrate with different incident angle .....	55
Figure 3.11 Reflection calculation of different ARC thickness on glass substrate with different incident angle .....	57
Figure 3.12 Reflection calculation of different ZnO thickness on silicon substrate with different incident angle .....	58
Figure 3.13 Reflection calculation of different ZnO thickness on glass substrate with different incident angle .....	59
Figure 3.14 Reflection calculation of different ARC/ZnO thickness on amorphous silicon substrate with different incident angle .....	61
Figure 3.15 Yee unit cell .....	64
Figure 3.16 FDTD simulation setup .....	66
Figure 3.17 FDTD simulation time monitor (left) and index monitor (right) results .....	67
Figure 3.18 Reflection Coefficient of theoretical and FDTD calculation .....	68
Figure 3.19 Electric Field Distribution of s-polarized symmetric 45 ° incident light (left) theoretical calculation (right) FDTD result.....	70
Figure 3.20 Electric Field Distribution of p-polarized symmetric 45 ° incident light.....	71
Figure 3.21 Difference of field distribution between FDTD and theoretical calculation .....	73

Figure 4.1 Photographs of two laser interference lithography setups for (left) p polarized (right) s polarized.....	79
Figure 4.2 Photograph of power adjustment by using paper .....	80
Figure 4.3 Microscopic images of 1 dimensional lines with period of (top left) 482nm (top right) 620nm (bottom left) 976nm (bottom right) 1870nm .....	81
Figure 4.4 (a) Diffraction pattern of 1 inch sample (b) SEM image of 482nm period lines ..	82
Figure 4.5 Photograph of AFM.....	82
Figure 4.6 AFM images of photoresist nano-line with period of 263nm .....	83
Figure 4.7 AFM images of photoresist nano-line with period of (a) 1.29 $\mu$ m and (b) 1.94 $\mu$ m	84
Figure 4.8 Microscopic images of 2 dimensional bumps with period of 482nm .....	87
Figure 4.9 side view of device structures.....	88
Figure 4.10 Nanowire device fabrication process.....	88
Figure 4.11 Schematic of PLD system .....	89
Figure 4.12 Optical microscopic images of patterned ZnO film without removing photoresist .....	91
Figure 4.13 AFM images of etched ZnO film .....	91
Figure 4.14 AFM image of gold contact thickness.....	92
Figure 4.15 Silicon nitride membrane process flow .....	93

Figure 4.16 microscopic image of (a) silicon membrane (b) ZnO on top of silicon membrane with KOH residual .....	94
Figure 4.17 (a) Full mask design (b) Compact view of the mask .....	95
Figure 4.18 Schematic of a set of square contacts .....	96
Figure 4.19 Schematic of a set of single digit contacts.....	98
Figure 4.20 Schematic of a set of multiple interdigitated contacts.....	99
Figure 4.21 Number system on mask	101
Figure 4.22 Images of device chips with (a) 100nm and (b) 160nm thick ZnO, (c) ZnO thin film and (d) plain Silicon substrate.....	102
Figure 4.23 Microscopic images of square contact devices (a) devices with 20 $\mu$ m, 10 $\mu$ m distance (b) devices with 30 $\mu$ m, 50 $\mu$ m distance (c) SEM image of close up of interdigitated contact device (d) SEM image of fabricated ZnO wires.....	104
Figure 4.24 Microscope images of devices (a) Interdigitated contact width of 10 $\mu$ m. (b)Close up of 10 $\mu$ m interdigitated contact connected by ZnO nanowire pattern. (c) Single digit devices with 10 $\mu$ m (left) and 20 $\mu$ m (right) spacing. (d) Close up on single digit contacts showing .....	105
Figure 4.25 Photograph of (a) HP 4142B (b) Connection box .....	107
Figure 4.26 Photograph of probe station.....	108

Figure 4.27 Photograph of (a) bell jar system under vacuum (b) top view (c) side view of lifted bell jar for atmosphere gas sensing (d) GreenTech GT50 air purifier for ozone generation.....	109
Figure 4.28 I-V curve of sensor prototype (a) a resistor type behavior (b) diode type behavior .....	111
Figure 4.29 Resistance change between measurements .....	113
Figure 4.30 photograph of external heater .....	115
Figure 4.31 Gas sensing performance with heater under vacuum .....	116
Figure 4.32 Gas sensing performance with UV LED under vacuum with no heater .....	119
Figure 5.1 Vapor etching test results (a) HF vapor etch on glass substrate (b) (c) (d) HCl vapor etching on ZnO thin film .....	124

## Chapter 1 Introduction

A sensor is a device that transduces a signal from one form to another. A gas sensor is one of many kinds of sensors which are widely used in environmental protection, factory safety monitoring, health monitoring, etc. A gas sensor is a device which detects the presence and concentration of various gases within an area. Gas sensors come in two main types. Fixed type sensors are usually used for manufactories, plants or control rooms to monitor the process. Portable type sensors are usually used for environmental atmosphere monitoring, basically the environment surrounding a person.

The increasing demand in protection of each individual's health leads to the trend of real-time detection of a person's surrounding environment. To monitor the level of different toxic gases such as  $O_3$ ,  $NO_2$ ,  $NO_3$  and  $CO$ . requires the gas sensors to be small, portable, user-friendly, have low power consumption (long operation time), low cost and still maintain the necessary accuracy and stability.

According to its sensing mechanism, gas sensors can be divided into several categories: metal oxide based gas sensors, capacitance based gas sensors, acoustic wave based gas sensors, calorimetric gas sensors, FET gas sensors, optical gas sensors and electrochemical gas sensors.

Metal oxide sensors are also known as chemiresistors. The detection principle of resistive sensors is based on change of the resistance of a thin film upon adsorption of the gas

molecules on the surface of a semiconductor. In this project, we implement the use of laser interference lithography to form nanowires in metal oxide sensors, which introduces the advantage of large area, low cost, repeatable stability and is the first time used in the gas sensor area. Details of metal oxide sensors will be discussed in Chapter 2.

Notice that metal oxide gas sensors are not the only form. Several other forms of gas sensors and their sensing mechanisms are briefly introduced below. Since the process of using laser interference lithography to form nanowires has no connection with the sensor's operation mechanism, it is possible to employ Laser Lithography in the fabrication of other types of sensors too.

Capacitance based gas sensors measure the change in the dielectric constant of films between the electrodes as a function of the gas concentration. One of the most important advantages of a recently developed capacitance-based sensor [1] using  $\text{Ga}_2\text{O}_3$  nanowires is that such devices can operate at room temperature. These sensors also have a rapid and reversible response. A serious disadvantage for these sensors is the lack of chemical selectivity and a small response to common hydrocarbons such as acetone[2].

Acoustic wave based gas sensors use piezoelectric material either in the thin film form or in bulk form and measure the resonant frequency change caused by reaction with target gas as a sensing mechanism. Selectivity may rely on the sensing material or the response may be altered or enhanced by coating the propagation path with a chemically-selective material[3].

Calorimetric gas sensors use temperature changes resulting from the oxidation process on a catalytic element to measure the concentration of combustible species. These sensors burn combustible gases and the heat generated by combustion is balanced by a reduction in the electrical heating power, thus, the power consumption indicates the concentration of gas[4].

FET (field effect transistor) gas sensor devices are very attractive since they utilize one of the most common logical devices. The detection mechanism of FET devices with a catalytic sensing layer is often described in terms of the hydrogen response of dense catalytic metals and the ammonia response of porous catalytic metal films. Other gas molecules are divided into hydrogen containing, like hydrocarbons, and non-hydrogen containing gases like CO or NO/NO<sub>2</sub>. The hydrogen molecules dissociate on a catalytic metal surface such as Pd, Pt or Ir, and the hydrogen species diffuse quickly to the metal-oxide interface. They adsorb onto sites on the insulator surface forming special bounds, for example, OH groups[5].

Optical sensors have the advantage of a contact free, fast response that is suitable for flammable gas sensing and multi-gas detection by using multiple wavelengths, polarization and phases. The sensing mechanisms generally fall into three categories: spectroscopic techniques, ellipsometry, and surface plasmon resonance (SPR). The spectroscopic method uses the absorption/ emission/ scattering of a gas species at a suitable optical wavelength and thus is fast, accurate and stable. Ellipsometry is an optical, reflection-based technique which measures the polarization changes of reflection at oblique incidence into a sensing layer, usually a thin film. Surface plasmons, also known as surface plasmon polaritons, are the

surface electromagnetic waves that exist and propagate along the metal-insulator interface. To generate surface plasmon, several conditions need to match: the metal must have electrons in the conduction band that can resonant with certain wavelength of incident light, there is certain incident angle based on metal and insulator. In general, all it needs for SPR excitation is the match of momentum of the incident light and the supported SP mode of the interface. A change in the refractive index of the insulator can change the condition of SP mode, and such change can be used for detection.

Many efforts have been carried out on better understanding the sensing layers of these devices. Currently, most research is centered on conducting polymers; interesting results, in particular, have been obtained using polyimide films for humidity sensors[5-7]. However, the focus of this thesis will be on metal oxide sensors.

## REFERENCES

- [1] S. P. Arnold, S. M. Prokes, F. K. Perkins, and M. E. Zaghloul, "Design and performance of a simple, room-temperature  $\text{Ga}_2\text{O}_3$  nanowire gas sensor," *Applied Physics Letters*, vol. 95, p. 103102, 2009.
- [2] L. Mazeina, F. K. Perkins, V. M. Bermudez, S. P. Arnold, and S. M. Prokes, "Functionalized  $\text{Ga}_2\text{O}_3$  nanowires as active material in room temperature capacitance-based gas sensors," *Langmuir*, vol. 26, pp. 13722-6, Aug 17 2010.
- [3] A. Ricco, S. Martin, and T. Zipperian, "Surface acoustic wave gas sensor based on film conductivity changes," *Sensors and Actuators*, vol. 8, pp. 319-333, 1985.
- [4] P. N. Bartlett and S. Guerin, "A micromachined calorimetric gas sensor: an application of electrodeposited nanostructured palladium for the detection of combustible gases," *Analytical chemistry*, vol. 75, pp. 126-132, 2003.
- [5] E. Comini, G. Faglia, and G. Sberveglieri, "Electrical-based gas sensing," in *Solid State Gas Sensing*, ed: Springer, 2009, pp. 1-61.
- [6] L. Gu, Q.-A. Huang, and M. Qin, "A novel capacitive-type humidity sensor using CMOS fabrication technology," *Sensors and Actuators B: Chemical*, vol. 99, pp. 491-498, 2004.
- [7] P. Story, D. Galipeau, and R. Mileham, "A study of low-cost sensors for measuring low relative humidity," *Sensors and Actuators B: Chemical*, vol. 25, pp. 681-685, 1995.

## Chapter 2 Metal Oxide Gas Sensors

This thesis is about using laser interference lithography to fabricate metal oxide gas sensor for the following reasons:

- Formation of small dimension which increases the sensor's sensitivity and to obtain self-heating effect which can eliminate the need of an external heater
- Low cost, large area periodic structure formation where the period of the nanowire can be easily changed.
- Multiple exposures can lead to more complicated structures with 1D, 2D or 3D periodicity which is useful for future applications.

Metal oxide gas sensors have been researched for several decades. Due to their low cost in production, simplicity in use and the variety of gases they can detect, metal oxide gas sensors continue to be investigated with researchers aiming at higher sensitivity, lower working temperature, lower power consumption and better reliability. In 1991, Yamazoe demonstrated that the microstructure, e.g. grain size (diameter,  $D$ ) and depth of surface space-charge layer ( $L$ ) can affect the sensitivity by changing the transducer function[1]. The decrease in grain size makes the material almost depleted with only a few thermally activated carriers in the surface which leads to a great change in conductance when transition from a strongly not activated state to an activated state produced by target gas happens. Since then,

the challenge has become to prepare materials with small grain sizes while still obtain stability in performance for long periods of time.

A decrease in the dimension of structure will bring beneficial properties, such as an increase in the surface to volume ratio, and an increase in Joule heating effect which will possibly lead to self-heating effect when the size of the structure is designed to the proper range. In this chapter, the sensing mechanism will be discussed first, then the self-heating effect of one dimensional structure (nano-wires) will be introduced, and photo-electrocatalytic effect which is also used for room-temperature gas sensing will be covered.

## **2.1 Sensing Mechanism**

In order to fabricate and embed the advantages of nano-sized structure into the sensors, it is important to understand the sensing mechanism and influencing factors. Yamazoe and Shimano concluded that the sensing phenomenon can be reduced into a combination of three basic factors, receptor function (surface properties), transducer function (inter-grain properties) and utility (kinetic factor determined by diffusion and surface reaction) which are schematically illustrated in Figure 2.1[2].

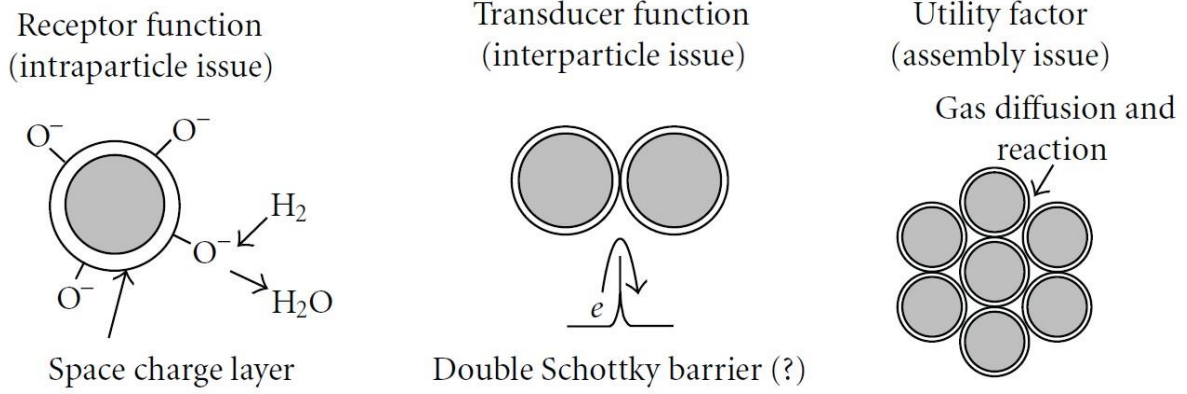
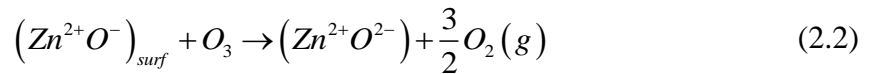


Figure 2.1 Three factors determining the response of semiconductor gas sensors [3]

The receptor function of the sensor is concerned with how each constituent crystal responds to the surrounding atmosphere containing oxygen and target gases[3]. A depletion layer is an insulating region formed by oxygen adsorbed on the crystal surface forming negatively charged species. The target gases interact by being adsorbed completely or reacting with the adsorbed oxygen. Two example reactions can be shown as below. Equation 2.1 is an example for a combustible gas, here  $H_2$ , which reacts with the adsorbed  $O^-$ . Equation 2.2 is an example for a more oxidizing gas, here  $O_3$  reacts with the adsorbed oxygen at the ZnO surface, which results in an increase in the depletion region[4]:



The transducer function depends on the details of how reaction with the receptor function is transferred to the sensor signal. In the chemiresistor case this is the change of the

resistance. A double Schottky barrier for transport of electrons through grain boundaries is assumed to be the reason of the resistance change. For a long time, the effect of the crystal size, which plays a very important role as mentioned before was ignored.

The tunneling effect is also suggested by experimental results showing that the resistance of spin-coated SnO<sub>2</sub> thin film stays almost constant in the temperature range of 150 °C to 400 °C as shown in Figure 2.2[5].

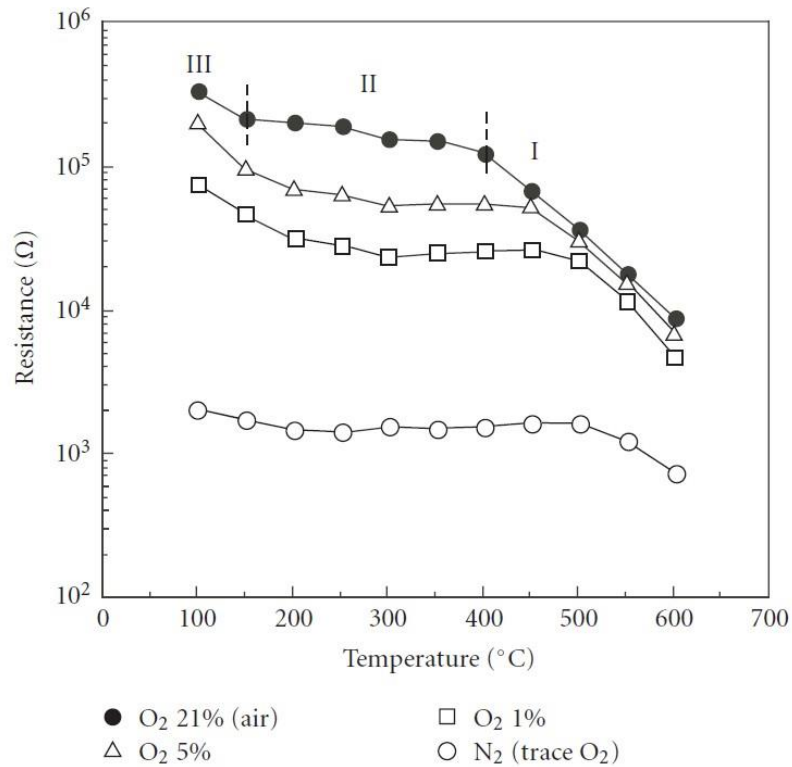


Figure 2.2 Resistance of device under selected partial pressures of oxygen as measured at various temperatures [5]

## 2.2 Nanostructured metal oxide and their novel applications

### 2.2.1 Gas Sensing in Thin Films

As pointed out by Yamazoe, the structural properties of the material (i.e. size, morphology) matter for the gas sensor's behavior. The effect of the grain size (diameter,  $D$ ) and depth of surface space-charge layer ( $L$ ) is shown below in Figure 2.3[6]. In order to incorporate these advantages into any gas sensor. The relatively small feature size within the device material needs to be emphasized.

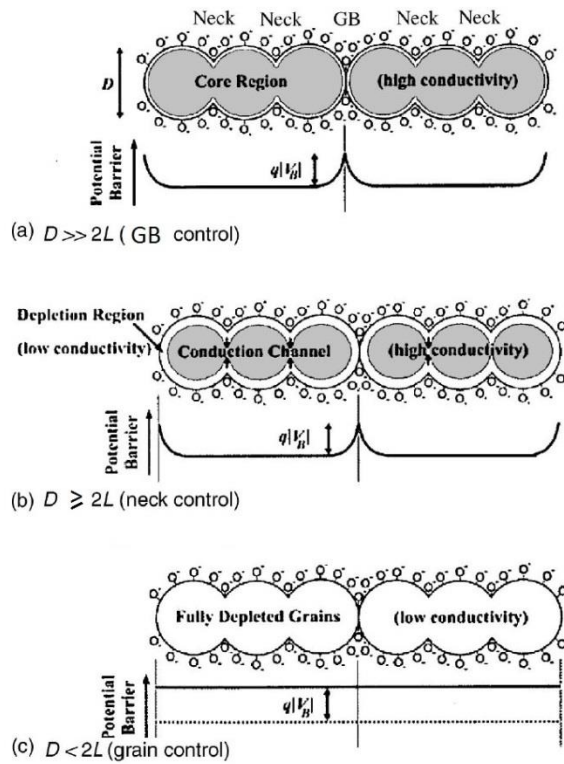


Figure 2.3 Schematic model of the effect of the crystallite size on the sensitivity of metal-oxide gas sensors [6]

Barsan and Weimar studied the conduction model of tin dioxide in 2001, and divided the sensing mechanism into two general categories, compact layer and porous layer[7]. The definition of compact layer and porous layer mainly differs on where the gas molecule can react with the sensing semiconducting film. In the compact layer, the reaction only happens on the film geometric surface. In porous layer, the reaction can also happen in the volume through the pores. Even though the difference between the two categories seems clear, it's hard to say for sure what certain deposition technique will lead the material into which category. A general idea provided by Barsen is that most of the techniques used for thin film deposition will lead to a compact layer whereas porous layers are characteristic to thick film techniques or other 'thick' techniques such as RGTO (Rheotaxial Growth and Thermal Oxidation). On the other hand, this definition seems tricky for certain material phases. For example, nano-crystalline materials which are usually in the thin film form can still provide a good interaction with the target gas within the material volume. Equipment parameters vary from lab to lab, therefore it is better to find out the specific deposition conditions and characterize the material for specific cases.

The depth of the reaction is almost the same for both cases which is controlled by the parameter Debye Length  $\lambda_D$  :

$$\lambda_D = \left( \frac{k\epsilon_0 k_B T}{e^2 N_0} \right)^{\frac{1}{2}} \quad (2.3)$$

where  $k_B$  is the Boltzmann constant,  $T$  is the absolute temperature,  $k$  is the relative static electric permittivity of the medium,  $\epsilon_0$  is the electric constant of the free space,  $e$  is the charge of an electron and  $N_0$  is the carrier density when potential is zero[8].

### A. Compact Layer

The thickness of the layer mainly determines whether it's partly depleted or completely depleted with the same material (thus same  $\lambda_D$ ). Figure 2.4 shows the geometry and energy band of a compact layer sensing film.

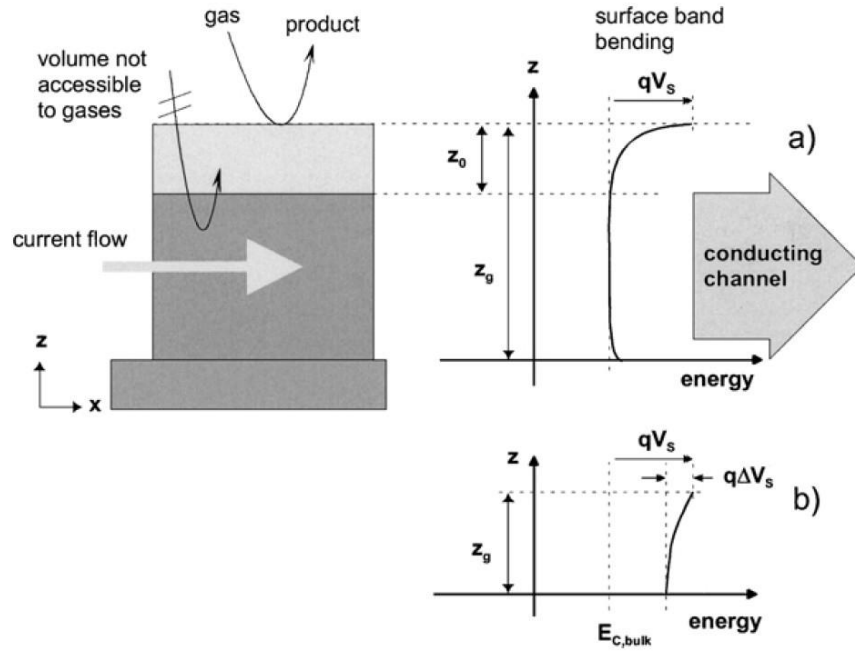


Figure 2.4 Schematic representation of a compact sensing layer with geometry and energy band representations;  $z_0$  is the thickness of the depleted surface layer;  $z_g$  is the layer thickness and  $qV_s$  is the band bending. (a) represents a partly depleted compact layer ("thick thicker"), (b) represents a completely depleted layer ("thinner") [8]

When the thickness of the layer is larger than the depleted depth ( $z_g > z_0$ ), the layer is partially depleted and the current flow is mainly in the bulk region ( $z_g - z_0$ ) as the conducting channel shown in the figure 2.4 illustrates. In this case, it has the same effect as two resistors in parallel: one representing the depleted region, one representing the rest of the bulk. A reducing gas interacts with the film, resulting in a decrease in the depletion region and an oxidizing gas tends to increase the depletion region. In order to have good sensitivity, one should properly control the film thickness such that for sensing a reducing gas, the film switches from completely depleted to partially depleted, resulting in a decrease in the resistance. For sensing an oxidizing gas, the film switches from partially depleted to completely depleted resulting in an increase in the resistance. Failure to switch between the two modes will end up with the film always staying in fully/partially depleted form exhibiting a small change in resistance whose results can be understood by the two parallel connected resistor-like film-gas interactions.

## **B. Porous Layer**

For the porous layer, the concept of being partially depleted and completely depleted still works, but needs a little modification so that this concept applies to the poly or nano crystalline grains here, which are the building blocks of the film. In a sense of building blocks, the connections between each block fall into two different new components: grain boundaries or necks. The grain boundary is the interface between two grains. The neck is the connection between two grains or even two particles which usually happens in the sintering

process. A neck connects two grains together and form them into one piece. For the schematic representation of necks, please refer to Figure 2.3 (a).

The discussion about the porous layer usually depends on the grain size: large grains ( $x_g > \lambda_D$ ) and small grains ( $x_g < \lambda_D$ ) and how large the depletion region is in relation to the grain size, as shown in Figure 2.5. It is important to consider the neck's effect as well.

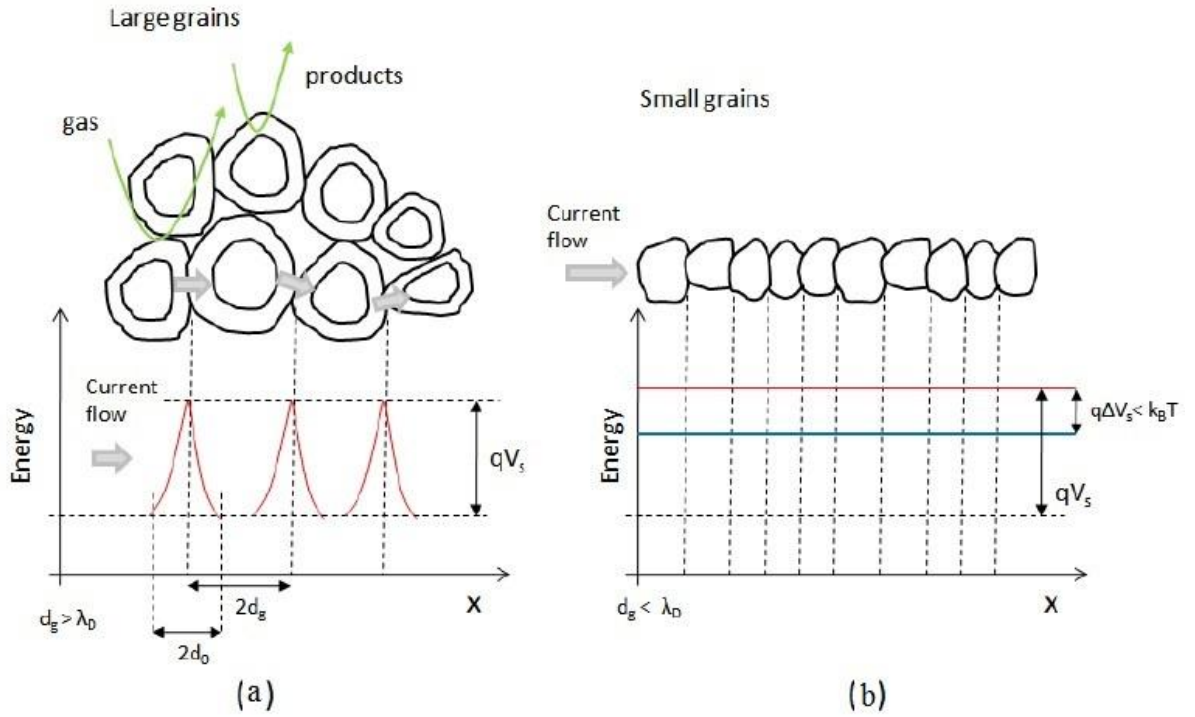


Figure 2.5 Schematic representation of a porous sensing structure. [7]

For large grains, if no necks are present, the contact region between grains is small enough that the carriers are only affected by one  $V_s$  when moving from one grain to the other, as shown in Figure 2.5 (a). The surface charge carrier density  $n_s$  is given by equation 2.4. [2]

$$n_s = n_b \exp(-qV_s / k_B T) \quad (2.4)$$

When necks are present in large grains, there are two cases to consider, as shown in Figure 2.6. If the depletion layer is small compared to the neck diameter, the effect is similar to the partly depleted case in a compact layer. When the neck is completely depleted and the thermal energy is not enough for the electron activation ( $q\Delta V_s > k_B T$ ), the carriers have a different barrier potential depending on its location (z value) which results in an average effective potential  $V_{s,average}$ . If the thermal energy is enough for electron activation ( $q\Delta V_s < k_B T$ ), the electrons will feel the same barrier potential ( $V_s$ ) again when passing from one barrier to another, similar to the previous case.

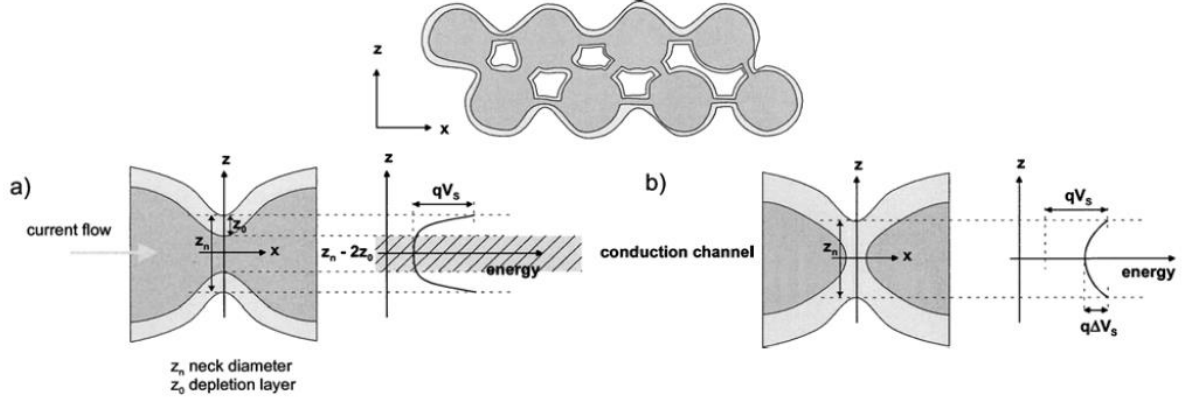


Figure 2.6 Schematic representation of a porous sensing layer with geometry and surface energy band-case with necks between grains. a) represents the case of only partly depleted necks whereas b) represents large grains where the neck contact is completely depleted [7]

For small grains, surface scattering may play a role in influencing the mobility, which depends on the relationship between the mean free path of electrons ( $\lambda$ ) and the dimension of the grains ( $2r$ ), using a sphere for simplicity.

When  $\lambda/(2r)$  is negligible, the scattering effect is negligible, and the conductance is proportional to the surface concentration of electrons  $n_s$ . When  $\lambda/(2r)$  is non-negligible, the mobility change needs to be considered, and the conductance is proportional to the surface concentration of electrons  $n_s$  multiplied with the respective mobility. Details of the calculations of the terms can be found in [7].

Similar with the case of large grains, the relationship between the activation energy and the Debye length is also important here,

$$\Delta E \sim k_B T (R / 2\lambda_D) \quad (2.5)$$

where  $R$  is the radius of the cylindrical filament produced by sintering small grains [2]. If  $\Delta E$  could be satisfied by thermal activation, then we have a homogeneous electron distribution in the filament and flat band conditions as shown in Figure 2.5 (b). For tin dioxide, it has been shown that with grain sizes lower than 50nm, complete carrier depletion happens inside the grains at almost all temperatures.

### **2.2.2 Benefit of “Nano” : Self-heating**

Besides the flat conduction band of small grains, switching between partially depleted and completely depleted thin films also benefits from reducing the dimension down to smaller sizes. One unique effect obtained by 1D nanostructures has been noticed as very useful in the application of gas sensing – self-heating.

Self-heating effects are not unfamiliar, since current flow through a resistor produces heat. Self heating effects depend on the following effects:

- a) Heat transfer to the surrounding atmosphere
- b) Heat transfer to the contacts connected to the nanowire
- c) The magnitude of the current and resistance

Kawano et al. reported an electrothermal effect in their suspended multiwalled carbon nanotube gas sensor [9]. They reported that both gas pressure and species can affect the heat-transfer process and resulted in the multiwalled carbon nanotube temperature changes and therefore resistance changes. Figure 2.7 (a) shows the scanning electron

microscope (SEM) image of their single 26 $\mu\text{m}$  long suspended nanotube device. The multiwalled carbon nanotube used in their calculation had an outer diameter of 30nm and an inner diameter of 10nm. Figure 2.7 (b) shows continuous resistance change of their device versus time with pressure change in a nitrogen environment which is also observed in our experiments shown in detail in the experimental results part.

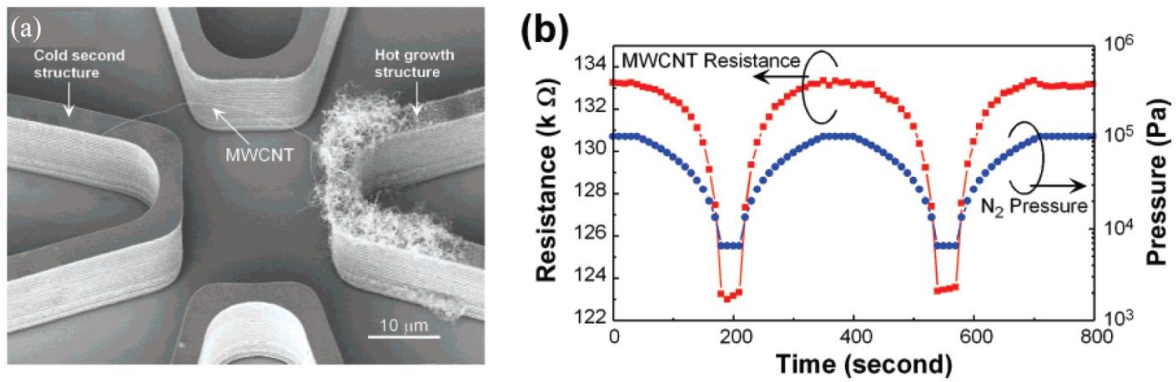


Figure 2.7(a) SEM image of a single multiwalled carbon nanotube electrothermal gas sensor. (b) Continuous resistance change versus time with a pressure control of every 10s in a nitrogen environment. No delay is observed, indicating a fast response time, which cannot be explained by previously reported gas sensing mechanisms. [9] Reported joule heating effect of nanowire silicon nanowires on top of  $\text{SiO}_2$  [10]

The idea of using the joule heating effect to warm up the nanowire by itself relies on winning the competition between heat source and loss. Strelcov et al. studied the detail of the self-heating effect on surface reactivity and gas sensing for metal oxide nanowire chemiresistors [11]. Even though the precise modeling of the temperature distribution requires numerical simulation, they provided a feasible method to evaluate the power of the

source and environment. Figure 2.8(a) shows the model setup. The joule power  $P_J$  dissipated in an n-type nanowire resistor can be estimated as [11]

$$P_J = IV \sim S n(T) e \mu V^2 / L \quad (2.6)$$

where  $S$  is the cross-sectional area of the conducting channel in the nanowire,  $e$  is the elementary charge,  $\mu$ ,  $n$  are the mobility and concentration of electrons in the conduction band and  $L$  is the length of the nanowire.

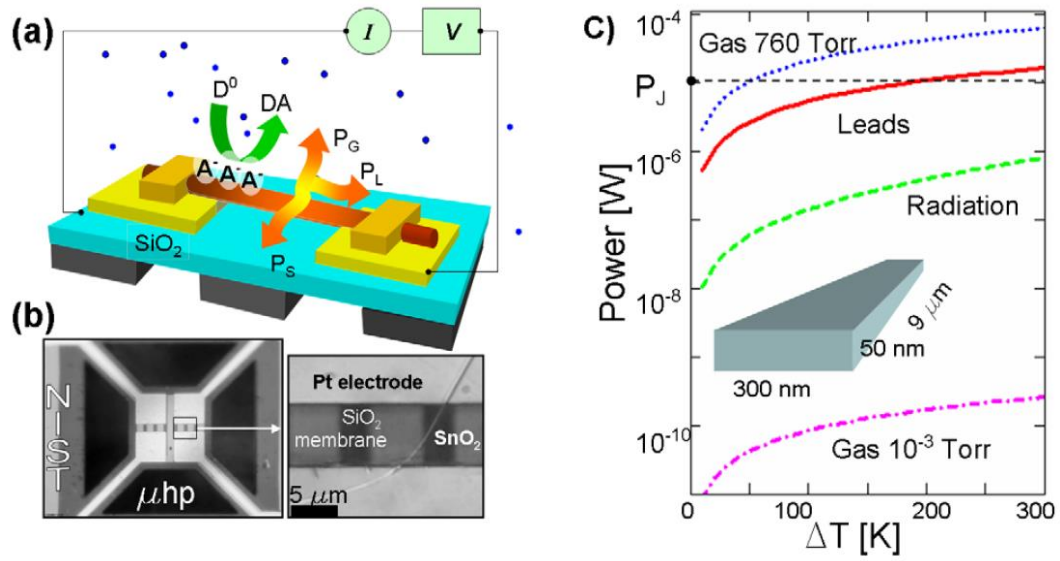


Figure 2.8 (a) Schematic representation of the device and its operational principle.  $P_G$ ,  $P_L$  and  $P_S$  are power losses to the gas surroundings, leads and radiation, respectively. D and A are donor and acceptor species. (b) Optical images of the real device; (c) Theoretical evaluation of the partitioning of thermal losses between different channels: metal leads, gas environment at 760 Torr and 10<sup>-3</sup> Torr, and radiation loss [11]

For a suspended nanostructure, heat loss due to metal leads:

$$P_L \sim 4S\kappa(T-T_0)/L \quad (2.7)$$

and environmental gas:

$$P_G \sim \alpha \sqrt{\frac{R}{T_0}} \left( \frac{P_1}{\sqrt{M_1}} + \frac{P_2}{\sqrt{M_2}} \right) (T-T_0) S^* \quad (2.8)$$

and via the radiation losses:

$$P_{rad} \sim \varepsilon \sigma S^* (T^4 + T^3 T_0 + T^2 T_0^2 + T T_0^3 - 4T_0^4) / 5 \quad (2.9)$$

where  $\kappa$  is thermal conductivity,  $\alpha \sim 1$  is a numerical factor,  $S^*$  is the surface area of the nanostructure,  $T$  is the temperature of the nanostructure in its center,  $T_0$  is the temperature of the environment,  $P_{1,2}$  and  $M_{1,2}$  are the partial pressures and molar masses of the gases, and  $R$ ,  $\sigma$  and  $\varepsilon$  are the universal gas constant, the Stefan-Boltzmann constant and the emissivity factor of the nanostructure, respectively [11]. It can be seen from Figure 2.8 (c) that the heat dissipation to environmental gas increases with the pressure change from vacuum ( $10^{-3}$  Torr) to atmospheric pressure (760 Torr) and the heat loss due to the metal lead is still dominant. In accordance with this estimation, for maximal used  $P_j \sim 10^{-5} W$ , the equilibrium state of the structure leads to a temperature 200 K above room temperature (as shown in the horizontal line in Figure 2.8 (c)).

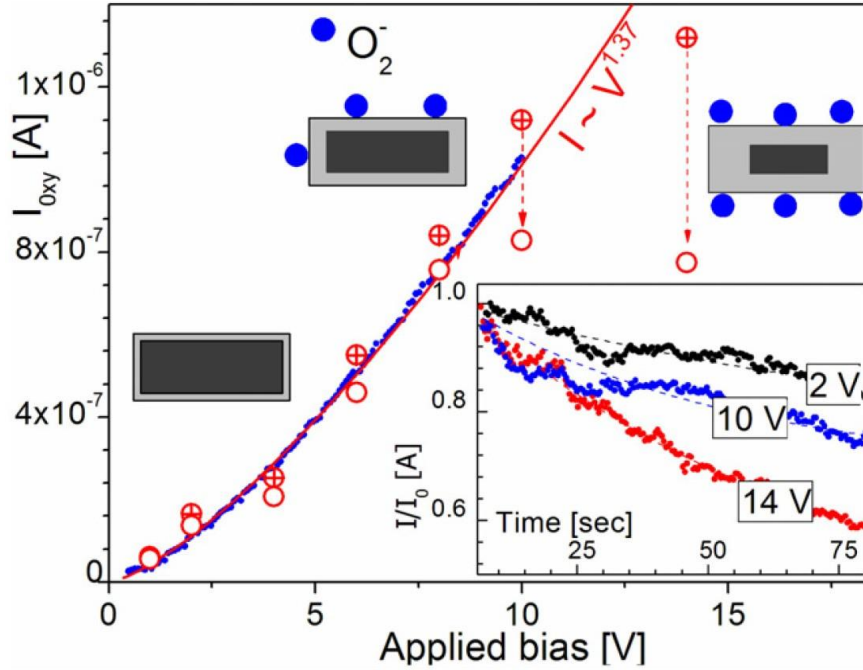


Figure 2.9 I-V measurements on SnO<sub>2</sub> nanobelt in oxygen environment. The blue dotted curve represents ‘fast’ voltage ramp with the dwell time 200 ms between the points. The red solid curve shows fitting of these data. Circles correspond to ‘slow’ I-V measurements where the voltage was set manually for gas sensing measurements. The crossed circles correspond to the initial value of the current in oxygen and the open ones to the current measured 75 s later. [11]

An interesting manifestation of the self-heating effect was observed by a delayed ‘slow’ IV curve measurement compared with a ‘fast’ measured IV curve, which shows a significant drop in current with the same input of voltage (kept constant) after 75s, which indicates an increase in the resistance as shown in Figure 2.9. They concluded this phenomenon to the slow oxygen ionosorption (at  $0.5 \cdot 10^{-4}$  Torr):  $O_{2(s)} + e^- \xrightleftharpoons{\tau} O_{2(s)}^-$  or  $O_{2(s)} + 2e^- \xrightleftharpoons{\tau} 2O_{(s)}^-$  which depletes the surface region of the nanostructure and is a thermally

activated process. The increase of conductance drops with bias voltage agrees with the self-heating hypothesis [11].

### **2.2.3 Room Temperature Gas Sensing: Photoelectrocatalysis**

Besides the self-heating effect, another approach towards room temperature metal oxide gas sensing is to use UV light to activate the sensing material free carriers and enable the surface reaction, which normally requires high temperatures ( $>300\text{ }^{\circ}\text{C}$ ) [12]. However, the high temperature also affects sensor's reliability and durability.

Comini et al. used UV light illumination on a  $\text{SnO}_2$  thin film gas sensor for  $\text{NO}_2$  detection. They reported a decrease in working temperature together with response time, recovery time and no poisoning effect. Gui et al. used UV light activation on a  $\text{TiO}_2$  doped  $\text{ZnO}$  thick film sensor to enable room temperature sensing [13].

Fan et al. studied the UV-activated room temperature gas sensing mechanism of polycrystalline  $\text{ZnO}$  in 2009 [14]. It is noticed that there are two processes caused by the UV illumination as shown in Figure 2.10:

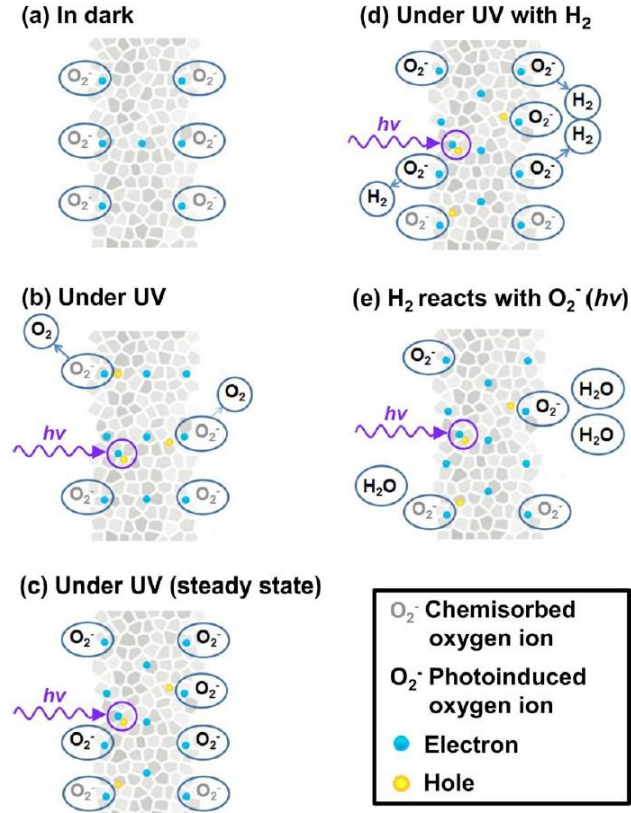
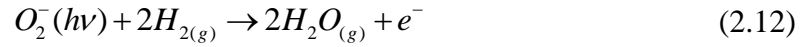


Figure 2.10 Diagram illustrating the UV-activated room temperature gas sensing mechanism [14]

- i. The photoinduced hole interacts with the chemisorbed oxygen ion ( $O_2^-$ ) which is thermally stable, causing the ion to desorb from the surface by the following reaction:



- ii. The ambient oxygen reacts with the photoinduced electrons to create new oxygen ions ( $O_2^-(h\nu)$ ), which are very active and can easily participate in the redox reaction. These ions are bonded to the ZnO surface very weakly and can be easily removed simply by turning off the UV light, yielding quick recovery. The redox reaction in the case of room temperature  $H_2$  sensing is as following:



Based on the quick reaction of the photoinduced free electrons, people have used UV light for sensor's recovery in room temperature gas sensing. Carotta et al. used a UV LED to assist ZnO thick film ozone sensing and was able to push the response limit down to 10 ppb (parts per billion) at room temperature as shown in Figure 2.11 [15].

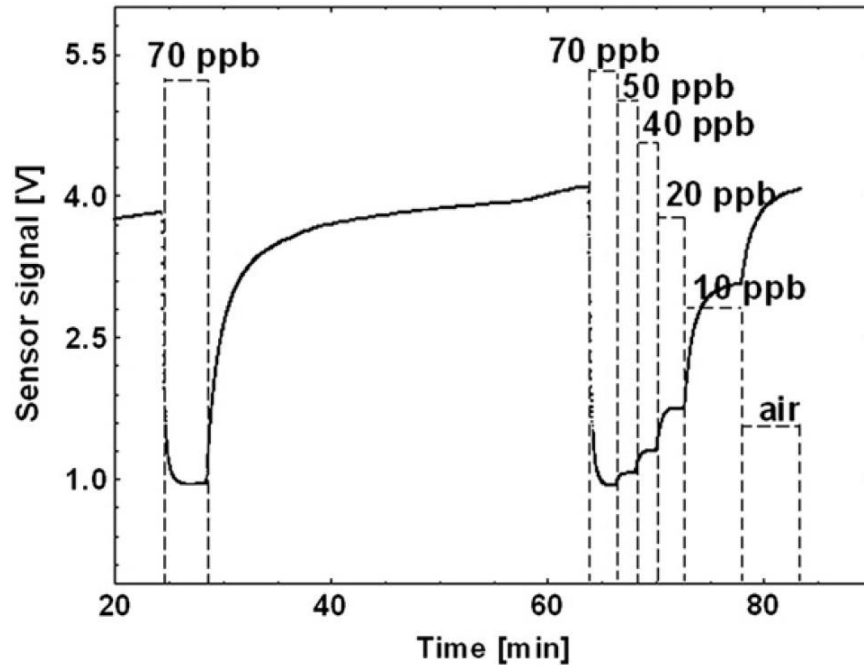


Figure 2.11 Response of RT-UV assisted ZnO sensor to different concentrations of ozone in the range of 70-10 ppb. [15]

Their work is remarkable, since it's difficult to detect such a low ozone concentration (ranges mostly found in papers are among ppm (parts per million)) with a metal oxide based gas sensor.

#### 2.2.4 Zinc Oxide

Zinc oxide possesses a variety of nanostructures: nanowires, nanobelts, nanorings, nanorods, nanocombs and other novel architectures [16, 17]. Zinc oxide belongs to the wurtzite family, which is an important material for applications in optoelectronics, lasing,

and piezoelectricity. Zinc oxide has a wide band gap (3.37eV) and exhibits near ultraviolet emission [2]. With its large variety of structures and wide range of functions, zinc oxide has attracted a lot of attention in many research fields. In the sensing world, it was the first sensing material used but was abandoned afterwards. Recent studies of its ability to form in different small-scale structures (self-heating), interact with many different target gases and UV activation (photo-electrocatalytic) have brought it back to be the most popular studied material again. Since our group has a long history and good understanding of ZnO, this material is chosen for the first generation devices [18-20]. When the process is mature, it is possible to use other materials such as TiO<sub>2</sub>, IZGO, etc.

## REFERENCES

- [1] N. Yamazoe, "New approaches for improving semiconductor gas sensors," *Sensors and Actuators B: Chemical*, vol. 5, pp. 7-19, 1991.
- [2] D. K. Aswal and S. K. Gupta, *Science and technology of chemiresistor gas sensors*: Nova Publishers, 2007.
- [3] N. Yamazoe and K. Shimanoe, "Receptor function and response of semiconductor gas sensor," *Journal of Sensors*, vol. 2009, 2009.
- [4] R. Martins, E. Fortunato, P. Nunes, I. Ferreira, A. Marques, M. Bender, N. Katsarakis, V. Cimalla, and G. Kiriakidis, "Zinc oxide as an ozone sensor," *Journal of Applied Physics*, vol. 96, pp. 1398-1408, 2004.
- [5] N. Yamazoe, K. Shimanoe, and C. Sawada, "Contribution of electron tunneling transport in semiconductor gas sensor," *Thin Solid Films*, vol. 515, pp. 8302-8309, 2007.
- [6] A. Rothschild and Y. Komem, "The effect of grain size on the sensitivity of nanocrystalline metal-oxide gas sensors," *Journal of Applied Physics*, vol. 95, pp. 6374-6380, 2004.
- [7] N. Barsan and U. Weimar, "Conduction model of metal oxide gas sensors," *Journal of Electroceramics*, vol. 7, pp. 143-167, 2001.
- [8] O. Lupan, V. Ursaki, G. Chai, L. Chow, G. Emelchenko, I. Tiginyanu, A. Gruzintsev, and A. Redkin, "Selective hydrogen gas nanosensor using individual ZnO nanowire

- with fast response at room temperature," *Sensors and Actuators B: Chemical*, vol. 144, pp. 56-66, 2010.
- [9] T. Kawano, H. C. Chiamori, M. Suter, Q. Zhou, B. D. Sosnowchik, and L. Lin, "An electrothermal carbon nanotube gas sensor," *Nano letters*, vol. 7, pp. 3686-3690, 2007.
  - [10] I. Park, Z. Li, A. P. Pisano, and R. S. Williams, "Selective surface functionalization of silicon nanowires via nanoscale Joule heating," *Nano letters*, vol. 7, pp. 3106-3111, 2007.
  - [11] E. Strelcov, S. Dmitriev, B. Button, J. Cothren, V. Sysoev, and A. Kolmakov, "Evidence of the self-heating effect on surface reactivity and gas sensing of metal oxide nanowire chemiresistors," *Nanotechnology*, vol. 19, p. 355502, 2008.
  - [12] E. Comini, G. Faglia, and G. Sberveglieri, "UV light activation of tin oxide thin films for NO<sub>2</sub> sensing at low temperatures," *Sensors and Actuators B: Chemical*, vol. 78, pp. 73-77, 2001.
  - [13] Y. Gui, S. Li, J. Xu, and C. Li, "Study on TiO<sub>2</sub>-doped ZnO thick film gas sensors enhanced by UV light at room temperature," *Microelectronics Journal*, vol. 39, pp. 1120-1125, 2008.
  - [14] S.-W. Fan, A. K. Srivastava, and V. P. Dravid, "UV-activated room-temperature gas sensing mechanism of polycrystalline ZnO," *Applied Physics Letters*, vol. 95, pp. 142106-142106-3, 2009.
  - [15] M. Carotta, A. Cervi, A. Fioravanti, S. Gherardi, A. Giberti, B. Vendemiati, D. Vincenzi, and M. Sacerdoti, "A novel ozone detection at room temperature through

- UV-LED-assisted ZnO thick film sensors," *Thin Solid Films*, vol. 520, pp. 939-946, 2011.
- [16] Z. R. Tian, J. A. Voigt, J. Liu, B. McKenzie, M. J. Mcdermott, M. A. Rodriguez, H. Konishi, and H. Xu, "Complex and oriented ZnO nanostructures," *Nature materials*, vol. 2, pp. 821-826, 2003.
- [17] Z. L. Wang, "Nanostructures of zinc oxide," *Materials today*, vol. 7, pp. 26-33, 2004.
- [18] J. Narayan, A. K. Sharma, A. Kvit, C. Jin, J. Muth, and O. Holland, "Novel cubic Zn<sub>x</sub> Mg<sub>1-x</sub> O epitaxial heterostructures on Si (100) substrates," *Solid state communications*, vol. 121, pp. 9-13, 2001.
- [19] A. Suresh and J. Muth, "Bias stress stability of indium gallium zinc oxide channel based transparent thin film transistors," *Applied Physics Letters*, vol. 92, pp. 033502-033502-3, 2008.
- [20] J. Muth, R. Kolbas, A. Sharma, S. Oktyabrsky, and J. Narayan, "Excitonic structure and absorption coefficient measurements of ZnO single crystal epitaxial films deposited by pulsed laser deposition," *Journal of Applied Physics*, vol. 85, pp. 7884-7887, 1999.

## **Chapter 3 Laser Interference Lithography**

Maskless laser interference lithography (LIL) allows fast and large area periodical sub-micron structures to be patterned with simple equipment. The principle is based on the interference of two coherent light beams to form a horizontal standing wave for a grating pattern which can be recorded on photo-resist. It is convenient to use this method for forming different dimensions of sub-micron/nano patterns by tuning the angles between the incident beams.

### **3.1 Theoretical background of two beam interference**

In this section, the theoretical background of two beam laser interference lithography is explored with both symmetric and asymmetric incident beams. Then the formation of undesired vertical standing waves is explored. Three different reflection calculation methods are then introduced and used for structure optimization both in the use of additional Anti-reflection coatings and ZnO thin films acting as an interfering anti-reflection coating without an additional layer.

### 3.1.1 Two symmetrically incident beams

A schematic of two s-polarized beams interfering at the surface of photoresist is shown in Figure 3.1 [1].

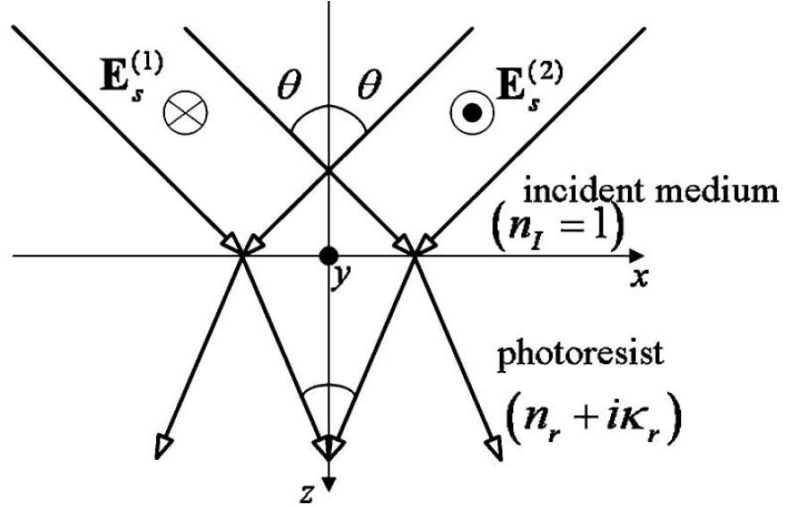


Figure 3.1 Interference between a pair of s-polarized incident plane waves [1]

By assuming the two beams incident at the same angle  $\theta$ , the electric fields of two waves can be written as [1]:

$$E_s^{(1)} = \left| \tau_s^{(l,r)} \right| A_1 \cos \left( -k_r \sin \theta_r' x + k_r \cos \theta_r' z - \frac{2\pi}{T} t + \delta_1 + \chi_s \right) \exp \left( \frac{-k \kappa_r' z}{\cos \theta_r'} \right) \mathbf{e}_y \quad (3.1)$$

$$E_s^{(2)} = - \left| \tau_s^{(l,r)} \right| A_2 \cos \left( k_r \sin \theta_r' x + k_r \cos \theta_r' z - \frac{2\pi}{T} t + \delta_2 + \chi_s \right) \exp \left( \frac{-k \kappa_r' z}{\cos \theta_r'} \right) \mathbf{e}_y \quad (3.2)$$

Where  $T$  is the inverse of the source frequency,  $|\tau_s^{(l,r)}|$  is the amplitude factor of the transmission coefficient for the s polarized incident electric field,  $\theta_r'$  is the angle of refraction, and  $\chi_s$  is the corresponding induced phase shift resulting from the transmission.

The corresponding time averaged intensity is given as:

$$I \propto \left\langle \left( E_s^{(1)} + E_s^{(2)} \right) \bullet \left( E_s^{(1)} + E_s^{(2)} \right)^* \right\rangle$$

$$= |\tau_s^{(l,r)}|^2 \left\{ \frac{A_1^2}{2} + \frac{A_2^2}{2} - A_1 A_2 \cos(2k \sin \theta x - \delta_{1,2}) \right\} \exp \left( \frac{-2k \kappa_r z}{\cos \theta_r'} \right) \quad (3.3)$$

It can be seen from Equation 3.3, that the periodic pattern is along the x axis and has a sinusoidal intensity distribution. The period  $\Lambda$  along x axis is then calculated as

$$\Lambda = \frac{2\pi}{2k \sin \theta} = \frac{\lambda}{2 \sin \theta} \quad (3.4)$$

For p polarized incident light, the electric fields are:

$$E_p^{(1)} = |\tau_p^{(l,r)}| A_1 \cos \left( -k_r \sin \theta_r' x + k_r \cos \theta_r' z - \frac{2\pi}{T} t + \delta_1 + \chi_p \right)$$

$$\exp \left( \frac{-k \kappa_r z}{\cos \theta_r'} \right) (-\cos \theta_r' \mathbf{e}_x + \sin \theta_r' \mathbf{e}_z) \quad (3.5)$$

$$E_p^{(2)} = |\tau_p^{(l,r)}| A_2 \cos \left( k_r \sin \theta_r' x + k_r \cos \theta_r' z - \frac{2\pi}{T} t + \delta_2 + \chi_p \right)$$

$$\exp \left( \frac{-k \kappa_r z}{\cos \theta_r'} \right) (-\cos \theta_r' \mathbf{e}_x - \sin \theta_r' \mathbf{e}_z) \quad (3.6)$$

Similarly, the time averaged intensity is then given as:

$$\begin{aligned}
 I &\propto \left\langle \left( E_p^{(1)} + E_p^{(2)} \right) \bullet \left( E_p^{(1)} + E_p^{(2)} \right)^* \right\rangle \\
 &= \left| r_p^{(t,r)} \right|^2 \left\{ \frac{A_1^2}{2} + \frac{A_2^2}{2} - A_1 A_2 \cos(2\theta_r') \cos(2k \sin \theta x - \delta_{1,2}) \right\} \exp\left( \frac{-2k\kappa_r z}{\cos \theta_r'} \right)
 \end{aligned} \tag{3.7}$$

It can be seen from Equation 3.7 that the intensity of the p polarized light is modulated by a factor of  $\cos \theta_r'$  as compared with s-polarized light, but the period  $\Lambda$  stays the same since the part  $\cos(2k \sin \theta x - \delta_{1,2})$  doesn't change.

### 3.1.2 Two asymmetrically incident beams

From the previous discussion, it can be seen that the period of the interference pattern is mainly controlled by the term  $\cos(2k \sin \theta x - \delta_{1,2})$  which represents the phase difference's influence in the intensity of the two incident beams along the x axis. Despite the phase shift of reflection and transmission, if simply dealing with the period on the photoresist's top surface, the problem then becomes a geometric light path way calculation. For different setups, which will be discussed in section 3.2, the relationship between the two beam's incident angles with the setup is slightly different. Following the same derivation, but relaxing the condition that the angles need to be identical, and that the amplitudes need to be identical one finds:

For s-polarized light:

$$E_s^{(1)} = \left| \tau_s^{(l,r)} \right| A_1 \cos \left( -k_r \sin \theta_1' x + k_r \cos \theta_1' z - \frac{2\pi}{T} t + \delta_1 + \chi_s \right) \exp \left( \frac{-k \kappa_r z}{\cos \theta_1'} \right) \mathbf{e}_y \quad (3.8)$$

$$E_s^{(2)} = - \left| \tau_s^{(l,r)} \right| A_2 \cos \left( k_r \sin \theta_2' x + k_r \cos \theta_2' z - \frac{2\pi}{T} t + \delta_2 + \chi_s \right) \exp \left( \frac{-k \kappa_r z}{\cos \theta_2'} \right) \mathbf{e}_y \quad (3.9)$$

The corresponding intensity is:

$$\begin{aligned} I &\propto \left\langle \left( E_s^{(1)} + E_s^{(2)} \right) \bullet \left( E_s^{(1)} + E_s^{(2)} \right)^* \right\rangle \\ &= \left| \tau_s^{(l,r)} \right|^2 \left\{ \frac{\hat{A}_1^2}{2} + \frac{\hat{A}_2^2}{2} - \hat{A}_1 \hat{A}_2 \cos \left[ (k \sin \theta_1 + k \sin \theta_2) x - (k \cos \theta_1 - k \cos \theta_2) z - \delta_{1,2} \right] \right\} \end{aligned} \quad (3.10)$$

where  $\hat{A}_{1,2} = A_{1,2} \exp \left( \frac{-k \kappa_r z}{\cos \theta_{1,2}'} \right)$  is the modified amplitude.

For p-polarized light:

$$\begin{aligned} E_p^{(1)} &= \left| \tau_p^{(l,r)} \right| A_1 \cos \left( -k_r \sin \theta_1' x + k_r \cos \theta_1' z - \frac{2\pi}{T} t + \delta_1 + \chi_p \right) \\ &\quad \exp \left( \frac{-k \kappa_r z}{\cos \theta_1'} \right) \left( -\cos \theta_1' \mathbf{e}_x + \sin \theta_1' \mathbf{e}_z \right) \end{aligned} \quad (3.11)$$

$$\begin{aligned} E_p^{(2)} &= \left| \tau_p^{(l,r)} \right| A_2 \cos \left( k_r \sin \theta_2' x + k_r \cos \theta_2' z - \frac{2\pi}{T} t + \delta_2 + \chi_p \right) \\ &\quad \exp \left( \frac{-k \kappa_r z}{\cos \theta_2'} \right) \left( -\cos \theta_2' \mathbf{e}_x - \sin \theta_2' \mathbf{e}_z \right) \end{aligned} \quad (3.12)$$

The corresponding intensity is:

$$I \propto \left\langle \left( E_p^{(1)} + E_p^{(2)} \right) \cdot \left( E_p^{(1)} + E_p^{(2)} \right)^* \right\rangle$$

$$= \left| \tau_p^{(i,r)} \right|^2 \left\{ \frac{\hat{A}_1^2}{2} + \frac{\hat{A}_2^2}{2} - \hat{A}_1 \hat{A}_2 \cos(\theta_1 + \theta_2) \cos \left[ (k \sin \theta_1 + k \sin \theta_2) x - (k \cos \theta_1 - k \cos \theta_2) z - \delta_{1,2} \right] \right\} \quad (3.13)$$

Where  $\hat{A}_{1,2} = A_{1,2} \exp \left( \frac{-k \kappa_r z}{\cos \theta_{1,2}} \right)$  is the modified amplitude as used in Equation 3.10.

Similarly, as with the case of two symmetrical incidences, the intensity is modulated by a factor of  $\cos(\theta_1 + \theta_2)$  for the p-polarized light, the period is still controlled by the same factor  $\cos(\theta_1 + \theta_2)$ , and therefore, the period along the x-axis is:

$$\Lambda = \frac{2\pi}{k(\sin \theta_1 + \sin \theta_2)} = \frac{\lambda}{\sin \theta_1 + \sin \theta_2} \quad (3.14)$$

The  $-(k \cos \theta_1 - k \cos \theta_2)z$  term in Equations 3.10 and 3.13 represents a vertical standing wave, which is caused by the difference in incident wave angle. For example, with the x value constant, by shifting the z position, the intensity becomes a sinusoidal periodic pattern. This is different from the well-known vertical standing wave, which is caused by the interference between incident light and reflected light which will be discussed in section 3.1.3 and in more detail in the anti-reflection coding section.

The period of the standing wave caused by these (two) asymmetrically incident beams therefore:

$$\Lambda_{vertical} = \frac{\lambda}{|\cos \theta_1 - \cos \theta_2|}, \theta_1 \neq \theta_2 \quad (3.15)$$

On the other hand, the  $-(k \cos \theta_1 - k \cos \theta_2)z$  term can also be treated as an extra phase difference  $\Delta \delta_{1,2}$  term caused by the different optical paths experienced by the two beams when travelling inside the film due to the difference in incident angles. In this way, the vertical position-dependent phase difference will cause a shift of the peak along the x-axis, which in turn results in a pattern shift.

It might seem useless to discuss this case in comparison with the symmetrical incident case, however in a real experiment, when one can change the desired horizontal standing wave period by tuning the angle of incident light, in order to obtain a large exposure area, the asymmetrical incident beams are more useful (see section 3.2). When minimizing the reflection of p polarized light by choosing angles near the Brewster angle, a vertical standing wave needs to be considered.

### 3.1.3 Vertical standing wave caused by reflection

Vertical standing wave occurs in the field of laser interference lithography [2-4] and also in other fields. For example interference pattern from soft x-rays standing waves are

useful in identifying and studying the chemical state and magnetic information at the buried interface between two materials [5, 6].

In the case of laser interference lithography, the vertical standing wave is unwelcome, which is known to cause problems such as low contrast ratio. One almost always wants to minimize the reflection in order to decrease this phenomenon. Therefore the formation of the vertical standing wave is important to understand. Figure 3.2 schematically shows the combination of horizontal and vertical standing waves [7].

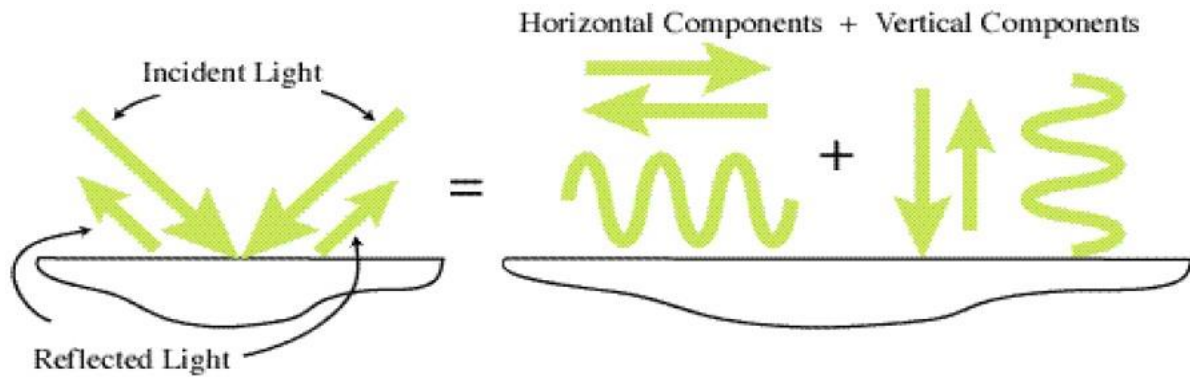


Figure 3.2 the horizontal and vertical components combine separately to create the desired horizontal standing wave and undesired vertical standing wave. [7]

The vertical standing wave is formed by the incident light and reflected light. The electric field inside the layer (e.g. photoresist) can be written as the following by using the same notation as before.

For s-polarized light:

$$E_s^{(1)} = |\tau_s| A_1 \cos \left( -k_r \sin \theta_1' x + k_r \cos \theta_1' z - \frac{2\pi}{T} t + \delta_1 + \chi_s \right) \exp \left( \frac{-k \kappa_r z}{\cos \theta_1'} \right) \mathbf{e}_y \quad (3.16)$$

$$E_s^{(2)} = -|r_s| |\tau_s| A_2 \cos \left( k_r \sin \theta_2' x - k_r \cos \theta_2' z - \frac{2\pi}{T} t + \delta_2 + \chi_s + \xi_s \right) \exp \left( \frac{-k \kappa_r z}{\cos \theta_2'} \right) \mathbf{e}_y \quad (3.17)$$

Where  $r_s$  is the reflection coefficient of the interface between two materials and  $\xi_s$  is the phase introduced by the reflection which is known as  $\pi$  phase-shift determined by the refractive index of the two material.

Then the intensity is therefore:

$$I \propto \left\langle \left( E_s^{(1)} + E_s^{(2)} \right) \bullet \left( E_s^{(1)} + E_s^{(2)} \right)^* \right\rangle \quad (3.18)$$

$$= \frac{\hat{A}_1^2}{2} + \frac{\hat{A}_2^2}{2} - \hat{A}_1 \hat{A}_2 \cos \left[ \left( k \sin \theta_1' + k \sin \theta_2' \right) x - \left( k \cos \theta_1' + k \cos \theta_2' \right) z - \delta_{1,2} + \xi_s \right]$$

where  $\hat{A}_1 = |\tau_s| A_1 \exp \left( \frac{-k \kappa_r z}{\cos \theta_1'} \right)$ ,  $\hat{A}_2 = |r_s| |\tau_s| A_2 \exp \left( \frac{-k \kappa_r z}{\cos \theta_2'} \right)$  are the new modified amplitudes here

which are different from those used in previous sections.

For p-polarized light:

$$E_p^{(1)} = |\tau_p^{(l,r)}| A_1 \cos \left( -k_r \sin \theta_1' x + k_r \cos \theta_1' z - \frac{2\pi}{T} t + \delta_1 + \chi_p \right) \exp \left( \frac{-k \kappa_r z}{\cos \theta_1'} \right) \left( -\cos \theta_1' \mathbf{e}_x + \sin \theta_1' \mathbf{e}_z \right) \quad (3.19)$$

$$E_p^{(2)} = |r_s| |\tau_p^{(l,r)}| A_2 \cos \left( k_r \sin \theta_2' x + k_r \cos \theta_2' z - \frac{2\pi}{T} t + \delta_2 + \chi_p + \xi_p \right) \exp \left( \frac{-k\kappa_r z}{\cos \theta_2'} \right) (-\cos \theta_2' \mathbf{e}_x - \sin \theta_2' \mathbf{e}_z) \quad (3.20)$$

Similar for the intensity:

$$I \propto \left\langle \left( E_p^{(1)} + E_p^{(2)} \right) \bullet \left( E_p^{(1)} + E_p^{(2)} \right)^* \right\rangle \quad (3.21)$$

$$= \frac{\hat{A}_1^2}{2} + \frac{\hat{A}_2^2}{2} - \hat{A}_1 \hat{A}_2 \cos(\theta_1 + \theta_2) \cos \left[ \left( k \sin \theta_1' + k \sin \theta_2' \right) x - \left( k \cos \theta_1' + k \cos \theta_2' \right) z - \delta_{1,2} + \xi_s \right]$$

where  $\hat{A}_1 = |\tau_p| A_1 \exp \left( \frac{-k\kappa_r z}{\cos \theta_1'} \right)$ ,  $\hat{A}_2 = |r_p| |\tau_p| A_2 \exp \left( \frac{-k\kappa_r z}{\cos \theta_2'} \right)$  are the modified amplitudes.

From Equations 3.18 and 3.21, it can be seen that the vertical standing wave comes from the term  $-(k \cos \theta_1' + k \cos \theta_2') z$ . Note that the two beams interfering here are the incident and the other reflected from the second interface, not the same as the two incident beams before in section 3.1.2.

Then, the period of the vertical standing wave can be calculated similar to previously:

$$\Lambda_{vertical} = \frac{\lambda}{\cos \theta_1' + \cos \theta_2'} \quad (3.22)$$

When  $\theta_1 = \theta_2$ , Equation 1.22 becomes  $\Lambda_{vertical} = \frac{\lambda}{2 \cos \theta_1'}$  which concords the widely used equation in reports[5-7].

### 3.2 Lloyd's Mirror Interferometer

There are two setups for two laser interference lithography: Lloyd's mirror interferometer and dual beam interferometer. The main difference between these two methods is the need of a beam splitter. By using beam splitters, one can split as many beams as needed. The problem with beam splitters is that it requires a much more complicated configuration for keeping the phase difference among those beams constant and they are more fragile to environment, e.g., vibration. Recent works mainly focus on the use of four-beam laser interference lithography with different angles, intensities, and polarizations [8-13] for being able to generate complicated periodic patterns using one simple dose.

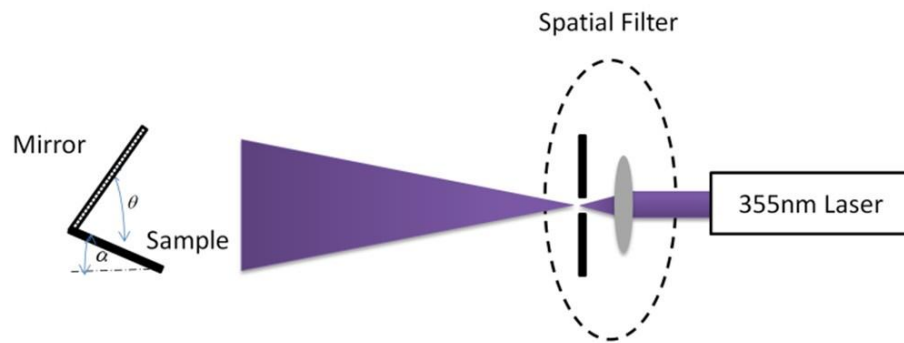


Figure 3.3 Lloyd's mirror interferometer setup

Figure 3.3 shows the typical setup of a Lloyd's mirror interferometer. The setup consists of a long coherent length laser, a spatial filter (made by a pinhole placed at the focus point of an objective lens), a mirror and a sample holder. The mirror is used to reflect the laser beam onto the sample so that two beams can incident at the surface simultaneously.

There are two angles noticeable as  $\theta$  and  $\alpha$  in the setup, note that they are not directly the two incident angles ( $\theta_1$  and  $\theta_2$ ) discussed before but can be transformed easily. By assuming the incident light to be a horizontal plane wave and neglecting the Gaussian beam nature, a simple geometric relationship between  $(\theta, \alpha)$  and  $(\theta_1, \theta_2)$  can be derived as following:

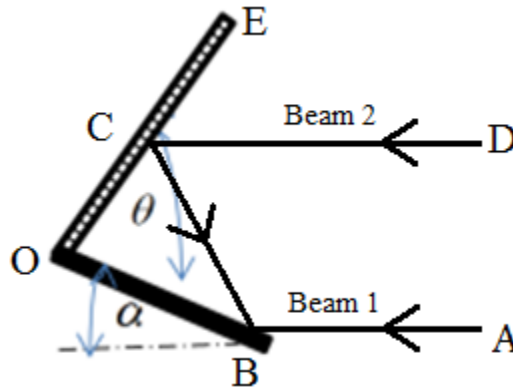


Figure 3.4 Geometric relationship between angles

As illustrated in Figure 3.4, two light beams 1 and 2 travel along direction the AB and DCB, and interfere at point B. We know  $\angle BCO = \angle ECD = \theta - \alpha$  due to the law of reflection. Knowing that  $\angle CBO = \pi - \theta - \angle BCO = \pi + \alpha - 2\theta$ , then the two incident angles are:

$$\theta_1 = \frac{\pi}{2} - \alpha \quad (3.23)$$

$$\theta_2 = \frac{\pi}{2} - \angle CBO = 2\theta - \alpha - \frac{\pi}{2} \quad (3.24)$$

A negative value of  $\theta_2$  means  $\angle CBO > 90^\circ$  which results in the two beams incident onto the surface from same side. Thus the dependence of the period  $\Lambda$  on the two angles  $\theta$  and  $\alpha$  is:

$$\Lambda = \frac{\lambda}{\sin\theta_1 + \sin\theta_2} = \frac{\lambda}{2\sin(\theta)\sin(\theta - \alpha)} \quad (3.25)$$

From Equation 3.23 and 3.24, we can see that when  $\theta = \frac{\pi}{2}$ ,  $\theta_1 = \theta_2$  which is the reason why Lloyd's mirror setup has the angle between sample and mirror fixed to be  $\frac{\pi}{2}$  [5-7].

### 3.3 Reflection Calculation and Anti-reflection Coating

#### 3.3.1 The Importance of Reflection

Reflection calculations are of great interest for every optics related project, sometimes aimed for maximizing and sometimes for minimizing. In the case of laser interference lithography, as discussed before, reflection is the main reason for the formation of vertical standing waves, which results in a bad aspect ratio of the lithography results and leads to low quality structures. Thus, a way to calculate reflection is of importance here. In this chapter, two methods of reflection coefficient calculation will be discussed first for the case of reflection happening on a single interface. These two methods are based on material [14] and the python code is attached in appendix A for reference. Then, a method for reflection coefficient calculation for an assembly of thin films will be discussed based on material [15].

A matlab code is used for the calculation [16]. Then the mechanism and design concept of anti-reflection coatings will be discussed based on the calculation of reflections.

### **3.3.2 Effective Index Methods for Reflection Coefficient Calculation**

In order to save time and space, the following discussion will start from the Fresnel equation directly since everyone knows that all optical equations can be derived from Maxwell's equation. As shown in Figure 3.5, light incident from medium 0 with refractive index  $n_0$  and incident angle  $\theta_0$ , refracts into medium 1 with refractive index  $n_1$  and transmission angle  $\theta_1$ .

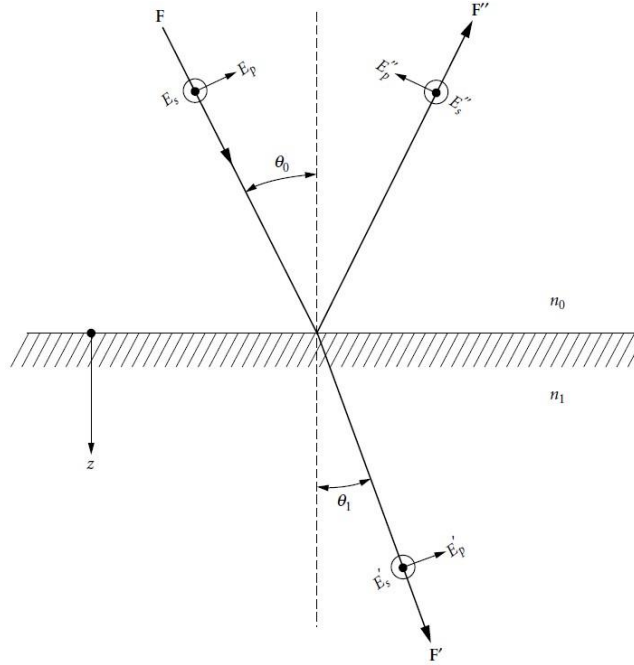


Figure 3.5 coordinate system for measuring the E vectors of a plane wave reflected and refracted at a boundary [14]

For non-absorbing material, Fresnel equations give out the reflection coefficients of both s and p polarizations, and the same with transmission coefficients.

$$\frac{E''_s}{E_s} = r_s = \frac{n_0 \cos \theta_0 - n_1 \cos \theta_1}{n_0 \cos \theta_0 + n_1 \cos \theta_1} \quad (3.26)$$

$$\frac{E''_p}{E_p} = r_p = \frac{n_1 \cos \theta_0 - n_0 \cos \theta_1}{n_1 \cos \theta_0 + n_0 \cos \theta_1} \quad (3.27)$$

$$\frac{E'_s}{E_s} = t_s = \frac{2n_0 \cos \theta_0}{n_0 \cos \theta_0 + n_1 \cos \theta_1} \quad (3.28)$$

$$\frac{E_p'}{E_p} = t_p = \frac{2n_0 \cos \theta_0}{n_1 \cos \theta_0 + n_0 \cos \theta_1} \quad (3.29)$$

For an absorbing material, the refractive index is modified from a real value to complex and the absorbing is counted in the imaginary part. There are several different conventions in optics where the complex refractive index is defined differently which usually differs at the sign of the imaginary part which corresponds to the convention of wave vector used. Here, the complex refractive index is defined as

$$\tilde{n}' = n - ik \quad (3.30)$$

which corresponds to the wave vector  $E = E_0 \exp \left[ i\omega \left( t - \frac{\tilde{n}' z}{c} \right) \right]$ . Methods of effective indexes can be used for calculations with absorbing material and have two different approaches: the Bernings method and the Abeles' method.

#### i. Bernings method

The effective indexes  $\eta_{0s}$  and  $\eta_{0p}$  for the s and p components of non-absorbing medium of incidence are:

$$\eta_{0s} = n_0 \cos \theta_0 \quad (3.31)$$

$$\eta_{0p} = \frac{n_0}{\cos \theta_0} \quad (3.32)$$

where  $n_0$  generally equals 1 for air. The complex effective indexes of the absorbing material are:

$$\tilde{\eta}_{1s} = \tilde{n}_1 \cos \theta_1 \quad (3.33)$$

$$\tilde{\eta}_{1p} = \frac{\tilde{n}_1}{\cos \theta_1} \quad (3.34)$$

Where  $\tilde{n}_1 = n_1 - ik_1$  is the complex refractive index of the material, and

$$\cos \theta_1 = \left[ \frac{(\alpha_1^2 + \beta_1^2)^{1/2} + \alpha_1}{2} \right]^{1/2} - i \left[ \frac{(\alpha_1^2 + \beta_1^2)^{1/2} - \alpha_1}{2} \right]^{1/2} \quad (3.35)$$

$$\alpha_1 = 1 + \left( \frac{n_0 \sin \theta_0}{n_1^2 + k_1^2} \right)^2 (k_1^2 - n_1^2) \quad (3.36)$$

$$\beta_1 = -2n_1 k_1 \left( \frac{n_0 \sin \theta_0}{n_1^2 + k_1^2} \right)^2 \quad (3.37)$$

## ii. Abeles' method

The effective indexes are calculated differently:

$$\tilde{\eta}_{1s} = a - ib \quad (3.38)$$

$$\tilde{\eta}_{1p} = c - id \quad (3.39)$$

Where

$$a^2 - b^2 = n_1^2 - k_1^2 - n_0^2 \sin^2 \theta_0 \quad (3.40)$$

$$ab = n_1 k_1 \quad (3.41)$$

$$c = a \left( 1 + \frac{n_0^2 \sin^2 \theta_0}{a^2 + b^2} \right) \quad (3.42)$$

$$d = b \left( 1 - \frac{n_0^2 \sin^2 \theta_0}{a^2 + b^2} \right) \quad (3.43)$$

After getting the effective refractive index  $\eta$ , the reflection coefficients can be calculated for both methods:

$$r_s = \frac{\eta_{0s} - \eta_{1s}}{\eta_{0s} + \eta_{1s}} \quad (3.44)$$

$$r_p = \frac{\eta_{1p} - \eta_{0p}}{\eta_{1p} + \eta_{0p}} \quad (3.45)$$

All refractive indexes at 355nm wavelength used for calculation are contained in Table 3.1. The extinction coefficient  $k$  is related to the absorption coefficient  $\alpha$  by

$$\alpha = \frac{4\pi k}{\lambda} \quad (3.46)$$

Table 3.1 Refractive Index list for Materials at 355nm wavelength

Material	n	k
Zinc Oxide [17]	2.47464	0.4308
Amorphous Silicon [18]	4.64682	
Single Crystalline Silicon [19]	5.610	3.014
High Temperature Glass [18]	1.5646	
Photoresist (AZ5214E) [20]	1.6990	0.0175
Anti-Reflection Coating (WIDE 15B) [21]	1.72	0.33
Gold [22]	1.73817	1.8491

By knowing the refractive indexes of the materials of interest, the reflection coefficient of certain incident angles can be calculated. Here, we use 355nm which is the wavelength of the UV laser we use for fabrication. The reflection coefficients for gold, glass and silicon were calculated and are shown in Figure 3.6.

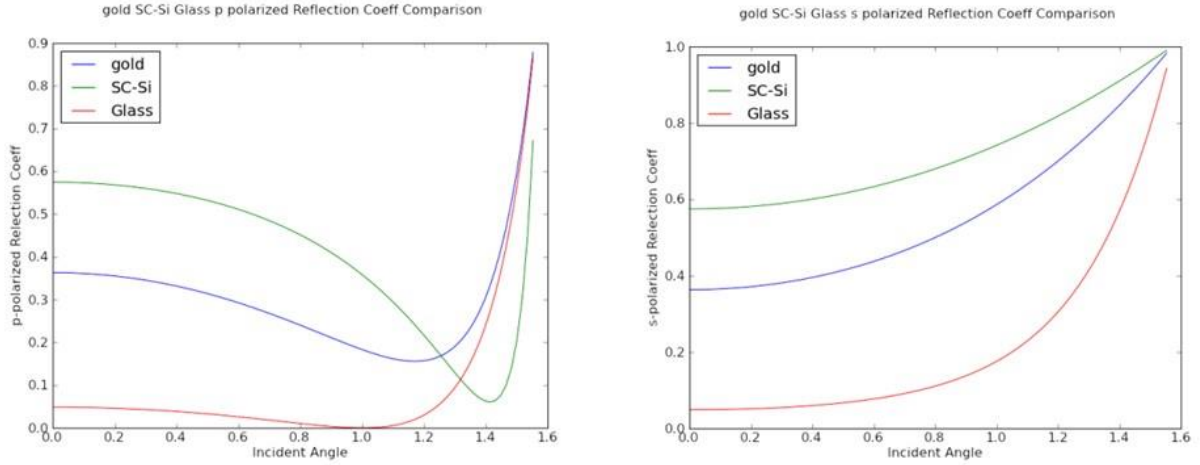


Figure 3.6 Angle dependence of reflection coefficient of light with 355nm wavelength upon different materials: gold, silicon and glass, a) p-polarized incident light, b) s-polarized incident light

One may quickly notice that there is a drop in reflection coefficient in the p-polarization with angles from 0 approaching 90 and after which the reflection coefficient goes from a minimum value straight up to a maximum. This phenomenon is known as the Brewster angle, by which reflection of p-polarized light is terminated. As our interest of reflection study is to minimize the reflected power, in other words, to obtain the minimum value in reflection coefficients, p-polarized light offered a unique opportunity for fabrication under certain incident angles for a given choice of materials.

### 3.3.3 Reflection Calculation of an Assembly of Thin Films

To calculate the reflection coefficient of an assembly of thin films, first, using results before, we separate the phase factors of the fields:

$$\text{Incident} \quad \exp\left\{i\left[\omega t - (2\pi n_0 / \lambda)(x \sin \theta_0 + z \cos \theta_0)\right]\right\} \quad (3.47)$$

$$\text{Reflected} \quad \exp\left\{i\left[\omega t - (2\pi n_0 / \lambda)(x \sin \theta_0 - z \cos \theta_0)\right]\right\} \quad (3.48)$$

$$\text{Transmitted} \quad \exp\left\{i\left[\omega t - (2\pi (n_1 - ik_1) / \lambda)(x \sin \theta_1 + z \cos \theta_1)\right]\right\} \quad (3.49)$$

Where  $(n_1 - ik_1) \sin \theta_1 = n_0 \sin \theta_0$ , according to Snell's law but the value of  $\theta_1$  can be complex.

For the following calculations, letters for boundaries and numbers for layers will be used, as shown in Figure 3.7.

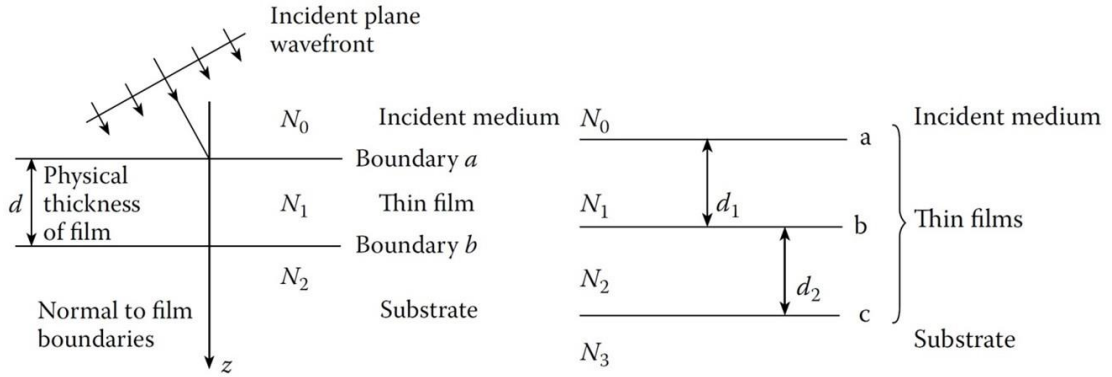


Figure 3.7 Schematic of plane wave incident on an assembly of thin films [15]

Then the tangential of the field components which are parallel to the boundary by neglecting the common phase factors can be written as:

$$E_b = E_{1b}^+ + E_{1b}^- \quad (3.50)$$

$$H_b = \eta_1 E_{1b}^+ - \eta_1 E_{1b}^- \quad (3.51)$$

The fields at interface a can be derived by adding a phase shift term

$$\delta = 2\pi N_1 d_1 \cos \theta_1 / \lambda \quad (3.52)$$

And the relationship between each component in the two films can be denoted by the matrix below:

$$\begin{bmatrix} E_a \\ H_a \end{bmatrix} = \begin{bmatrix} \cos \delta & (i \sin \delta) / \eta_1 \\ i \eta_1 \sin \delta & \cos \delta \end{bmatrix} \begin{bmatrix} E_b \\ H_b \end{bmatrix} \quad (3.53)$$

Where  $\eta$  is the tilted optical admittance, which connects components of electric field and magnetic field parallel to the boundary as:

$$\eta = \frac{H}{E} \quad (3.54)$$

And is defined as

$$\eta_p = \frac{y}{\cos \theta} = \frac{n \sqrt{\epsilon_0 / \mu_0}}{\cos \theta} \quad (3.55)$$

$$\eta_s = y \cos \theta = n \sqrt{\epsilon_0 / \mu_0} \cos \theta \quad (3.56)$$

where  $y$  is the optical admittance.

Equation 1.52 deals with a single film, but can be applied to an assembly of films by multiply a series of matrixes:

$$\begin{bmatrix} E_{out} \\ H_{out} \end{bmatrix} = \prod_j \begin{bmatrix} \cos \delta & (i \sin \delta) / \eta_j \\ i \eta_j \sin \delta & \cos \delta \end{bmatrix} \begin{bmatrix} E_{initial} \\ H_{initial} \end{bmatrix} \quad (3.57)$$

S polarized light is popularly used for laser interference lithography for the high contrast ratio that has been discussed in previous sections. Based on the calculation, it is found that using p-polarized light has less reflection, which benefits in having less vertical standing waves.

### A. Anti-reflection Coating on Substrates

Reflection coefficients depend on the refractive index, thickness and substrate of the film. Anti-reflection coatings are widely used for the reduction of undesired vertical standing wave formation. Such thin-film anti-reflection coating layers normally act by cancelling two reflected beams, e.g. one reflected when boundary b meets another beam reflected from boundary c and refracted to medium 1 at boundary b at the same point. When the phase difference between those two beams is a half-wavelength (180 degree phase) that resulting Poynting vector (intensity) is reduced.

Another approach is to make the antireflection layer very absorbing. Since the antireflection coating material has a large extinction value, a thick layer can absorb most of the light regardless of phase factor, preventing reflection from the substrate. If the interfere at the photoresist / reflection layer is index matched, the reflection from the front surface of the antireflection layer is reduced.

Assuming the light is incident from air, once the substrates and materials are chosen, there are two unknown variables: the incident angle and thickness of the ARC. For a specific

incident angle, the thickness of the anti-reflection coating needs optimization in order to obtain minimum reflection. For an incident angle of  $45^\circ$  onto an ARC layer on top of a silicon substrate, the resulting reflection coefficient of each polarization is shown in Figure 3.8 as a function of ARC thickness based on which thickness minimizes reflection. For p-polarized light, the thickness of 65.6nm gives the lowest reflection coefficient of 0.009. For s-polarized light, the thickness of 57.3nm gives the lowest reflection coefficient of 0.008.

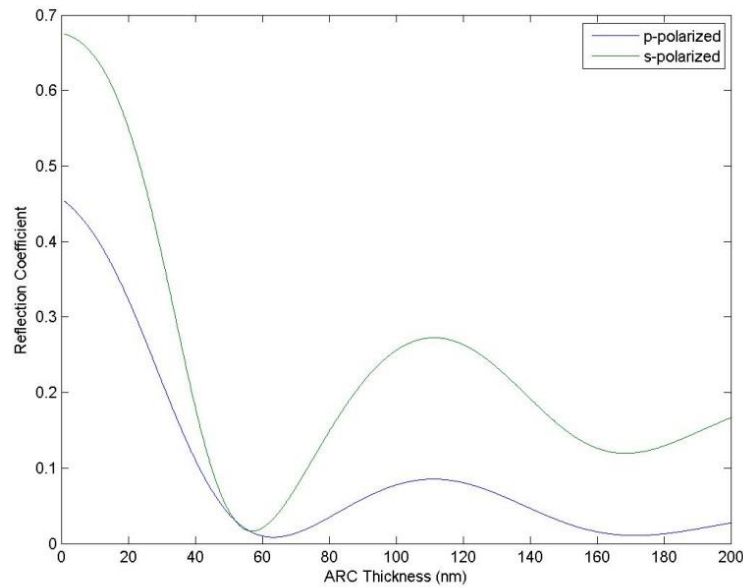


Figure 3.8 Reflection dependence of s and p polarized light on ARC thickness on silicon substrate. The incident angle is 45 degrees

Silicon has a high index of refraction (5.610) and produces a strong reflection compared to glass (index of 1.565). Figure 3.9 shows the reflection calculation of  $45^\circ$

incident light onto a glass substrate coated with an ARC layer. The calculation used the refractive index of high temperature glass, which better suits the metal oxide deposition procedure, e.g. ZnO deposited by PLD[17]. Reflection of p polarized light is much lower than s polarized light with all thicknesses of ARC layers up to 200nm. This agrees well with the reflection calculation of pure glass substrates shown in Figure 3.6. The reflection of p polarized light in this case is well below 0.1 and s polarized light has minimum reflection with 0 ARC thickness, both indicating the unnecessary use of ARC.

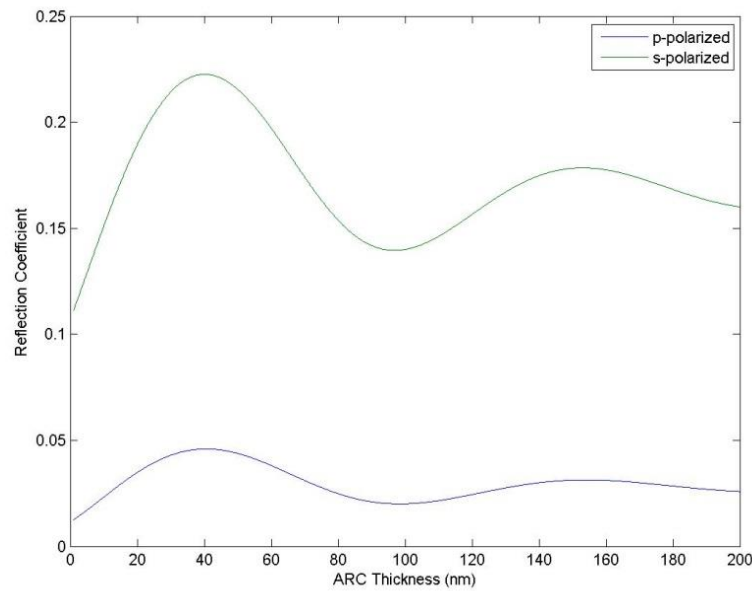


Figure 3.9 Reflection dependence of s and p polarized light on ARC thickness on glass. The incident angle is 45 degrees

The reflection coefficient varies with different conditions and can change significantly as seen in Figure 3.8 and Figure 3.9. A two dimensional image showing reflection coefficient values as a function of ARC layer thickness (x axis) and incident angle (y axis) is thus useful. Figure 3.10 shows the reflection calculation of both polarizations. The behavior differs with different polarizations as the incident angle increases from zero to ninety. This is similar to the Brewster angle in reflection where the reflection of p polarized light drops to zero when light is incident onto a certain substrate by its Brewster's angle as seen in Figure 3.6a.

To understand the variation of the reflection as a function of ARC coating thickness and incident angle one can produce surface plots as shown in Figure 3.10 and 3.11 where lighter colors represent higher intensities.

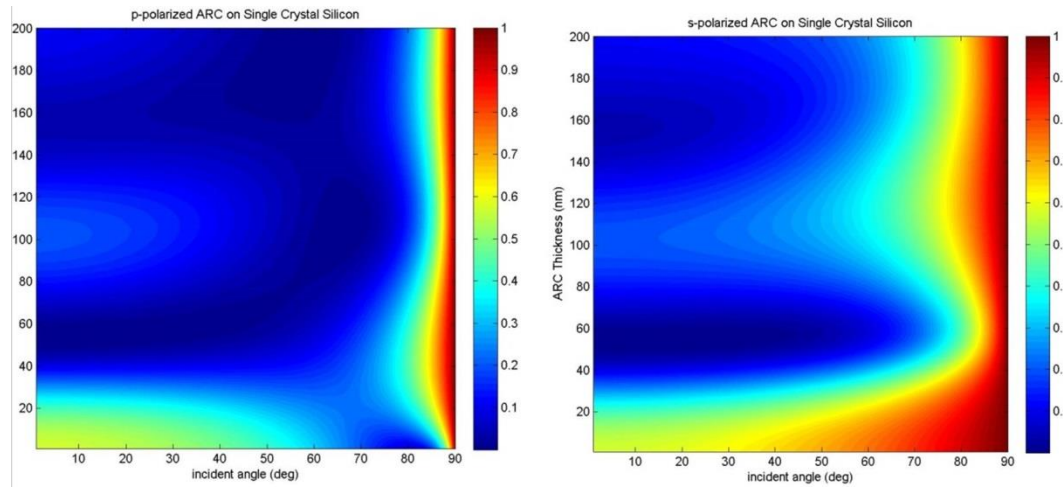


Figure 3.10 Reflection calculation of different ARC thickness on silicon substrate with different incident angle

Generally, p-polarized light has lower reflection with thin ARC thicknesses than s-polarized light. Both polarizations have a peak near 100nm thick ARC coating which corresponds to the standing wave condition  $2nt = m\lambda$ , where m is an integer. The drop of reflection with increased incident angle of p-polarized light makes it still useful for a 100nm ARC at angle of 60 to 70 degrees. However, since s-polarized light has an increasing reflection with the angle regardless of ARC thicknesses, one finds that the stronger reflection would make the same 100nm ARC not as useful. One finds that the reflection of s-polarized light for certain incident angles does decrease with increased ARC thickness, but forms little local peaks which indicates that the absorption of the thin film ARC is not enough to overcome the interference effect and thus the ARC coating behaves like an interference anti-reflection type, where the reflection at the top cancels out with the light reflected at the bottom of the ARC thin film.

Reflection calculations of ARC on glass of both polarizations are shown in Figure 3.11. The results are similar to Figure 3.6 with a little fluctuation with increased ARC thickness. The need to reduce reflection on glass mainly lies in the region of high incident angles, namely 70° to 90°. Unfortunately, the ARC doesn't make as large of a difference as expected and can be considered unnecessary for glass substrates.

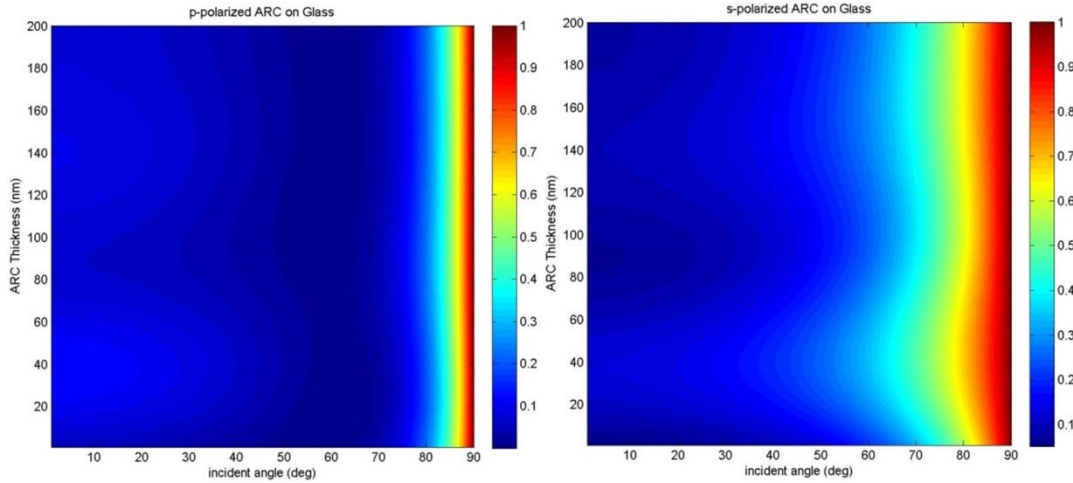


Figure 3.11 Reflection calculation of different ARC thickness on glass substrate with different incident angle

Comparing Figure 3.10 and Figure 3.11 one sees the significance of the higher index of silicon compared to glass in reflection.

### B. ZnO Thin Film on Substrates

ZnO thin films have many favorable optical and gas sensing properties as discussed in Chapter 2. It can be used as a thin film interference type anti-reflection coating in the gas sensor process. A laser interference lithography patterned photo-resist can be used on top of the ZnO thin film deposited on top of certain substrates. Since ZnO has strong absorption at 355nm [17], it is a good replacement for ARC, which makes the process ARC free and much easier. A patterned ZnO thin film by itself is used as a UV anti-reflection coating, which could be made by laser interference lithography technique too [23].

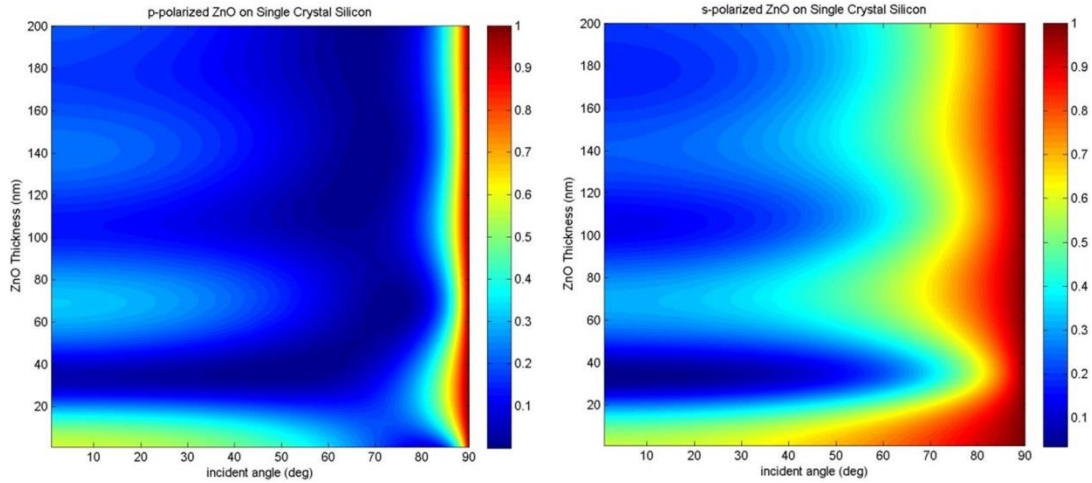


Figure 3.12 Reflection calculation of different ZnO thickness on silicon substrate with different incident angle

The vertical period of the reflection seen in Figure 3.12 corresponds to the standing wave condition as the thickness of ZnO increases. The results confirm the possible use of thin film ZnO as an interference type anti-reflection coating, which reduces the complexity of process. P polarized light shows more advantages than s polarized light at larger incident angles due to its unique Brewster angle condition. At thicknesses of 35nm and 108nm, both polarizations show minimum reflection. At thicknesses of 71nm and 143nm, p-polarized light shows minimum reflection at high incident angles near 80°.

Reflection calculations of ARC on glass of both polarizations are shown in Figure 3.11. The results are similar to ZnO on a silicon substrate, which indicates the same role of ZnO thin films as an interference anti-reflection coating in these two structures. The period of reflection with increasing ZnO thickness differs with half period drift of the two substrates which is caused by the difference of the refractive index of glass and silicon, one smaller

than that of ZnO while the other bigger, which results in a difference of a half-wave loss in the reflection known as  $\pi$  phase change.

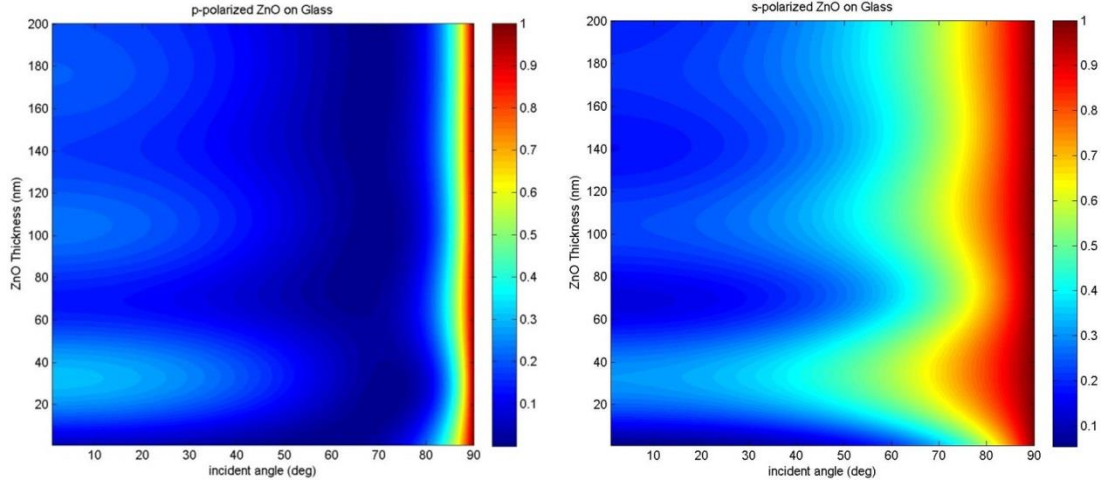


Figure 3.13 Reflection calculation of different ZnO thickness on glass substrate with different incident angle

Our results are based on the model in section 3.3.3. An alternative way to view these results is to interpret the periodicity of returns. Variation with ZnO thickness as weekly coupling of the incident beam with the intrinsic modes of the structure [24]. By using coupled mode theory, one would expect similar results. The model is also similar to MIE theory, which is set up in cylindrical coordinates rather than the Cartesian system used here. Both models assume a propagating wave in the last layer (substrate layer here and core layer in Mie theory) rather than an evanescent wave.

These types of calculations mainly depend on the thickness and refractive index of each layer, thus, an accurate measurement is essential towards achieving the right design. For example, silicon has a wide variety of forms which results in a large range of refractive indexes. Reflection calculations of ARC and ZnO on amorphous silicon are carried out and shown in Figure 3.14.

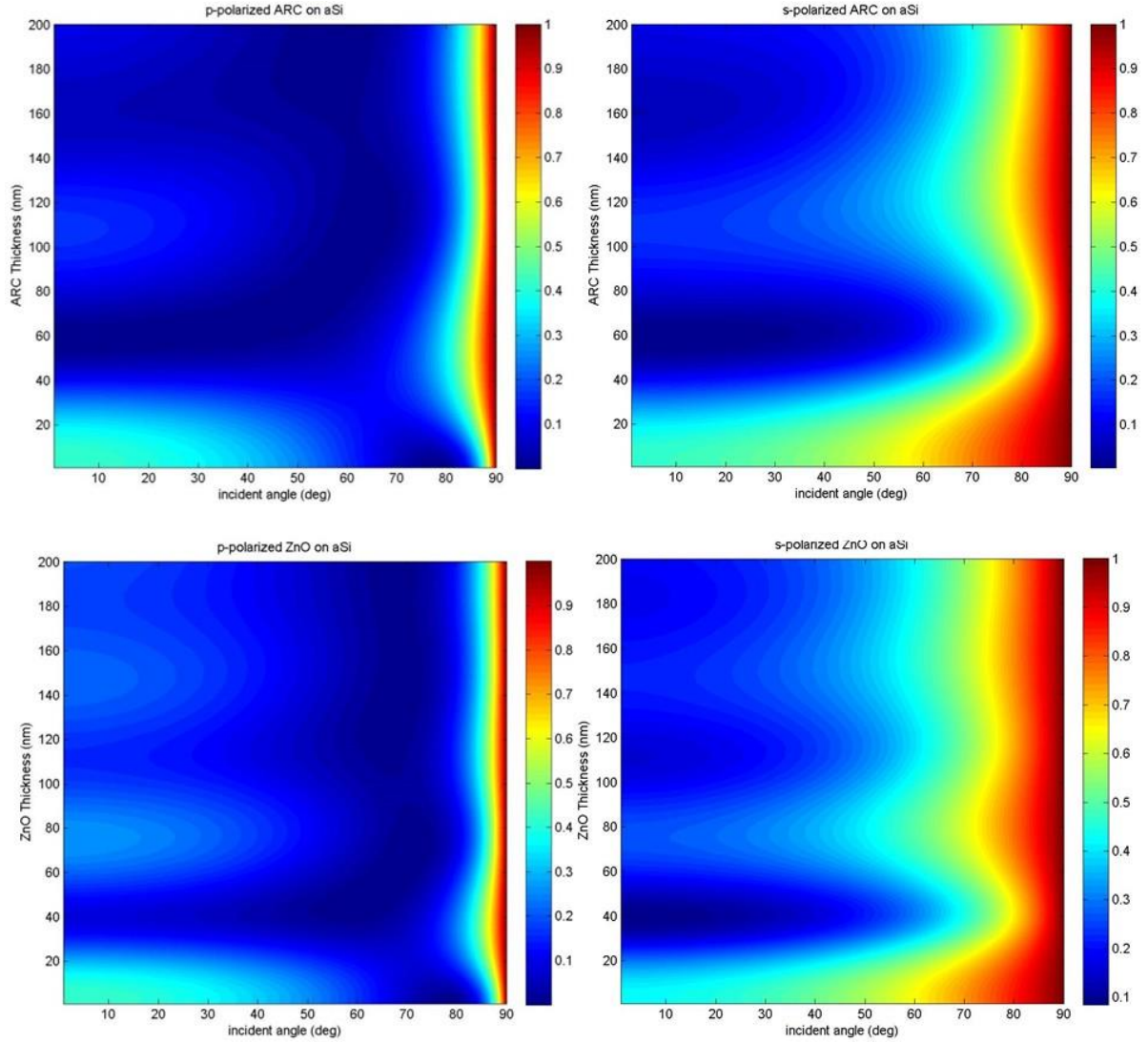


Figure 3.14 Reflection calculation of different ARC/ZnO thickness on amorphous silicon substrate with different incident angle

The drop in refractive index from  $5.610 - 3.014i$  of silicon to  $4.6468$  of amorphous silicon makes it match the  $2.4746 - 0.4708i$  refractive index of ZnO better.

### 3.4 Field Distribution

The theoretical direction of laser interference lithography has long relied on the calculation of aspect ratio( $V$ ), which simply considers the relative intensity and incident angles of the two beams [7].

$$V = \frac{I_{\max} - I_{\min}}{I_{\max} + I_{\min}} = \left( \frac{2\sqrt{I_1 I_2}}{I_1 + I_2} \right) |g_{12}| \quad (3.58)$$

Where  $I_1$  and  $I_2$  are the intensity of the two beams and  $g_{12}$  represents the relative phase difference between the two beams. The phase difference is generated by the difference in optical path of the two beams when arriving at the sample surface, which has been discussed in sections 3.1 and 3.2. This term is mainly determined by the geometry of the setup and the angles between each plane, shown in Figure 3.3 and Fig 3.4.

A more direct and vivid way is to calculate the field distribution inside the structure, especially the photo-resist layer which is of the most interest. Since the photoresist reacts with the UV light, the shape of the final product is thus determined by the field distribution. Traditionally, the field distribution is calculated by FDTD calculations, which is a finite difference calculation method. Here, an alternative calculation method is proposed for the first time based on the model in section 3.3.3 and compared with FDTD results.

### 3.4.1 FDTD Calculation Method

There are several FDTD calculation softwares: Meep, OptiFDTD, WOLFSIM, and FDTD solutions. The calculations in this section are done using FDTD Solutions [25] which unlike the other free software, is a commercial one. The software is chosen because of the familiarity, ease of use and good customer support since the author has previously used it for plasmonic calculations. [26, 27]

The Maxwell equations can be re-written into two curl equations:

$$\nabla \times E = -\mu \frac{\partial H}{\partial t} - \sigma_m H \quad (3.59)$$

$$\nabla \times H = \varepsilon \frac{\partial E}{\partial t} + \sigma_\varepsilon E \quad (3.60)$$

where  $E$  is the electric field component,  $H$  is the magnetic field component,  $\mu$  is the permeability,  $\varepsilon$  is the permittivity,  $\sigma_m$  is the effective permeability and  $\sigma_\varepsilon$  is the electric conductivity. FDTD is usually used for the study of non-magnetic materials where  $\mu = \mu_0$  and  $\sigma_m = 0$ . Thus the material's electromagnetic properties are determined by its permeability  $\mu$  and electric conductivity  $\sigma_\varepsilon$ . The continuous space is divided into small units known as the Yee unit in the FDTD numeric calculations. The electric and magnetic components are calculated stepwise in the Yee unit shown in Figure 3.15.

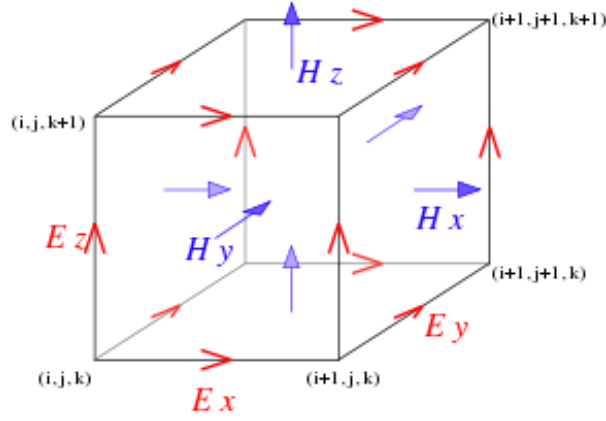


Figure 3.15 Yee unit cell [26]

The recurrence relation of the Maxwell equations can be written as:

$$H_z^{n+\frac{1}{2}}(i+\frac{1}{2}, j+\frac{1}{2}) = H_z^{n-\frac{1}{2}}(i+\frac{1}{2}, j+\frac{1}{2}) + CD \left[ E_x^n(i+\frac{1}{2}, j+1) - E_x^n(i+\frac{1}{2}, j) + E_y^n(i, j+\frac{1}{2}) - E_y^n(i+1, j+\frac{1}{2}) \right] \quad (3.61)$$

$$E_x^{n+1}(i+\frac{1}{2}, j) = CA(i+\frac{1}{2}, j)E_x^n(i+\frac{1}{2}, j) + CD \times CB(i+\frac{1}{2}, j) \left[ H_z^{n+\frac{1}{2}}(i+\frac{1}{2}, j+\frac{1}{2}) - H_z^{n+\frac{1}{2}}(i+\frac{1}{2}, j-\frac{1}{2}) \right] \quad (3.62)$$

$$E_y^{n+1}(i, j+\frac{1}{2}) = CA(i, j+\frac{1}{2})E_y^n(i, j+\frac{1}{2}) + CD \times CB(i, j+\frac{1}{2}) \left[ H_z^{n+\frac{1}{2}}(i-\frac{1}{2}, j+\frac{1}{2}) - H_z^{n+\frac{1}{2}}(i+\frac{1}{2}, j+\frac{1}{2}) \right] \quad (3.63)$$

Where CA, CB, CD are defined as:

$$CA(i, j, k) = \frac{1 - \frac{\sigma(i, j, k)\Delta t}{2\varepsilon(i, j, k)}}{1 + \frac{\sigma(i, j, k)\Delta t}{2\varepsilon(i, j, k)}} \quad (3.64)$$

$$CD = \frac{\Delta t}{\Delta s} \frac{1}{\sqrt{\epsilon_0 \mu_0}} \quad (3.65)$$

$$CB(i, j, k) = \frac{\epsilon_0}{\epsilon(i, j, k) + \frac{\sigma \Delta t}{2}} \quad (3.66)$$

Where  $i, j$  and  $k$  are integers used as notations for the Yee unit. From equations 3.61 to 3.66, the FDTD calculation only takes information of the distribution of permeability and electric conductivity in the structure and applies stepwise Maxwell equations to solve for the electromagnetic field of interest. Since it's a finite difference calculation method, the finer the Yee unit will result in a better accuracy, but requires more memory of the computer.

The FDTD solutions are calculated by using software FDTD solutions on a Dell XPS 8300 desktop with Intel i7-2600 cpu and 20 GB memory. Figure 3.16 shows the 2D simulation setup in the software. A structure of 300nm photo-resist (AZ5214E) and 35nm ZnO in sequence on top of a 5 $\mu$ m Si substrate is set for simulation. A plane wave with only 355nm wavelength p-polarized incident light is put 400nm above the top face of photo-resist with an incident angle of 45°. All layers are set as 5 $\mu$ m wide along the Z direction, which is infinite in calculation of the 2D simulation but is needed for a correct index distribution. The FDTD simulation area is set 300nm above the light source and 465nm below the ZnO-Si interface. The boundary condition of y direction is set as a perfect matched layer (PML) which absorbs electromagnetic energy incident upon it. The boundary condition of the x direction is set as Bloch, which adds a phase shift between each period when the structures and EM fields are periodic. The mesh type is set as 'auto non-uniform' for the reflection

calculation with an accuracy level of 8 (highest) to save calculation time, and ‘uniform’ with 1nm maximum mesh step settings in both x and y directions to compare with theoretical calculation results for field distribution inside the structure. A three frequency domain power monitor is set to monitor the reflection of the structure together with the field distribution inside the structure. A time monitor is set 100nm up from the lower boundary of FDTD simulation area to make sure that the light pulse has passed through the entire simulation area. An index monitor is set covering the entire simulation area to make sure the refractive index is set correctly. The angle and polarization direction are changed to perform simulations accordingly.

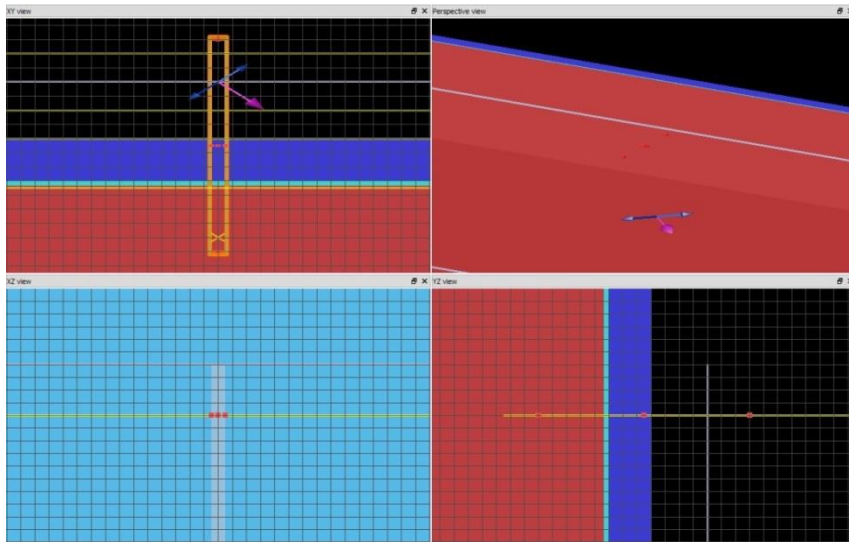


Figure 3.16 FDTD simulation setup

Since the FDTD calculation largely relies on the accuracy of index of refraction structure setup, it is important to check the index distribution in the simulation to see if it is the same as designed. FDTD solutions use a light pulse in simulation so that a time monitor is necessary to make sure the light pulse has passed the entire structure in the simulated time period. The results from index and time monitors are shown in 3.17. The simulation runs 150fs before auto-shutdown. The light pulse passed the time monitor at 40fs and was adsorbed by the PML layer with no fluctuation afterwards. The index also matches the setup well.

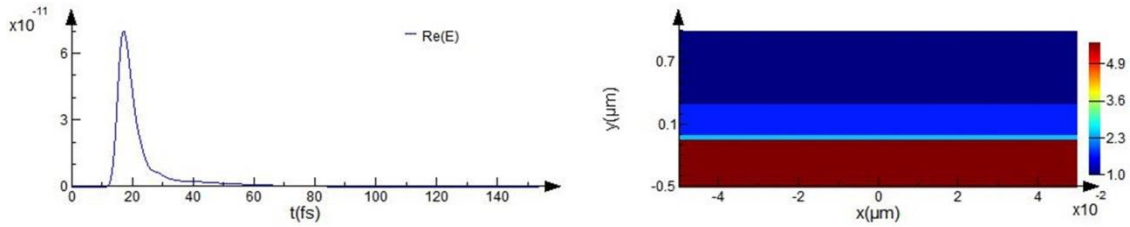


Figure 3.17 FDTD simulation time monitor (left) and index monitor (right) results

The simulated reflection is calculated by two methods using monitors placed behind and in front of the light source. By subtracting the ratio of transmission from 1 using data from the monitor between the light source and the structure, R1 is calculated. R2 is calculated straight from the power ratio at a monitor placed behind the light source. The FDTD results are put together with theoretical calculation results in Figure 3.18 with the same structure described in the FDTD simulation setup.

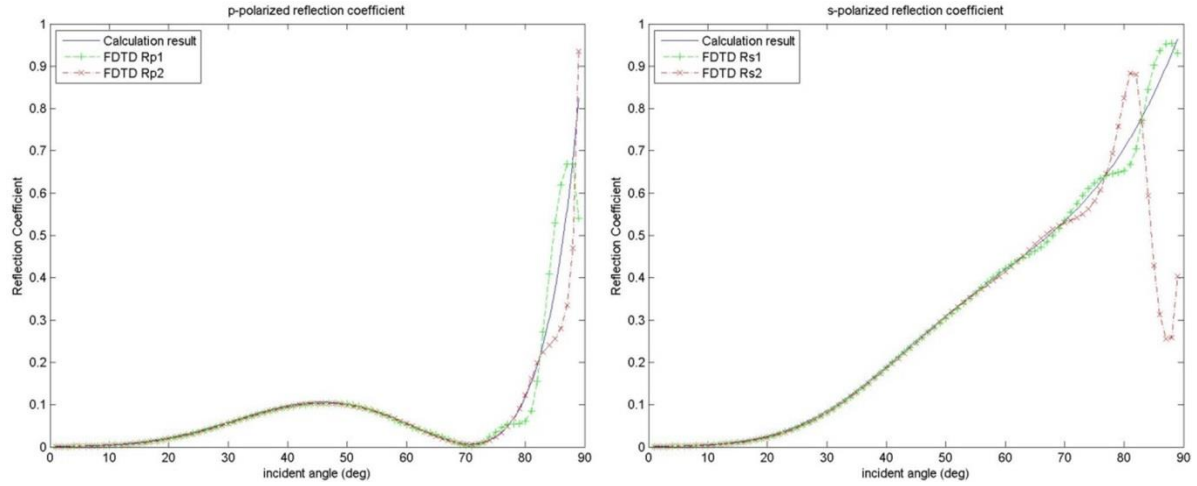


Figure 3.18 Reflection Coefficient of theoretical and FDTD calculation

The result of theoretical calculation agrees very well with FDTD calculation at incident angles smaller than  $70^\circ$ . At higher angles, the two methods of reflection calculation don't agree with each other, which are results of a weakness in the simulation that at non-normal incidence the Bloch boundary condition together with the light source hardly fits the plane wave and periodic condition, which is usually a problem in FDTD methods.

The field distribution is monitored in the FDTD simulation by a power monitor that captures the three components of the electric field:  $E_x$ ,  $E_y$  and  $E_z$ . Each component is kept in a matrix with complex values so that the phase term is kept together. Two simulations were run separately to capture the field distribution of the two incident lights to keep the periodic boundary condition, which adds a constant phase according to the incident angle, between each period of the simulation region. The components of the electric field were added accordingly afterwards in the case of fully coherent which is the basis of interference.

### **3.4.2 Theoretical Field Distribution Calculation Method**

The model used in reflection coefficient calculation of an assembly of films in section 3.3.3 also gives the electromagnetic field components at the interface between each film by ignoring the common phase factor (3.46-3.48). By manually inserting a virtual interface inside the film so that the films at each side of the interface are of the same material, the same matrix calculation method can be used to calculate the electromagnetic components throughout the structure. Unlike the FDTD calculation method, this calculation method is faster and is easier to use.

### **3.4.3 Calculation Results**

The incident angle is chosen as a symmetric  $45^\circ$  for illustration. Any other angle can be calculated by the two methods mentioned above.

Since the electric field of s-polarized incident light has only one non-zero component. The theoretical field distribution calculation and FDTD results of total intensity ( $|E^2|$ ) are shown in Figure 3.19.

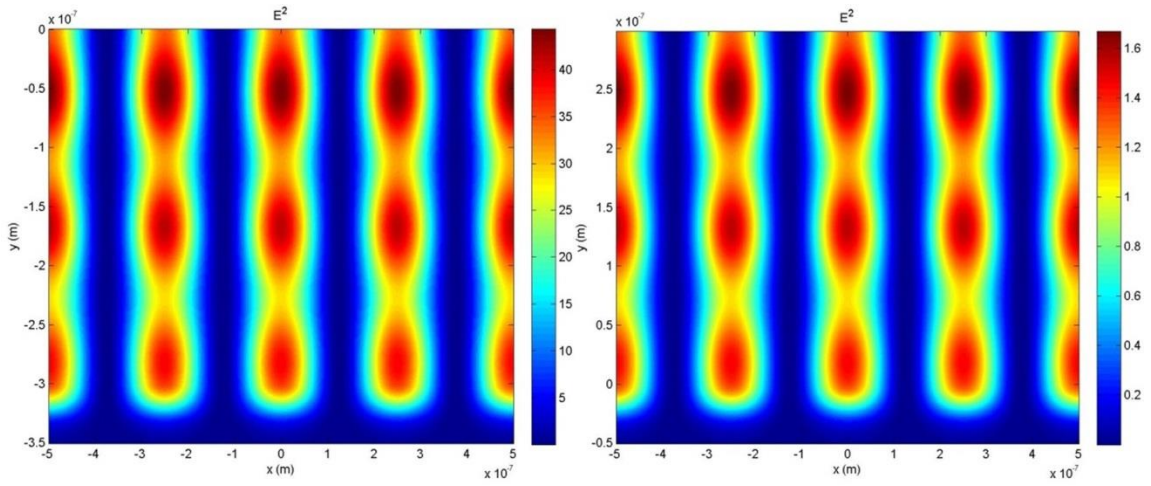


Figure 3.19 Electric Field Distribution of s-polarized symmetric 45 ° incident light (left) theoretical calculation (right) FDTD result

Two electric field components of p-polarized incident light are non-zero, so that the total intensity together with each non-zero component is shown.

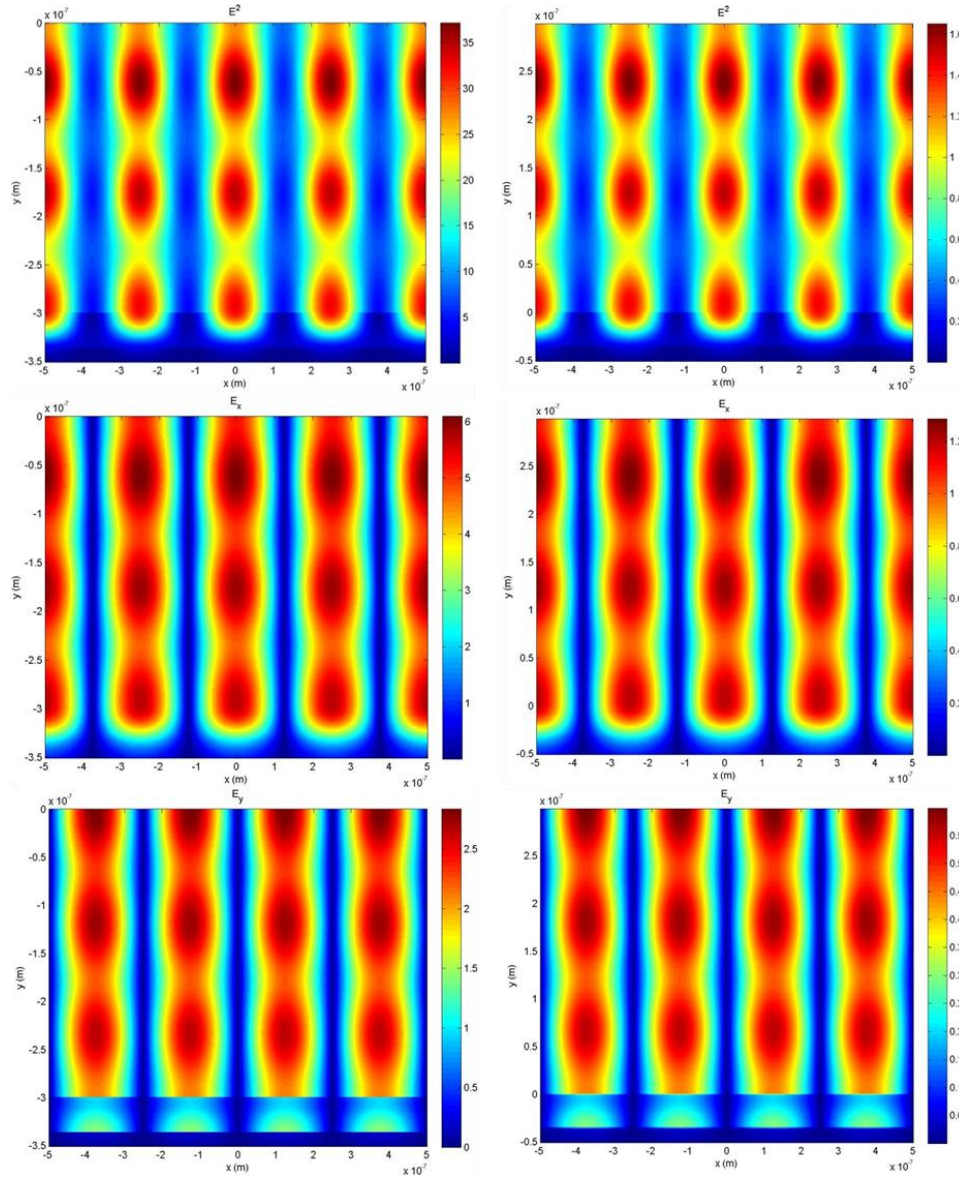


Figure 3.20 Electric Field Distribution of p-polarized symmetric  $45^\circ$  incident light (top left) theoretical result (top right) FDTD result of  $|E^2|$  (middle left) theoretical result (middle right) FDTD result of  $|E_x|$  (bottom left) theoretical result (bottom right) FDTD result of  $|E_y|$

The results of field distribution calculated by the two methods agree very well, as shown in Figure 3.20. The strength of these calculations leads to the pre-experiment

determination of the intensity distribution in the photo-resist, which can be used as a powerful tool of determining the combination of the angles in the experimental setup and polarization of the incident light.

Differences between field distributions between two methods are calculated and shown in Figure 3.21. Field distribution is first normalized to have the maximum intensity of 1 in both methods. Then the value of FDTD results is subtracted from the value of theoretical calculation results at the same coordinate position accordingly as described in Eq. 3.67.

$$\Delta E = |E_{Theoretical}| - |E_{FDTD}| \quad (3.67)$$

Majority of differences are located at the boundary of the graph which indicates the error mainly comes from FDTD simulation. Periodic boundary condition has a numerical error when applying  $k_x$  between each period of simulation window. The PML boundary condition in FDTD could bring a tiny portion of reflection in the FDTD simulation rather than perfectly elimination of reflection from the horizontal direction caused by the simulation setup itself.

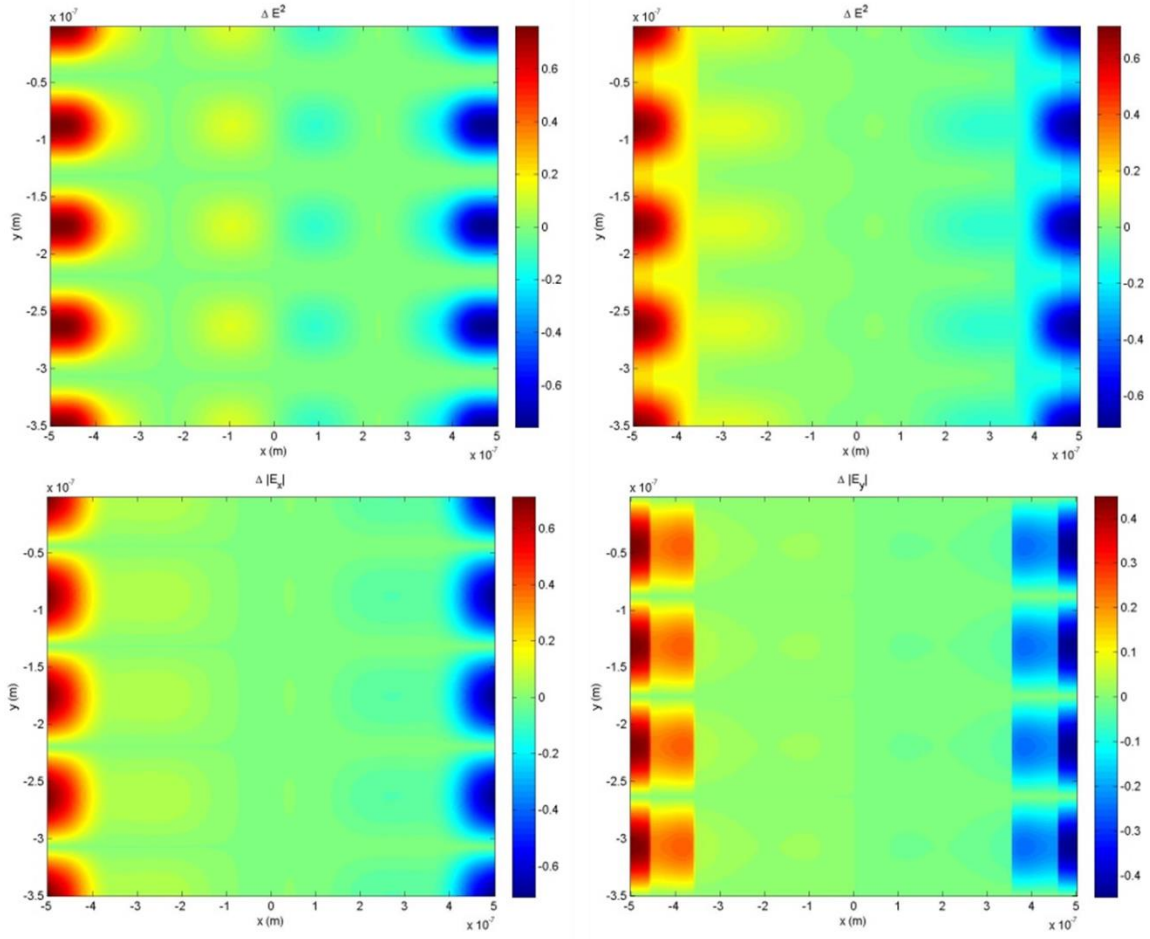


Figure 3.21 Difference of field distribution between FDTD and theoretical calculation (top left)  $|E^2|$  of s polarized light (top right)  $|E^2|$  of p polarized light (bottom left)  $|E_x|$  of p polarized light (bottom right)  $|E_y|$  of p polarized light

## REFERENCES

- [1] K. V. Sreekanth, J. K. Chua, and V. M. Murukeshan, "Interferometric lithography for nanoscale feature patterning: a comparative analysis between laser interference, evanescent wave interference, and surface plasmon interference," *Applied Optics*, vol. 49, pp. 6710-6717, 2010.
- [2] Q. Xie, M. Hong, H. Tan, G. Chen, L. Shi, and T. Chong, "Fabrication of nanostructures with laser interference lithography," *Journal of alloys and compounds*, vol. 449, pp. 261-264, 2008.
- [3] R. Murillo, H. van Wolferen, L. Abelman, and J. Lodder, "Fabrication of patterned magnetic nanodots by laser interference lithography," *Microelectronic engineering*, vol. 78, pp. 260-265, 2005.
- [4] J. Spallas, R. Boyd, J. Britten, A. Fernandez, A. Hawryluk, M. Perry, and D. Kania, "Fabrication of sub-0.5  $\mu\text{m}$  diameter cobalt dots on silicon substrates and photoresist pedestals on 50 cm  $\times$  50 cm glass substrates using laser interference lithograph," *Journal of Vacuum Science & Technology B: Microelectronics and Nanometer Structures*, vol. 14, pp. 2005-2007, 1996.
- [5] F. Kronast, R. Ovsyannikov, A. Kaiser, C. Wiemann, S.-H. Yang, D. Burgler, R. Schreiber, F. Salmassi, P. Fischer, and H. Durr, "Depth-resolved soft x-ray photoelectron emission microscopy in nanostructures via standing-wave excited photoemission," *Applied Physics Letters*, vol. 93, pp. 243116-243116-3, 2008.

- [6] S.-H. Yang, B. S. Mun, N. Mannella, S.-K. Kim, J. B. Kortright, J. Underwood, F. Salmassi, E. Arenholz, A. Young, and Z. Hussain, "Probing buried interfaces with soft x-ray standing wave spectroscopy: application to the Fe/Cr interface," *Journal of Physics: Condensed Matter*, vol. 14, p. L407, 2002.
- [7] M. E. Walsh, "Nanostructuring magnetic thin films using interference lithography," Massachusetts Institute of Technology, 2000.
- [8] D. Wang, Z. Wang, Z. Zhang, Y. Yue, D. Li, and C. Maple, "Effects of polarization on four-beam laser interference lithography," *Applied Physics Letters*, vol. 102, p. 081903, 2013.
- [9] J.-M. Park, K. S. Nalwa, W. Leung, K. Constant, S. Chaudhary, and K.-M. Ho, "Fabrication of metallic nanowires and nanoribbons using laser interference lithography and shadow lithography," *Nanotechnology*, vol. 21, p. 215301, 2010.
- [10] J. Amako, D. Sawaki, and E. Fujii, "Highly efficient diffractive beam splitters surface-structured on submicron scale using deep-UV laser interference lithography," in *SPIE LASE*, 2011, pp. 79210N-79210N-8.
- [11] M. Ellman, A. Rodríguez, N. Pérez, M. Echeverria, Y. Verevkin, C. Peng, T. Berthou, Z. Wang, S. Olaizola, and I. Ayerdi, "High-power laser interference lithography process on photoresist: Effect of laser fluence and polarisation," *Applied surface science*, vol. 255, pp. 5537-5541, 2009.
- [12] J. Lutkenhaus, D. George, D. Garrett, H. Zhang, and Y. Lin, "Holographic formation of compound photonic crystal and nano-antenna templates through laser interference," *Journal of Applied Physics*, vol. 113, pp. 103103-103103-5, 2013.

- [13] X. Wang, D. Zhang, Y. Chen, L. Zhu, W. Yu, P. Wang, P. Yao, H. Ming, W. Wu, and Q. Zhang, "Large area sub-wavelength azo-polymer gratings by waveguide modes interference lithography," *Applied Physics Letters*, vol. 102, pp. 031103-031103-4, 2013.
- [14] M. Bass, C. DeCusatis, J. Enoch, V. Lakshminarayanan, G. Li, C. Mac-donald, V. Mahajan, and E. Van Stryland, "Handbook of Optics, Volume I: Geometrical and Physical Optics," *Polarized Light, Components and Instruments (set)*(McGraw-Hill, Inc., USA, 2010), 2010.
- [15] H. A. Macleod, *Thin-film optical filters*: CRC Press, 2001.
- [16] The code can be sent upon request
- [17] J. Muth, R. Kolbas, A. Sharma, S. Oktyabrsky, and J. Narayan, "Excitonic structure and absorption coefficient measurements of ZnO single crystal epitaxial films deposited by pulsed laser deposition," *Journal of Applied Physics*, vol. 85, pp. 7884-7887, 1999.
- [18] Refractive index database [Online]. Available: <http://refractiveindex.info/>
- [19] D. Aspnes and A. Studna, "Dielectric functions and optical parameters of Si, Ge, GaP, GaAs, GaSb, InP, InAs, and InSb from 1.5 to 6.0 ev," *Physical Review B*, vol. 27, p. 985, 1983.
- [20] (2010). *Optical Parameters of Photoresists*. Available: [http://www.microchemicals.eu/technical\\_information/photoresists\\_optical\\_parameters.pdf](http://www.microchemicals.eu/technical_information/photoresists_optical_parameters.pdf)
- [21] Provided by Brewer Science, InC.

- [22] E. D. Palik, *Handbook of Optical Constants of Solids: Index* vol. 3: Access Online via Elsevier, 1998.
- [23] Q. G. Du, G. Alagappan, H. Dai, H. Demir, H. Yu, X. W. Sun, and C. H. Kam, "UV-blocking ZnO nanostructure anti-reflective coatings," *Optics Communications*, vol. 285, pp. 3238-3241, 2012.
- [24] V. R. Almeida, Q. Xu, C. A. Barrios, and M. Lipson, "Guiding and confining light in void nanostructure," *Optics letters*, vol. 29, pp. 1209-1211, 2004.
- [25] F. Solutions, "Lumerical Solutions Inc," *Vancouver, British Columbia, Canada* (Accessed January 2013), <http://www.lumerical.com/tcad-products/fdtd>, 2003.
- [26] X. Han, X. Ji, H. Wen, and J. Zhang, "H-Shaped Resonant Optical Antennas with Slot Coupling," *Plasmonics*, vol. 7, pp. 7-11, 2012.
- [27] G. Xiao, X. Ji, L. Gao, X. Wang, and Z. Zhou, "Effect of dipole location on profile properties of symmetric surface plasmon polariton mode in Au/Al<sub>2</sub>O<sub>3</sub>/Au waveguide," *Frontiers of Optoelectronics*, vol. 5, pp. 63-67, 2012.

## **Chapter 4 Fabrication of ZnO Gas Sensor Using Laser Interference Lithography**

In this chapter, the fabrication process of ZnO gas sensors is covered. The experimental setup of laser interference lithography with different photo-resist periodic line structures is shown. The process flow is then covered. A photo-mask for introducing metal contacts by lift-off technique was made and discussed. The gas sensor prototypes are shown, and electric characterization of the sensors was made. Finally, qualitative gas sensing tests under vacuum with and without an external heater were made and shown. Quantitative measurements were not made due to time constraints, but the limitation of current measurement system. These results show the practicability of the method.

### **4.1 Experiment Setup of laser interference lithography**

An exposure setup was made for each polarization. A Coherent Genesis CX 355-100 SLM UV laser was used for laser interference lithography. The laser beam has a tunable output power up to 100mW and a vertically polarized output. Both setups were made on optical breadboards. The p-polarized setup consists of a vertical supporting post and two horizontal posts holding mirror and sample stage. A Quint Graphics iGaging 14'' digital protractor was used for adjusting and measuring angles. The s-polarized setup consists of two stages for a mirror and sample holder. A rotation stage is used as sample holder with double sided tape on top, preventing the sample from falling. The sample holder is set on a 360

degree rotation stage fastened on a 1 dimensional slide rail. The mirror holder is set on another rotation stage fastened on a linear translation rail. Figure 4.1 illustrates the two setups.

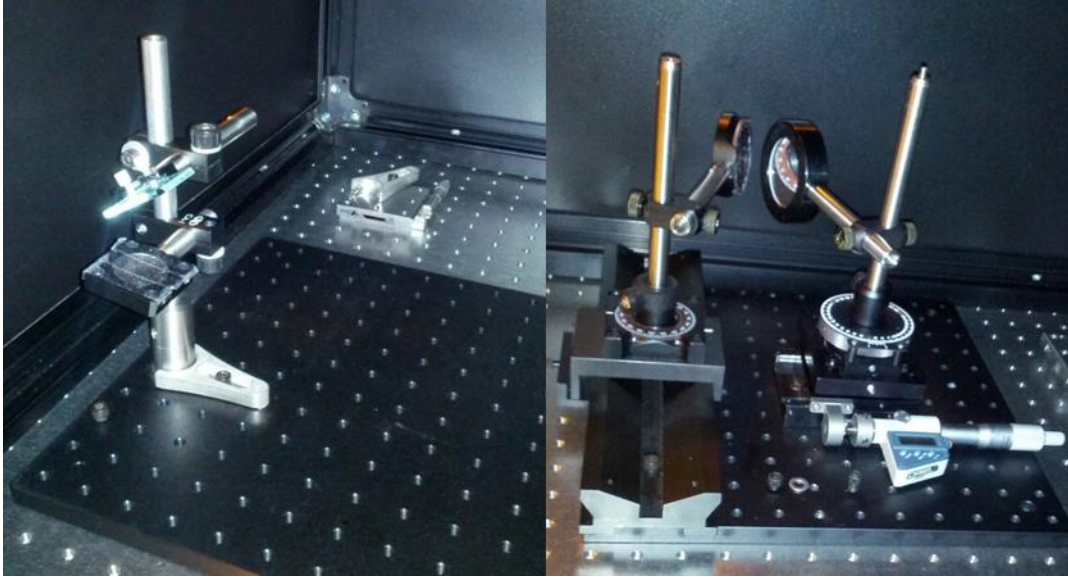


Figure 4.1 Photographs of two laser interference lithography setups for (left) p polarized (right) s polarized

A Thorlabs PM100D power meter was used for measuring the power of light at the mirror and sample surface in the NCSU Nanofabrication Facility (NNF) cleanroom. A Newport 1815-C power meter with 883-uv detector was used in Dr. Escuti's lab for the same purpose. A paper was placed on the sample stage as a visual aid while adjusting the power. Light directly from the laser, and light reflected from mirror form a higher intensity region on the paper. By blocking either light, the remaining intensity indicates the power of the other

part projected onto the state. The power is adjusted correctly when areas that containing only one light source both have the same intensity. This method is performed in addition to the power meter to have a more direct way of seeing light intensity distribution on the exposure area and overcome the difficulty of adjusting the power meter height. Figure 4.2 shows the experimental process of adjusting power using paper.

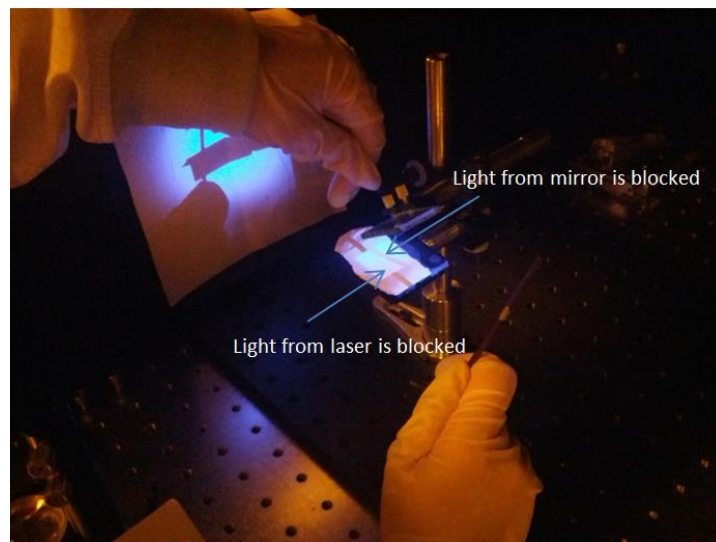


Figure 4.2 Photograph of power adjustment by using paper

## 4.2 Patterned photoresist with laser interference lithography

By adjusting the combination of angles ( $\theta, \alpha$ ), periodic structures with a variety of periods ranging from 250nm to 2 $\mu$ m can be made. Figure 3 shows optical microscopic images of photo-resist structures of one-dimensional lines made by a single exposure with periods of 482nm, 620nm, 976nm and 1870nm.

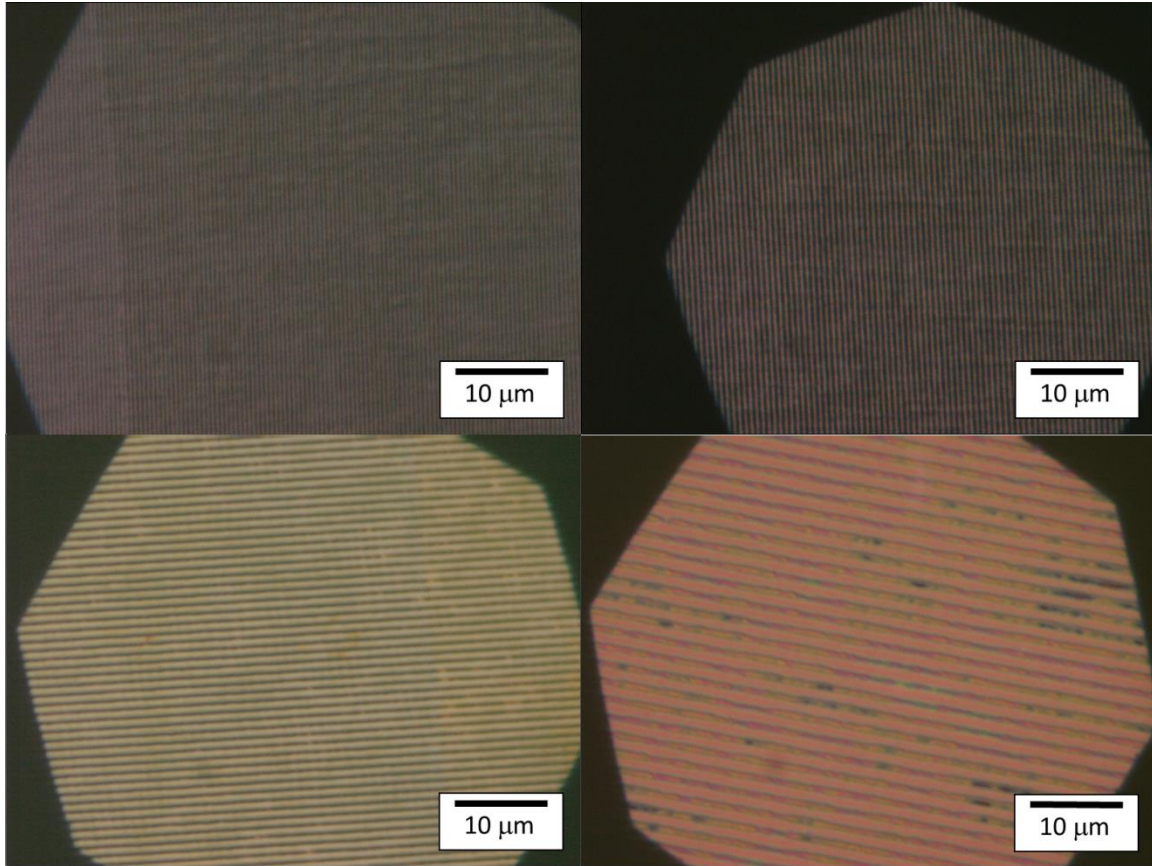


Figure 4.3 Microscopic images of 1 dimensional lines with period of (top left) 482nm (top right) 620nm (bottom left) 976nm (bottom right) 1870nm

All periods shown in Figure 4.3 were exposed using p polarized setup. These one dimensional structures are good optical gratings which show color difference with different view angle because of diffraction effect. Figure 4.4 (a) shows such color change of diffraction pattern on a 1 inch glass sample. Figure 4.4 (b) shows the SEM image of 482nm period line structure. When the period is not smaller than visible range, such effect is expected and can be used as an indicator of the structure quality. The diffraction pattern becomes brighter with higher contrast of the pitch.

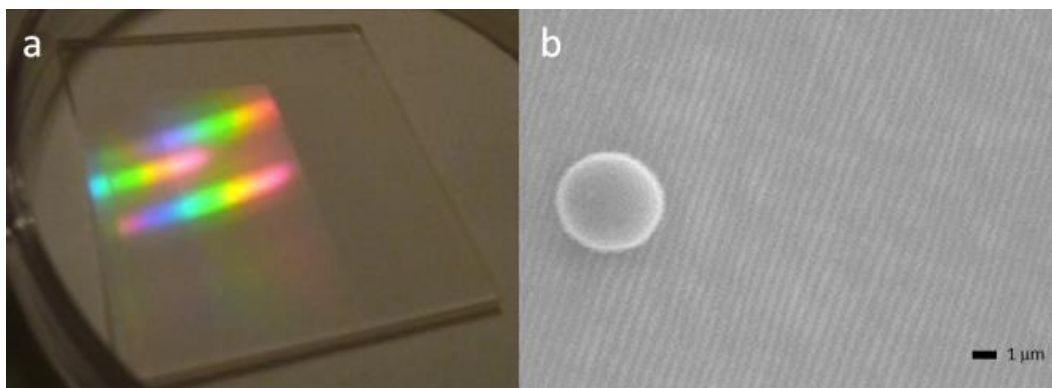


Figure 4.4 (a) Diffraction pattern of 1 inch sample (b) SEM image of 482nm period lines

When the period is less than 400nm, the structure is below optical microscope resolution. A Digital Instruments Dimension 3100 atomic force microscope (AFM) is used to measure the period of such a case is shown in Figure 4.5. The height of the structure is also measured by AFM.

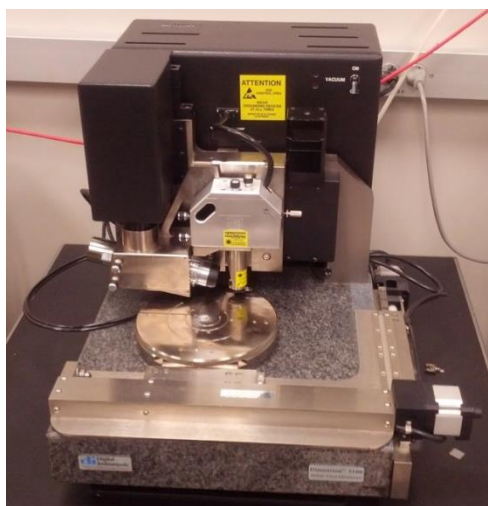


Figure 4.5 Photograph of AFM

The AFM images of different period of photoresist pattern are shown in Figure 4.6. The exposure parameters were adjusted for different combination of angles to have a deep photoresist valley indicating good contrast. The photoresist was patterned by the laser interference lithography up to close 300nm deep.

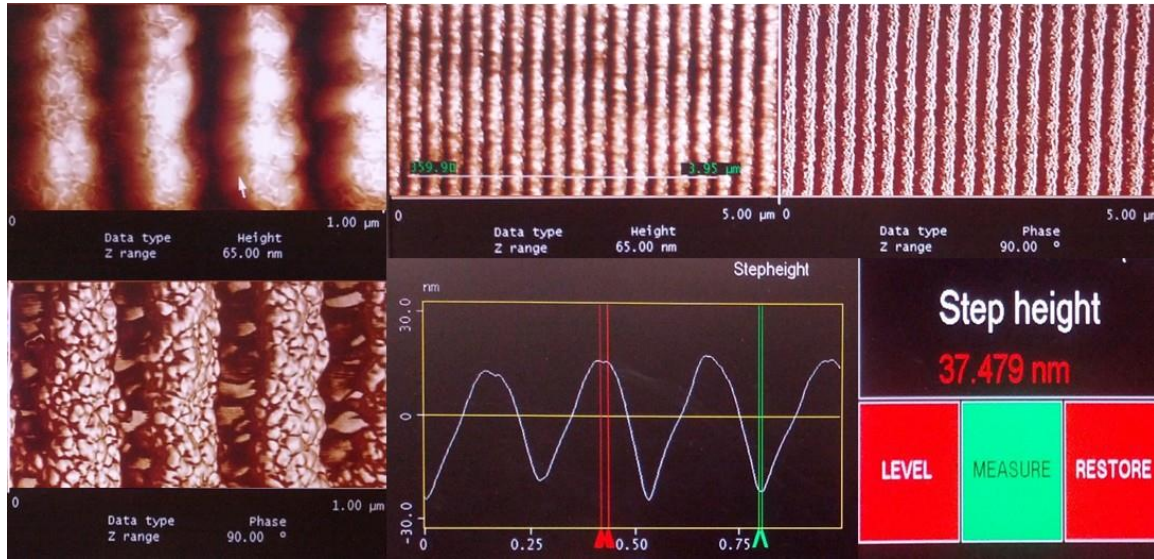


Figure 4.6 AFM images of photoresist nano-line with period of 263nm

The s-polarized setup was used for the fabrication of small period structures. Figure 4.7 shows the AFM results of photoresist patterns with large periods of 1.29μm and 1.94μm. The p-polarized setup was used for these large period structures.

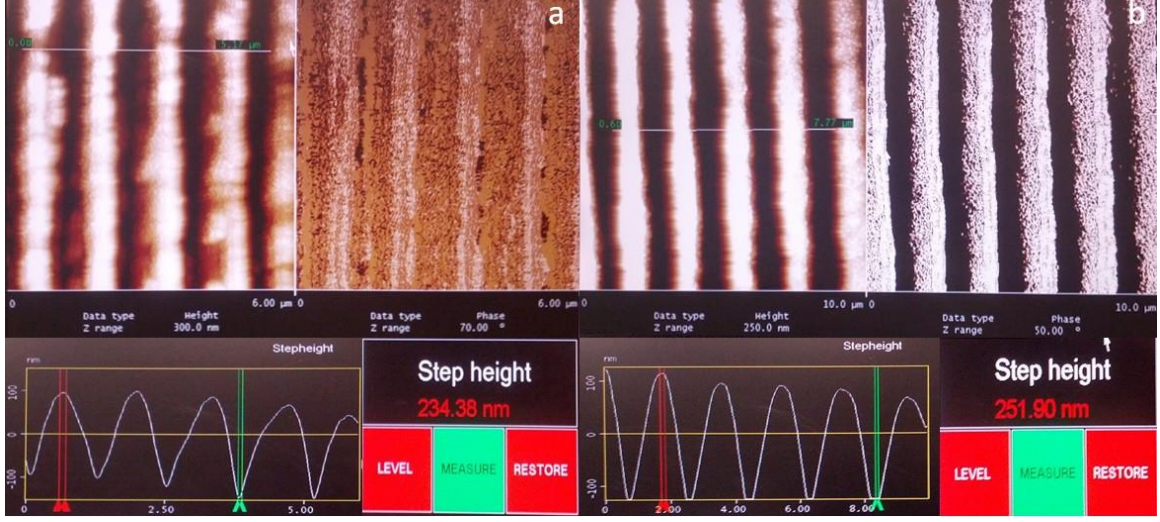


Figure 4.7 AFM images of photoresist nano-line with period of (a) 1.29 $\mu$ m and (b) 1.94 $\mu$ m

The height to period ratio ( $\rho$ ) indicates the quality of the exposure. With the same period, a better contrast results in a higher height to period ratio. There are theoretical limits of this height to period ratio, which can be determined by the field distribution calculation discussed in Chapter 3 for specific incident angle combinations. The ratios of the three structures in Figure 4.6 and Figure 4.7 are:

$$\rho_{263nm} = \frac{34.479nm}{263nm} = 0.131 \quad (4.1)$$

$$\rho_{1.29\mu m} = \frac{234.38nm}{1.29\mu m} = 0.181 \quad (4.2)$$

$$\rho_{1.94\mu m} = \frac{234.38nm}{1.94\mu m} = 0.130 \quad (4.3)$$

The height of photoresist structures with large periods allows the use of RIE processing to transfer the pattern to an underneath layer. The first device prototype was made by this method. However, the height of the smaller period structures is not enough for an RIE process to be used. A wet etch or vapor etch approach can be used to complete the pattern transfer. In both cases, the thickness of the photoresist needs to be around the exposure depth to obtain optimal effect in pattern transfer. AZ5214E photoresist is used for processing in our group, which forms a thickness of 1500nm at a spin speed of 4700rpm. The normal AZ5214E photoresist was diluted with its solvent, PGMEA, to reduce the thickness. Table 4.1 and table 4.2 contain the thicknesses of diluted photoresist with different spin speeds.

Table 4.1 Thickness of 1:1 (AZ5214E: PGMEA) volume ratio diluted photoresist of varied spin speed

Spin Speed (rpm)	Thickness (nm) measured by AFM	Thickness (nm) measured by DEKTEK
3000	256	284.4
4000	252	231.5
5000	222	228.4
6000	213	232.2

Wide-15B Anti-reflection coating from Brewer Science was also studied. ARC is widely used to get better contrast and higher structure height in laser interference lithography processes. The thickness vs. spin speed relation of the ARC is shown in table 4.2. As discussed in chapter 3, thin film antireflection coatings act mainly as interference

antireflection coatings, in which case the thickness needs to be in the right range. This is important since the reflection could be even enhanced with a wrong ARC thickness.

Table 4.2 Thickness of ARC of varied spin speed

Spin Speed (rpm)	Thickness (nm) measured by AFM
3000	136
4000	84
5000	81
6000	75

The height to period ratio needs to be further optimized by either employment of an ARC layer or a thin film of ZnO (or other metal oxide sensing material) with designed thickness acting as interference type thin film antireflection layer. Detail of such a design has been discussed in Chapter 3.

Laser interference lithography can be used to define two-dimensional periodic structures as well by multiple exposures. By expanding the theoretical field distribution to three dimensions, the model can be used as a simulation method for complex structures for experimental design. A simple idea is to have a double exposure with same exposure parameters and a 90-degree rotation of the sample. Fig 4.8 illustrates two dimensional photoresist bumps by double exposure laser interference lithography with a period of 482nm. Such structures can be used as plasmonic devices by coating a thin film of gold on top.

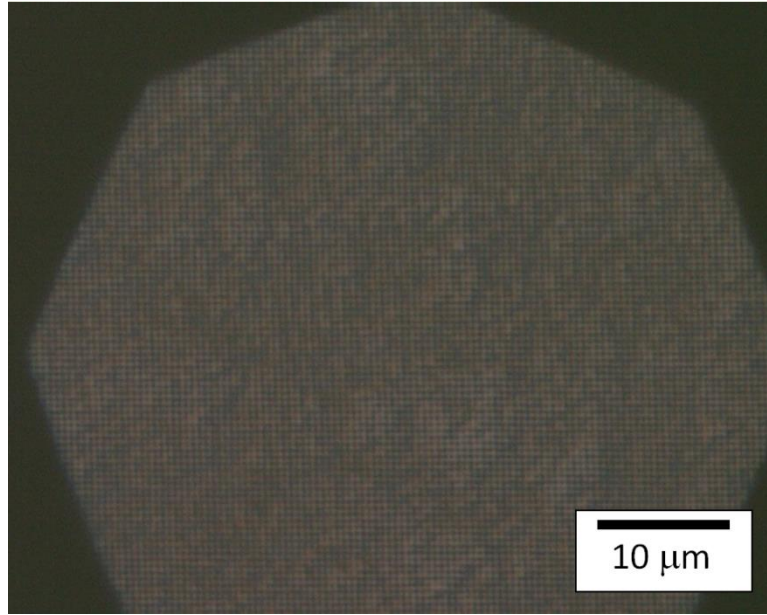


Figure 4.8 Microscopic images of 2 dimensional bumps with period of 482nm

### **4.3 Process flow for metal oxide nanowire gas sensor fabrication**

Four device structures of chemical resistor type metal oxide gas sensors are shown in Figure 4.9. Thin film metal oxide gas sensors with and without textured metal oxide layers are shown in Figure 4.9 (a) and (b). To reduce the thermal loss to the substrate, the devices can be put onto silicon nitride membrane which has low thermal conductivity as shown in in Figure 4.9 (c) and (d).

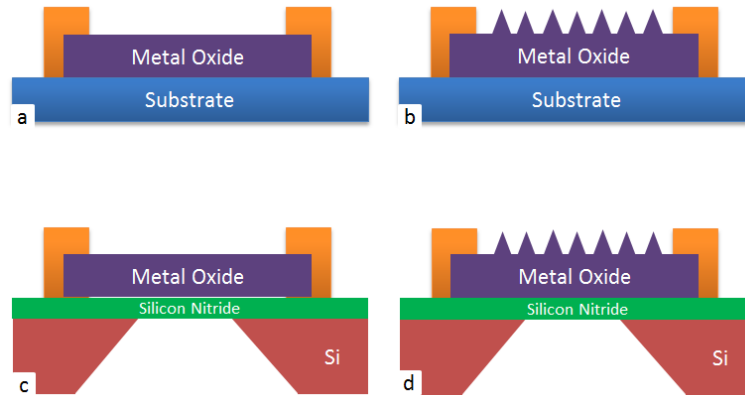


Figure 4.9 side view of device structures

Two main processes are involved to make the final device in Figure 4.9 (d). One process is for the device in Figure 4.9 (b) while the other is the process for silicon nitride membranes. The first process flow is shown in Figure 4.10. Each step is discussed afterwards.

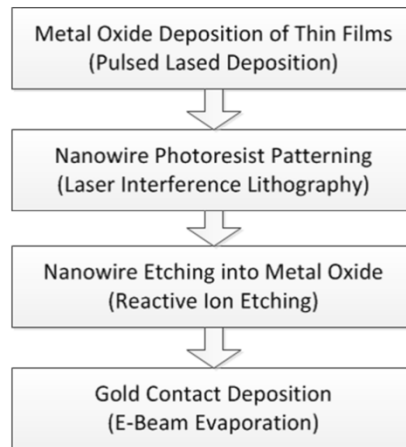


Figure 4.10 Nanowire device fabrication process

A pulsed laser deposition (PLD) system is used for metal oxide deposition. A high power laser beam is focused on the target inside of a vacuum chamber and causes the target material to evaporate in a plasma plume. The plasma then recombines on the substrate, producing a thin layer of the target material. The high energy density makes such a system capable of depositing hard and high heat resistant material. The high energy density also leads to a plasma plume, which offers the deposition system a high deposition rate and minimizes contamination. The system can operate in ultra-high vacuum or in the presence of a background gas, such as oxygen when depositing metal oxide to fully oxygenate the deposited film. A schematic of a PLD system is shown in Figure 4.11. [1]

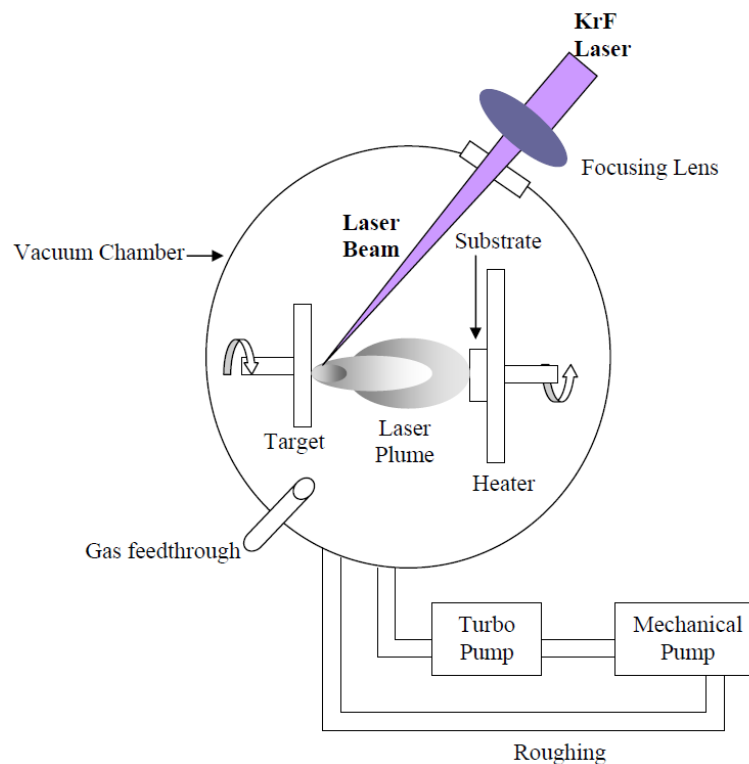


Figure 4.11 Schematic of PLD system [1]

A 300nm thick diluted photo-resist film (AZ5214E and PGMEA with volume ratio 1:1) is spin coated on top of the deposited oxide film. Laser interference lithography is then done with the Lloyd's mirror interferometer setup by using a 355nm wavelength laser (Coherent Genesis CX355-100 SLM, TEM00 mode). A Quint Graphics iGaging 14'' digital protractor is used for adjusting and measuring angles of the p-polarized setup. Rotation mounts with readings of angles are used for the s-polarized setup. Exposure dose and development times were adjusted with different incident angles. A subsequent RIE process is optional according to the etching technique used for pattern transfer of the oxide layer. For a wet etch process, a short RIE process of the photo-resist is recommended to make sure the unwanted photoresist is fully removed and the oxide has a good contact with the chemical used for wet etching.

The patterned photoresist is then used as a mask for pattern transfer into the metal oxide layer. Three etching methods are available, reactive ion etch, chemical vapor etch or chemical wet etch. An RIE process with  $\text{BCl}_3$  gas was used for the first prototype of ZnO gas sensors. Figure 4.12 shows the optical microscopic image with photoresist on top after RIE processing. The photoresist was then removed using acetone. An AFM measurement was performed for the etch depth. The AFM images are shown in Figure 4.13.

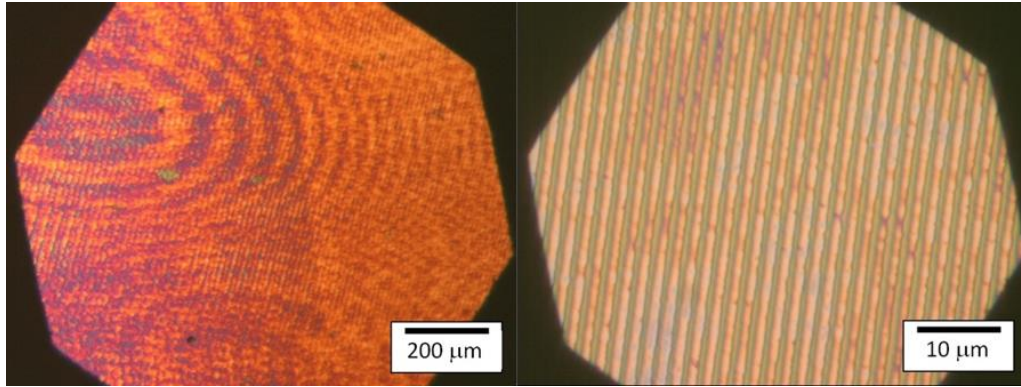


Figure 4.12 Optical microscopic images of patterned ZnO film without removing photoresist

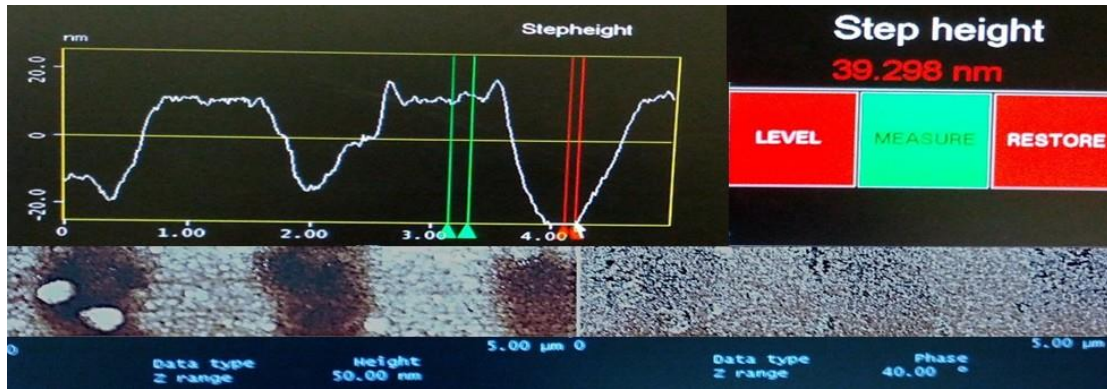


Figure 4.13 AFM images of etched ZnO film

The contacts were deposited by using a standard lift-off method. A 1.5  $\mu\text{m}$  photoresist (AZ5214E) layer was spin coated on the patterned ZnO film. The photoresist was then exposed using a photo-mask designed with different shapes and was tuned to negative type. A gold film of 171nm thick was coated on top with E-beam deposition. Figure 4.14 shows the measured thickness of the gold contact. Details of contact shapes are discussed in section 4.4.

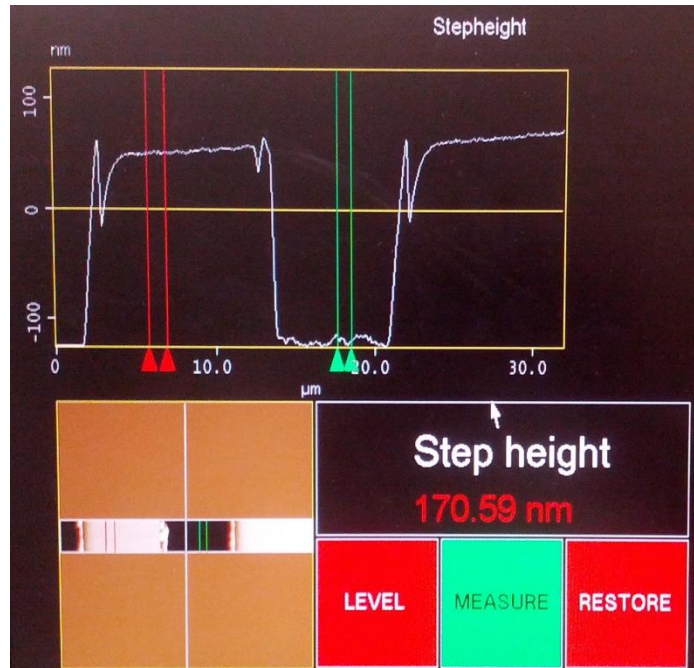


Figure 4.14 AFM image of gold contact thickness

The process of silicon nitride membrane fabrication was developed long before in our group. It is now a standard fabrication process in the NNF cleanroom. Figure 4.15 shows the fabrication process of silicon nitride membranes.

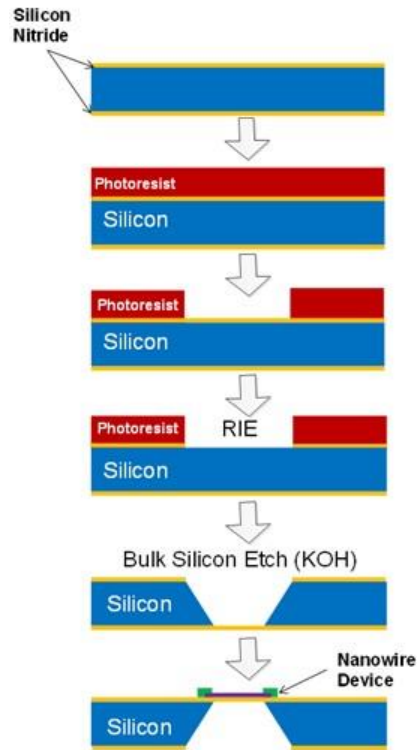


Figure 4.15 Silicon nitride membrane process flow

The thickness of the silicon (with  $\langle 100 \rangle$  orientation) between two silicon nitride films is  $212 \mu\text{m}$ . The etched silicon has a slope of  $54.74$  degrees. Several silicon nitride membranes were made by this method for future device fabrication. When cleaning the sample after KOH etching, it is important to make sure that all KOH is removed. Otherwise, nucleation of KOH on the film will be observed under an optical microscope. An optical microscopic image of the silicon nitride membrane is shown in Figure 4.16 (a). An optical microscope image of a silicon nitride membrane with KOH residue coated with a ZnO film is shown in Figure 4.16 (b).

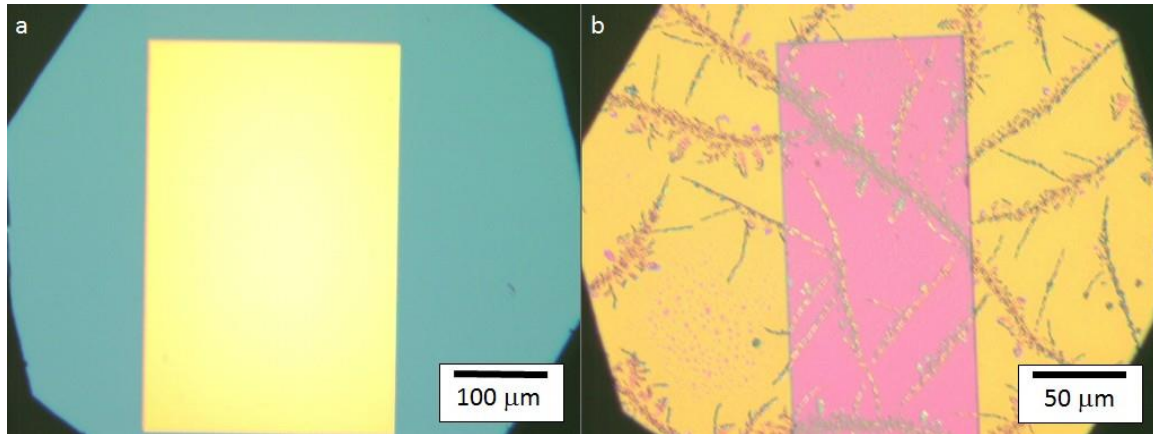


Figure 4.16 microscopic image of (a) silicon membrane (b) ZnO on top of silicon membrane with KOH residual

#### 4.4 Mask Design of Metal Oxide Gas Sensor

A photomask was designed by using software LASI 7. The mask was fabricated by photo science, Inc. with product code F10CS 4060. The mask is used for introducing metal contacts, isolating devices and the fabrication of silicon nitride membranes. Figure 4.17 (a) shows the full mask design, which consists of 9 areas marked with numbers. Figure 4.17(b) shows the compact design of the mask. Areas 1, 6 and 8 are used for silicon nitride membrane fabrication. Areas 2, 5 and 7 are used for introducing metal contacts. Areas 3 and 4 are used for device isolation. Area 9 is used for four-point probe measurement.

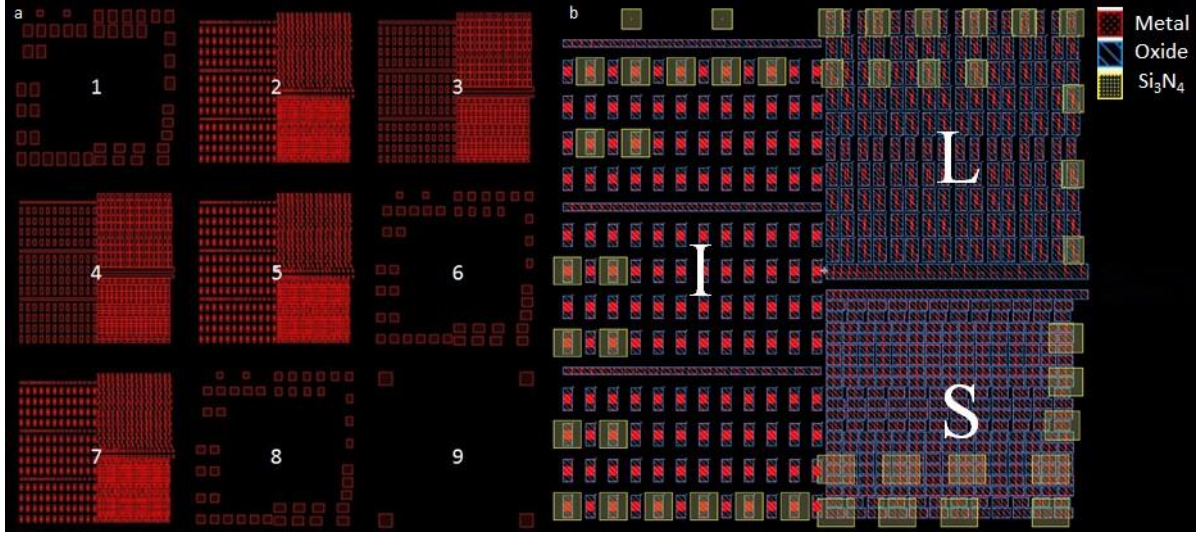


Figure 4.17 (a) Full mask design (b) Compact view of the mask

Three metal contact categories were designed: square contact, single digit contact and multiple interdigitated contact. They are placed into three sections shown in Figure 4.17(b) marked with capital letters I (interdigitateds), L (single digit) and S (square) for each type.

#### 4.4.1 Square contacts

The square contacts have the simplest shape. They are kept in one same size with only varied distance (d) between two contacts of each device. Each square contact is  $150\mu\text{m}$  wide,  $200\mu\text{m}$  tall. Figure 4.18 illustrates the morphology of a set of square contacts. Each line in section S contains sets with same distance (d) value. The distances between the two contacts are set according to Table 4.3. Lines are counted from the bottom of the section. The

five lines are then repeated in a reversed order three times. There are 20 lines in total in section S.

Table 4.3 Distance table of square contact

Line number	Distance (d) ( $\mu\text{m}$ )
1	100
2	50
3	30
4	20
5	10

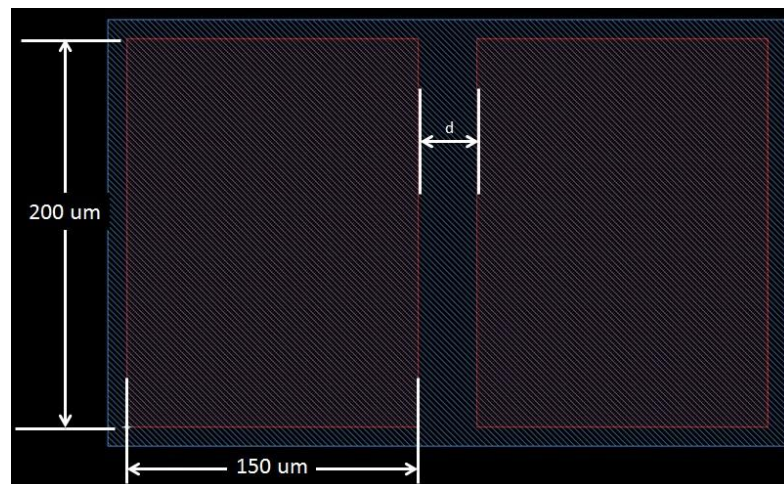


Figure 4.18 Schematic of a set of square contacts

#### 4.4.2 Single digit contacts

Single digit contacts are designed to measure the performance between two digits in comparison with multiple interdigitated contact devices. One set of single digit contacts contains two identical contacts with 180-degree rotational symmetry. Each contact consists of two parts: a  $150\mu\text{m} \times 150\mu\text{m}$  square and a  $10\mu\text{m} \times 190\mu\text{m}$  digit. The distance between the two digits ( $d$ ) is varied according to Table 4.4. Lines are counted from the bottom of the section. Each line in section L contains sets with same distance ( $d$ ) value. Figure 4.19 illustrates the morphology of a set of single digit contacts. The five lines are then repeated once. There are 10 lines in total in section L.

Table 4.4 Distance table of single digit contact

Line number	Distance ( $d$ ) ( $\mu\text{m}$ )
1	10
2	20
3	30
4	50
5	100

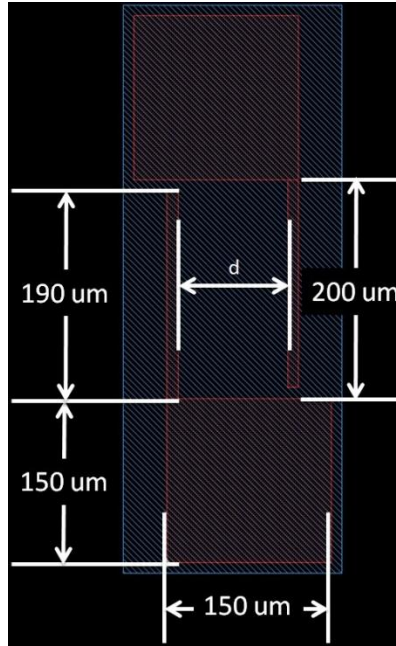


Figure 4.19 Schematic of a set of single digit contacts

#### 4.4.3 Multiple interdigitated contacts

Multiple interdigitated contact devices are widely used in nanowire devices. The multiple interdigitated contacts minimize the effect of disconnection of single nanowire. One set of multiple interdigitated contacts has two identical contacts with a 180-degree rotational symmetry. Each contact consists of two parts: a  $200\mu\text{m} \times 150\mu\text{m}$  rectangle and multiple  $10\mu\text{m} \times 190\mu\text{m}$  digits. The digits are separated with distance ( $d$ ) and repeated from the left end to right with the maximum allowed number of periods. The value of  $d$  is varied according to Table 4.5. Lines are counted from the bottom of the section. Each line in section I contains sets with the same distance ( $d$ ) value. Figure 4.20 illustrates the morphology of a set of multiple interdigitated contacts. The four lines together with a line of single rectangular

contacts for contact resistance measurement are then repeated three times. There are 12 lines in total in section I.

Table 4.5 Distance table of single digit contact

Line number	Distance (d) ( $\mu\text{m}$ )	Number of digits (on single contact)
1	15	4
2	10	5
3	5	7
4	3	7

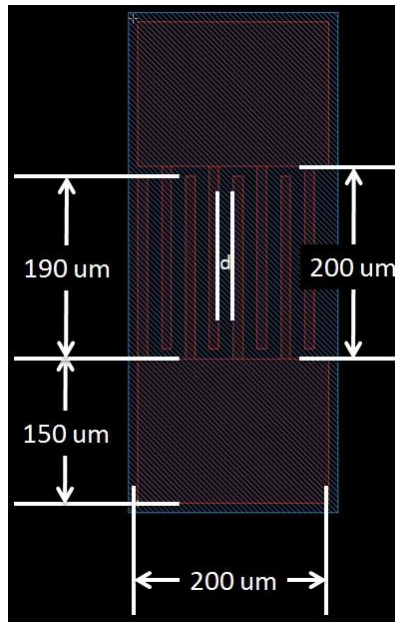


Figure 4.20 Schematic of a set of multiple interdigitated contacts

#### **4.4.4 Silicon nitride membrane**

Two sizes of silicon nitride membranes were designed. One covers the whole device (section 1 in Figure 4.17(a)) whereas the other only covers the digit part of the device (sections 6 and 8 in Figure 4.17(a)). The size of silicon nitride membrane mask is calculated according to the KOH etching process. A 212 $\mu$ m space is left out of the desired size because the etching process starts from the bottom. The silicon nitride membranes are put surrounding the center of the mask to leave enough space for the sample to mount on spinner for further photolithography processing

#### **4.4.5 Number system**

A number system was designed for notation of the d value on the mask. The number system is shown in Figure 4.20. A number was put on the top right outer corner of the device every two sets of contacts.


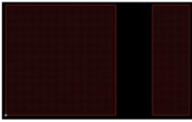








Mask Symbol	Number	Mask Symbol	Number
	1		6
	2		7
	3		8
	4		9
	5		10

Figure 4.21 Number system on mask

#### 4.5 Zinc Oxide Gas Sensor Prototype

A zinc oxide gas sensor prototype was made according to the process discussed in section 4.3. Figure 4.21 shows the photographs of the sensor prototypes.

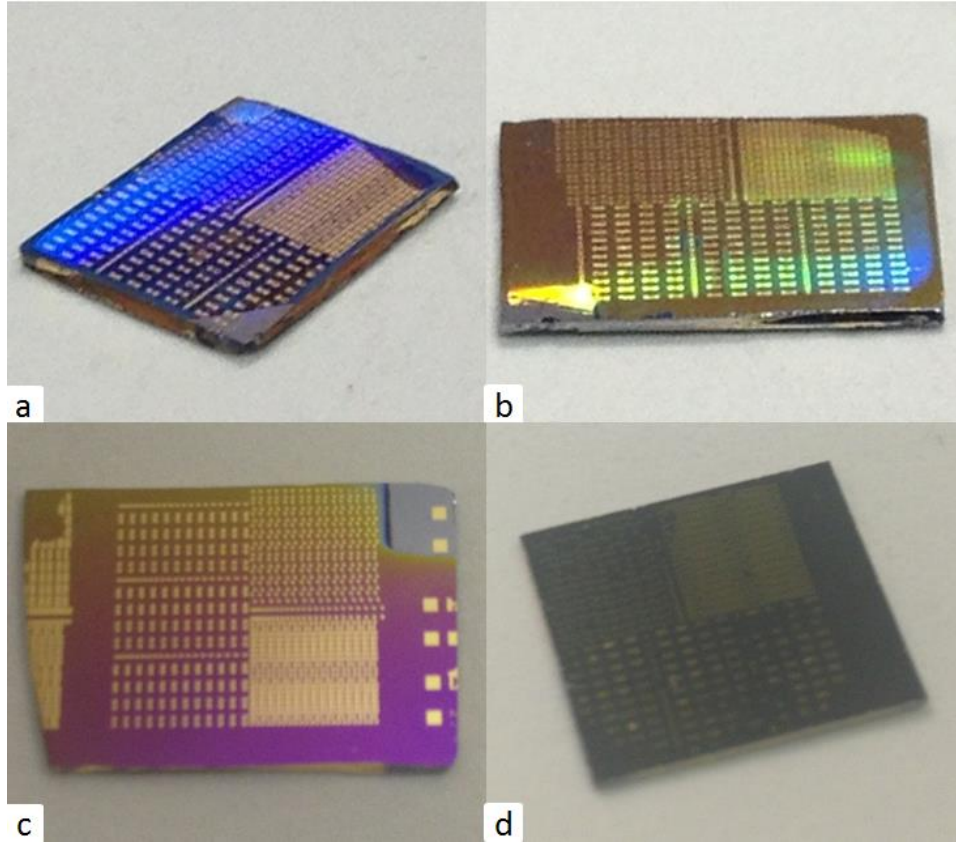


Figure 4.22 Images of device chips with (a) 100nm and (b) 160nm thick ZnO, (c) ZnO thin film and (d) plain Silicon substrate.

The gas sensor prototypes were made to mainly verify the validity of the fabrication process and to test the etching speed. AFM measurements were performed three times to test the etching speed: before RIE, after RIE with photo-resist remaining and after RIE with photo-resist removed by acetone. Table 4.6 contains the measured step height of the three measurements.

Table 4.6 Step height measurements

Measurement	Step height (nm)
Before RIE	260.35
After RIE with PR remained	176.80
After RIE without PR	40.75

The etching speed can then be calculated for both positive photo-resist (AZ5214E) and ZnO. The RIE etching process lasts 8 minutes. The calculated etching speed therefore is 15.494nm/min for the positive photoresist and 5.094nm/min for ZnO. Figure 4.22 shows optical microscopic images for the square contact devices. Figure 4.23 (a) and (b) show the optical microscopic images for single digit and multiple interdigitated contact devices. Figure 4.23 (c) shows SEM image of close up of interdigitated contact device. Figure 4.23 (d) shows the SEM image of fabricated ZnO wires on silicon substrate.

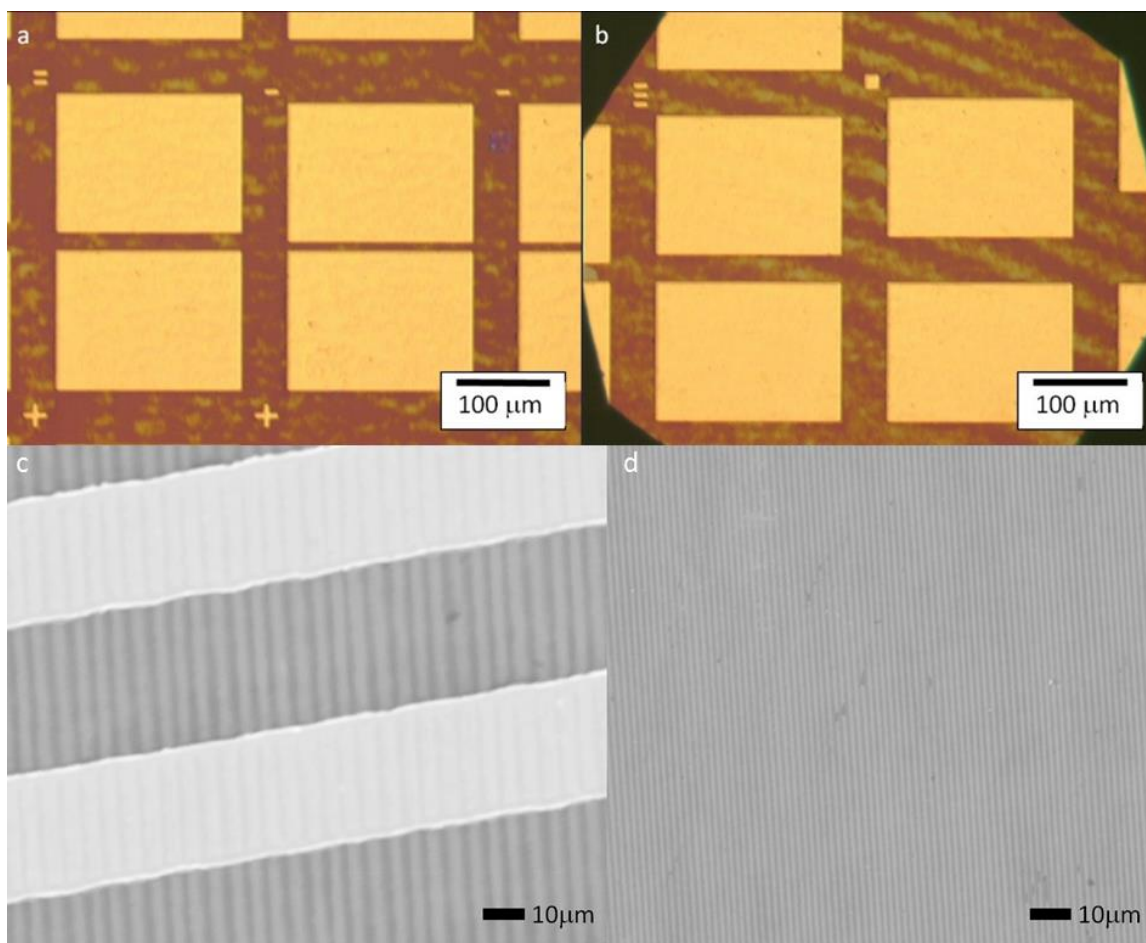


Figure 4.23 Microscopic images of square contact devices (a) devices with 20μm, 10 μm distance (b) devices with 30μm, 50 μm distance (c) SEM image of close up of interdigitated contact device (d) SEM image of fabricated ZnO wires

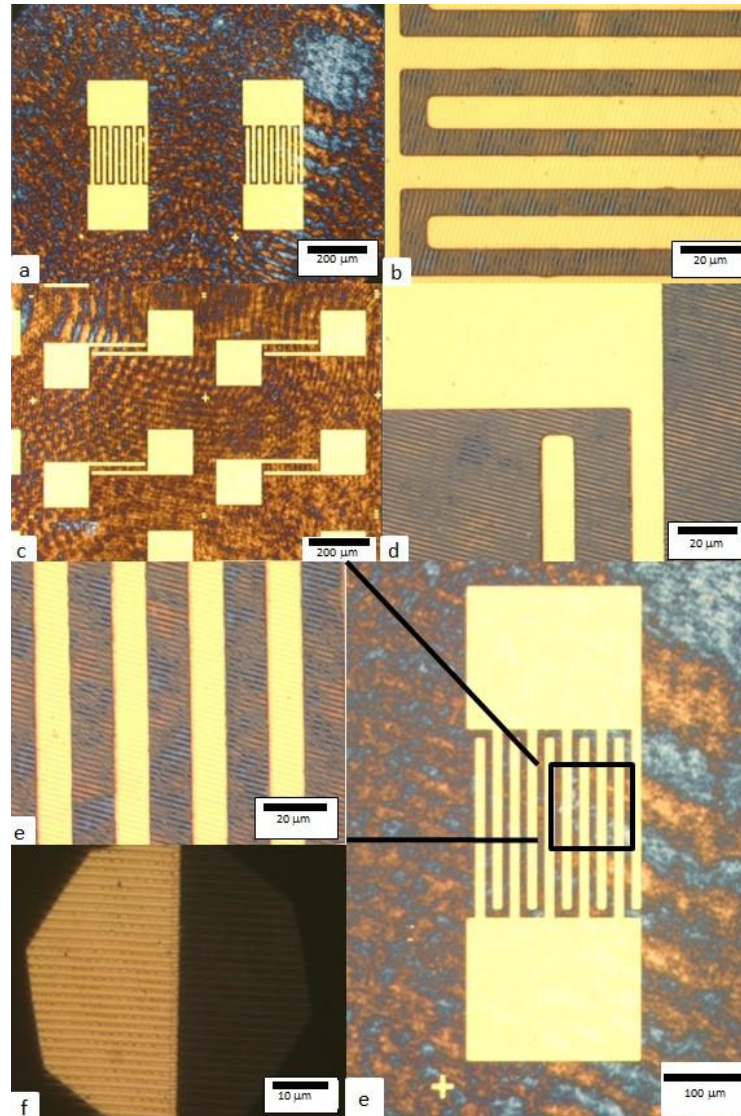


Figure 4.24 Microscope images of devices (a) Interdigitated contact width of 10um. (b) Close up of 10um interdigitated contact connected by ZnO nanowire pattern. (c) Single digit devices with 10um (left) and 20um (right) spacing. (d) Close up on single digit contacts showing the ZnO nanowires. (e) Detailed close up of a 10um interdigitated device (f) Phase Shift on gold edge of laser interference patterned nanowires

Phase shift is a unique phenomenon of the p polarized laser interference lithography setup where the periodic lines shift by half period at the edge of gold as shown in Figure 4.24 (f). The effect is caused by the refractive index of each layer which cause  $\pi$  in phase change. Same effect has been seen on silicon nitride membrane edge. Using phase shift effect of the wires in fabrication, a mismatch of wires at the metal contact may result in an additional heating effect. The wires with mismatches are expected to have an effective width smaller than half of the period.

## **4.6 Device characterization**

The electric properties of the sensor prototypes were measured. Qualitative gas sensing tests were conducted with and without an external heater.

### **4.6.1 Measurement system**

The devices were characterized by using an HP 4142B Modular DC Source/Monitor shown in Figure 4.25 (a). A connection box, shown in Figure 4.25 (b), allows two measurements to be taken spontaneously using two ports.

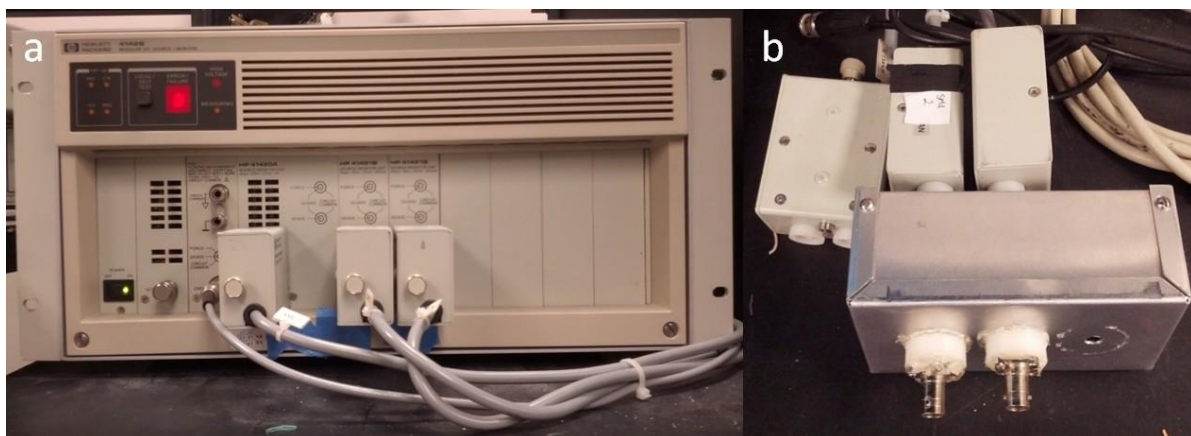


Figure 4.25 Photograph of (a) HP 4142B (b) Connection box

A custom probe station consists of four micromanipulators to make electrical contacts to the device contacts. The probes are connected to the HP 4142B for signal processing. A LABVIEW program is used on a computer to control the HP 4142B and used for data analysis. A UV LED holder was mounted to the left of the sample station for testing of the photo-electrocatalytic effect. The illuminated area was marked a black circle on the sample stage. The power supply shown in Figure 4.26 (a) was used for the UV LED. Figure 4.26 (b) shows the photograph of the probe station.

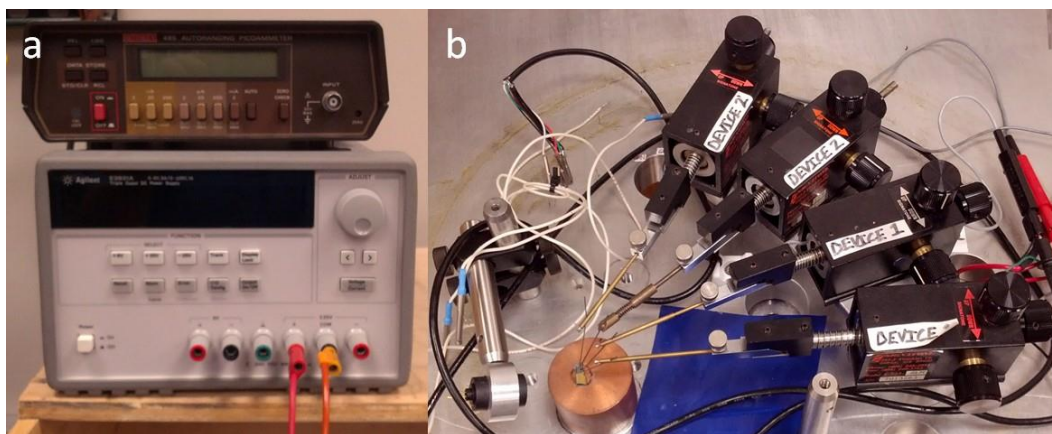


Figure 4.26 Photograph of probe station

A bell jar was used for gas sensor testing, which seals the whole setup inside [2]. The bell jar was sealed to an aluminum plate with grease when the conducting gas sensing test in vacuum Figure 4.27 (a) and lifted by three aluminum plates when under atmospheric condition shown in Figure 4.27 (b) and (c). A commercial ozone detector (e2v metal oxide semiconductor (MOS) gas sensor evaluation kit) was used for gas sensor testing spontaneously for detection. A GreenTech GT50 ionic air purifier, which generates activated oxygen (ozone) at safe, user-controlled levels ( $<0.05\text{ppm}$ ) was used as an ozone generator and is shown in Figure 4.27 (d).

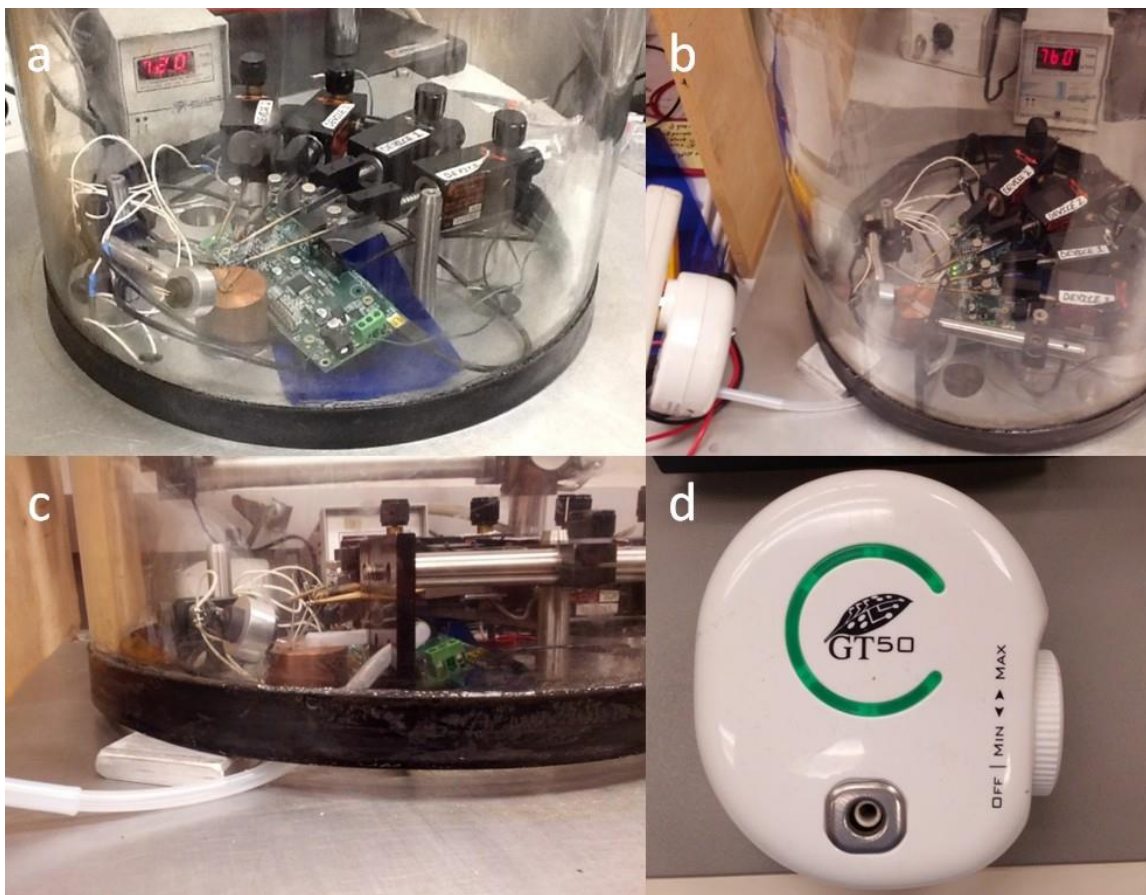


Figure 4.27 Photograph of (a) bell jar system under vacuum (b) top view (c) side view of lifted bell jar for atmosphere gas sensing (d) GreenTech GT50 air purifier for ozone generation

#### 4.6.2 Electrical properties of the sensor prototype

Sensor prototypes were tested under three circumstances:

- a) Atmosphere pressure at room temperature
- b) Under vacuum at elevated temperature with heater only
- c) Under vacuum at room temperature illuminated with UV LED without heater

First at room temperature under normal atmosphere the resistance of the sensors was measured. Three I-V curve measurements were taken on each device with 90s time set for each period under circumstance (a). The voltage was set to sweep from high (10V) to low (0.001V). The voltage was kept constant 0.001V after the sweep was finished of each measurement period. From the I-V measurement two types of I-V curves were observed, almost ohmic resistive behavior and devices that had a diode like nature. A linear relation of I-V curve is defined as resistor like. An I-V curve that has a slow response to voltage at beginning, linear response in the middle and reverse response at the end forming an 'S' shape is defined as diode like. The current tends to saturate at high voltage in both cases. Decreasing resistance between measurements indicates the previous measurements influence the carrier concentration. This indicates annealing from an increase in device temperature caused by heat generated by the current through the device. This corresponds to a previous report [3]. Figure 4.28(a) shows the performance of a resistor type and Figure 4.28 (b) shows a typical diode type performance.

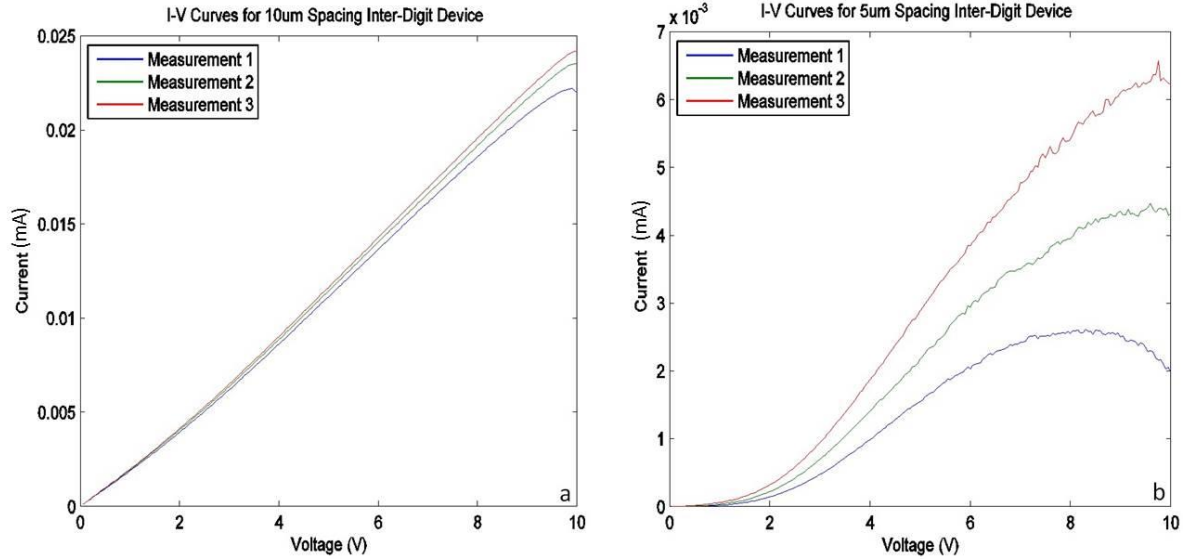


Figure 4.28 I-V curve of sensor prototype (a) a resistor type behavior (b) diode type behavior

Resistance was calculated for each measurement for both resistor type and diode type (using the linear region in 3V to 5V for calculation). The resistance of the resistor type device was calculated by performing a linear regression of the voltage on current and the slope was taken as resistance. The resistance of the diode type device was calculated by the same method but only in the linear region of the I-V curve (region of 3V to 5V was used for all diode type devices here).

The resistance of the same type sensor (in the same row) changes significantly by an order of magnitude, which indicates non-uniform fabrication of the device. This non-uniformity can be caused by photoresist pattern from the laser lithography's non-uniform intensity distribution, the ZnO film from the PLD process and gold contacts from E-beam deposition. The laser lithography process is more critical in this case for the reason that the

light beam wasn't expanded enough to have a uniform distribution of intensity on the sample where instead a Gaussian profile of intensity distribution was formed on both sample holder and the mirror. When the center of the beam was adjusted in the middle of the sample holder and the mirror, the exposure area has an intensity distribution decreasing from the middle of the beam. Such a power distribution leads to a dose distribution in the same direction, which is likely to cause a uniformity problem. An expanded beam can be used to improve the uniformity of intensity distribution.

It was found that all devices performed same change trend (an increase in current with same voltage during three measurements) regardless of the device performance type, resistor or diode. The changes of the resistance in the three measurements were examined for single digit devices and multiple interdigitated devices as Eq. 4.4.

$$\%change = \frac{\Delta R}{R_1} \times 100\% \quad (4.4)$$

The results are shown in Figure 4.29.

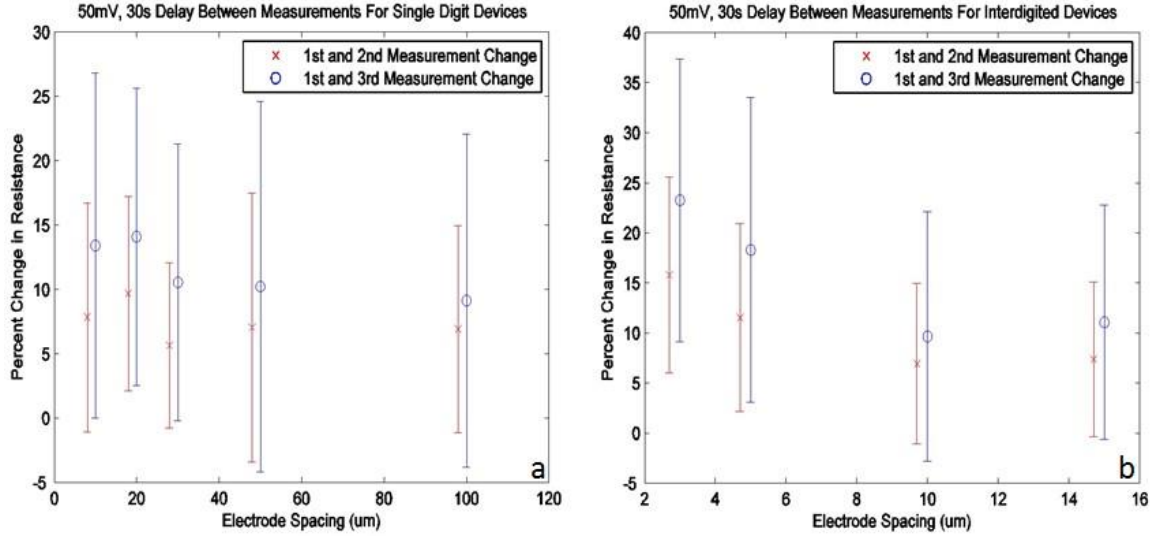


Figure 4.29 Resistance change between measurements

The large error corresponds to the non-uniformity of resistance with the same sensor structures. A clear increase in  $\Delta R$  is seen which again indicates a change in the carrier concentration due to self-annealing.

#### 4.6.3 Current density of the textured ZnO thin films

The resistance of the same type of sensor differs but mostly stays in the same order of magnitude. The differences in the resistance are caused by non-uniformity of the film and especially of the etched depth of the texture (wires). The non-uniform distribution of the laser beam power leads to a distribution of laser beam intensity on the sample which results in a non-uniform exposed thickness. This can be addressed by either making the beam more uniform or exposed through the photoresist layer.

Since the resistance of the same type of sensor differs within an order of magnitude. The current density is calculated using 20μA at 8V for 10μm spacing multiple interdigitated device. The ZnO film was 160nm thick with 40nm deep texture. The digit is 200μm long and 10μm apart from the other contact. The area between two digits is  $V = 180\mu\text{m} * 160\text{nm} - \frac{180\mu\text{m} * 40\text{nm}}{2} = 25.2\mu\text{m}^2$ . For 10μm spacing multiple interdigitated device, there are 10 digits in total. The current density can be estimated as  $J = \frac{20\mu\text{A}}{10 * 25.2\mu\text{m}^2} = 7.936\text{A}/\text{cm}^2$ .

The increased surface area ratio can be calculated as the ratio between increased surface area over the surface area of plain thin film. For textured films with period p and texture depth h, the increased surface area ratio can be calculated as:

$$\Delta S\% = \frac{h}{p} \quad (4.5)$$

For wires (the film is etched through in this case) with period p and depth h, the increased surface area ratio can be calculated as:

$$\Delta S\% = \frac{2h}{p} \quad (4.6)$$

For a textured film with period 2μm and texture depth 40nm, the increased surface area ratio is 2%. The ratio can be further increased if the period is smaller and the depth is larger. For example, the ratio can be increased to 10% with a 500nm period and 50nm depth, 20% with

250nm period and 50nm depth. For the purpose of the first fabrication, the ratio was not intended to be large.

#### **4.6.4 Qualitative gas sensing performance**

Gas sensing measurement was conducted in three conditions:

- a) Atmosphere pressure at room temperature illuminated with UV LED without heater
- b) Under vacuum at elevated temperature with heater only
- c) Under vacuum at room temperature illuminated with UV LED without heater

Figure 4.30 shows a photograph of the external heater [4]. The heater was placed underneath the sensor during testing.



Figure 4.30 photograph of external heater

### A. Sensor performance under condition a

No clear response to ozone was observed under condition a. It is not suitable to make conclusion that the sensor is not able to operate under condition (a) for the weakness in the testing setup since the sensor showed response under condition (b) and (c). A more accurate ozone generator and better testing chamber able to control constant flow inside are needed.

### B. Sensor performance under condition b

The result of sensor performance under vacuum at elevated temperature with heater only is shown in Fig .4.31.

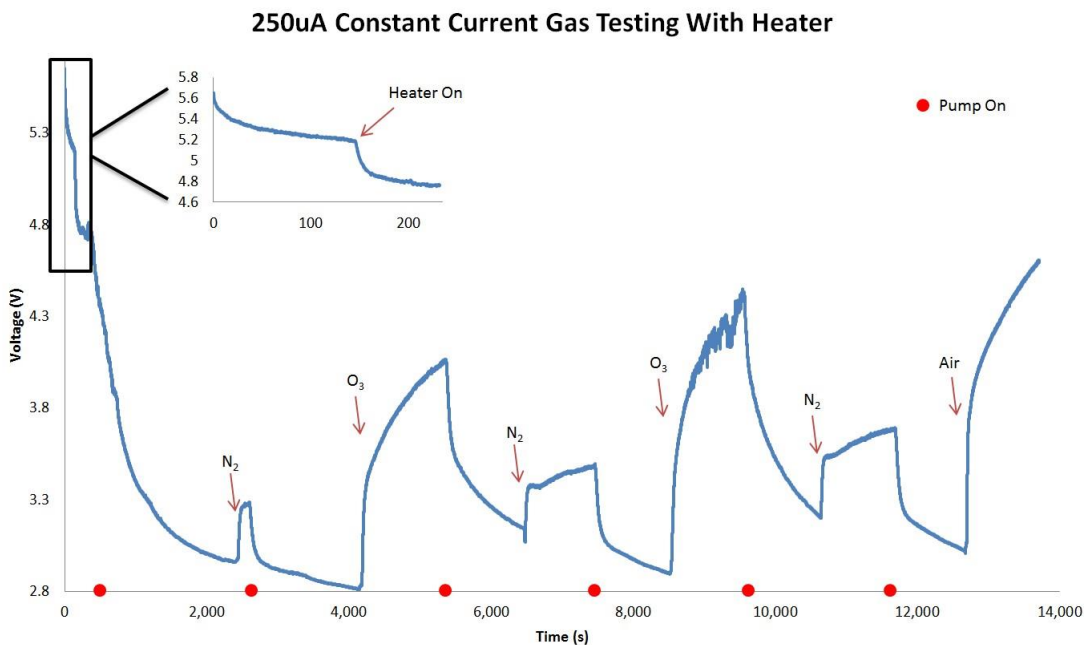


Figure 4.31 Gas sensing performance with heater under vacuum. Red dots indicate when the pump was turned on.

A constant 250 $\mu$ A current was kept through the single digit contact type sensor during the test. A drop in voltage happens when the test starts, which indicates an increase in the carrier concentration. The change in carrier concentration is likely caused by an increase in the sensor temperature caused by Joule self-heating effect. As seen in the magnified window in Figure 4.31, a similar carrier concentration change is also introduced by increasing the temperature with the heater.

To examine the sensitivity of those devices, given the equipment limitations in the lab the following experiment was performed.

- a) Bell jar evacuated to 50 mTorr
- b) Nitrogen gas introduced until pressure increased to 3 Torr
- c) Bell jar evacuated to 50 mTorr
- d) Ozone / Air introduced

Then the cycle was repeated.

While this experimental setup can be improved it does show responsiveness of the sensor to external conditions that can be broken into two main components,

- 1) Change in thermal conductivity of the surrounding gas on the nanowire, which changes the carrier concentration and resistance of the wire
- 2) Change in adsorption of the gases due to reaction with the wire

As can be seen from the data the  $N_2$  signal saturates quickly. And since it's not reactive with ZnO wire the shape may be attributed to the change in thermal conductivity, assuming that removal of atoms from the surface is relatively small. This in turn changes the sensor temperature and performance.

For the ozone / Air case one sees that the sensor does not completely saturate, in the same manner. Typical gas sensor performance was observed with an ozone environment, which was different from the response to a nitrogen environment. The response is a combination of surface reaction with target gas and temperature change due to the change in thermal conductivity of surrounding environment. Thermal conductivity of specific ozone concentration needs to be measured to compare with nitrogen gas for further investigation. Only thermal conductivity of liquid ozone was found in literature [5]. Since the concentration of ozone in the ozone/air mixture is low so that the thermal conductivity of air can be used as an approximation. The thermal conductivity of air [6] is  $0.0257W/mK$  at  $20\text{ }^{\circ}C$  which is close to the thermal conductivity of nitrogen [7] at  $20\text{ }^{\circ}C$  of  $0.0234W/mK$ . The response to ozone / air mixtures is much higher than the difference in thermal conductivity which indicates surface reaction with gases contributes to the increase of resistance.

### **C. Sensor performance under condition c**

A single digit contact type sensor was measured in vacuum and illuminated by UV LED without a heater for gas sensing performance as shown in Figure 4.32.

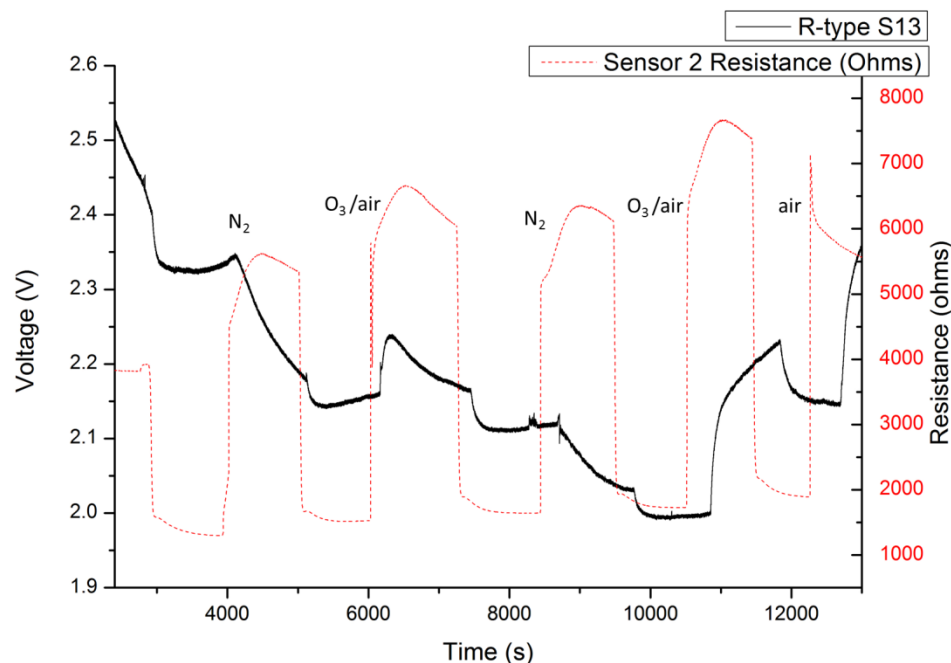


Figure 4.32 Gas sensing performance with UV LED under vacuum with no heater

The red dotted line in Figure 4.32 represents the measurement of a commercial sensor whereas the black line represents the sensor prototype performance and the red dotted line represents the commercial sensor response. Unlike in the heated situation, the sensor prototype responded to the nitrogen environment with a further decrease in voltage whereas the commercial sensor has an increase in resistance similar to its response to ozone. The sensor prototype's responses to ozone have a similar shape in both situations (a logarithmic increase and an exponential decrease). Further investigation is needed for understanding the sensor's performance, which requires a more accurately controlled ozone generator, testing chamber and calibration of the commercial gas sensor.

## REFERENCES

- [1] A. Suresh, "Amorphous Indium Gallium Zinc Oxide Thin-Film Transistors, Non-volatile Memory and Circuits for Transparent Electronics," 2010.
- [2] N. Patil, "Photoelectrocatalytic Sensor for Volatile Organic Compounds using Indium Gallium Zinc Oxide Thin Film Transistor," 2010.
- [3] E. Strelcov, S. Dmitriev, B. Button, J. Cothren, V. Sysoev, and A. Kolmakov, "Evidence of the self-heating effect on surface reactivity and gas sensing of metal oxide nanowire chemiresistors," *Nanotechnology*, vol. 19, p. 355502, 2008.
- [4] The heater was from Dr. Veena Misra's Group
- [5] T. Waterman, D. Kirsh, and R. Brabets, "Thermal Conductivity of Liquid Ozone," *The Journal of Chemical Physics*, vol. 32, pp. 304-305, 1960.
- [6] *hyperphysics*. Available: <http://hyperphysics.phy-astr.gsu.edu/hbase/tables/thrcn.html>
- [7] *Engineering Tool Box*. Available: [http://www.engineeringtoolbox.com/air-properties-d\\_156.html](http://www.engineeringtoolbox.com/air-properties-d_156.html)

## **Chapter 5 Conclusion**

### **5.1 Conclusions**

Thin film gas sensors based on semiconducting metal oxides have been investigated extensively in recent years for their compact size, ability for integration, low cost and variety of gases that can be detected. Metal oxide gas sensors have been continuously researched to reduce power consumption and to have better sensitivity and reliability. Room temperature gas sensing is one of the challenges metal oxide gas sensors face since the semiconductor material requires elevated temperatures for the activation of a reversible chemical reaction with the target gas. An external heater is usually required for metal oxide gas sensors to operate, which increases the cost and power consumption.

The self-heating effect brought by nanowires is one of the promising approaches for room temperature sensing. The increased Joule heating effect brought by the decrease of the nanowire dimension gives the sensor the capability of self-heating during operation.

The photo-electrocatalytic effect by UV illumination is another promising approach for room temperature gas sensing. Based on the quick reaction time of the photoinduced free electrons, people have used UV light for sensor's recovery in room temperature gas sensing and brought the response limit down to 10 ppb.

Laser interference lithography offers a quick, mask free, large area, low cost fabrication of periodic structures. By using a 355nm UV laser, periods as small as 250nm

have been achieved. Large periods such as 2  $\mu\text{m}$  can be achieved by the same method by the tuning angles of the setup. Such a fabrication method offers the opportunity of controlling nanowire size, which can obtain the self-heating effect as discussed. By choosing a suitable sensing material, the photo-electrocatalytic effect can be introduced into the same sensor.

A sensor prototype with 2 $\mu\text{m}$  period has been made and tested. Room temperature gas sensing capability has been proved by the photo-electrocatalytic effect under vacuum.

## **5.2 Suggestions for Future Work**

Numerous improvement of the fabrication method is still needed, such as improving the aspect ratio of small period laser interference lithography results. Another approach is to use wet etching instead of pure RIE for pattern transfer from the photoresist to the desired layer.

Anti-reflection coating is widely used in laser interference lithography processes to obtain a better aspect ratio, which in the fabrication of metal oxide gas sensors may not be necessary for the reason that the metal oxide layer can be used as effective thin film interference type anti-reflection coating by itself. Precise control of metal oxide deposition is needed in this case. Calculation and simulation methods discussed in Chapter 3 in this thesis may provide useful information of structure design to take such an advantage.

Some vapor etch tests have been done by the author to test the validity of such etching processes. These results were not put into the thesis for the consistency of content.

The sample was put on the top of an upside-down plastic basket inside a beaker with the etchant liquid inside the beaker. The etchant liquid was kept below the sample to avoid contact. The beaker was then set on an external heater at 70 °C with an upside-down Petri dish on top used as a cap to create equilibrium environment. The warming up process was kept for more than 20 minutes before putting samples in. This step was to guarantee the gas equilibrium.

An HF vapor etched glass substrate is shown in Figure 5.1 (a). The test results prove the validity of vapor etching using HF as an etchant. Repeatability of the etching speed is an issue due to the lack of accurate control of the experiment setup. Vapor etch tests with HCl on ZnO thin films were conducted for a validity test. Figure 5.1 (b), (c) and (d) show microscopic images of HCl vapor etched ZnO. Many water drops formed when conducting HCl vapor etching indicating the need for a wet etch instead. The uniformity of vapor etching is a problem that the edge etches faster than the middle, which can be seen in Figure 5.1 (c). Pattern transfer wise, it is acceptable as seen in Figure 5.1 (d). For future investigation, a wet etch using a well diluted HCl solution may provide better results.

Suspended photoresist nanowires can be achieved by multiple exposures with careful control of exposure times. Since air has lower thermal conductivity than silicon nitride, such an easy procedure is promising for next generation devices.

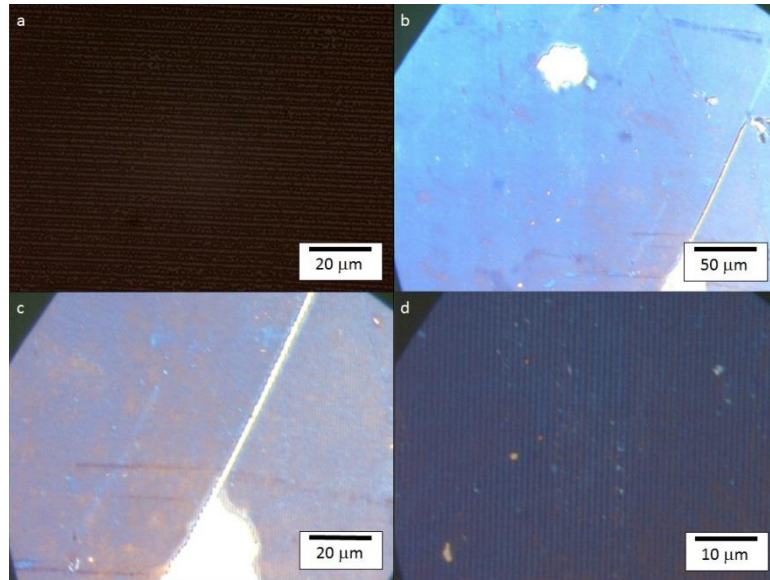


Figure 5.1 Vapor etching test results (a) HF vapor etch on glass substrate (b) (c) (d) HCl vapor etching on ZnO thin film

## APPENDICES

## Appendix A

Refractive Index list for Materials at 355nm wavelength

Material	n	k
Zinc Oxide [1]	2.47464	0.4308
Amorphous Silicon [2]	4.64682	
Single Crystalline Silicon [3]	5.610	3.014
High Temperature Glass [2]	1.5646	
Photoresist (AZ5214E) [4]	1.6990	0.0175
Anti-Reflection Coating (WIDE 15B) [5]	1.72	0.33
Gold [6]	1.73817	1.8491

- [1] J. Muth, R. Kolbas, A. Sharma, S. Oktyabrsky, and J. Narayan, "Excitonic structure and absorption coefficient measurements of ZnO single crystal epitaxial films deposited by pulsed laser deposition," *Journal of Applied Physics*, vol. 85, pp. 7884-7887, 1999.
- [2] Refractive index database [Online]. Available: <http://refractiveindex.info/>
- [3] D. Aspnes and A. Studna, "Dielectric functions and optical parameters of Si, Ge, GaP, GaAs, GaSb, InP, InAs, and InSb from 1.5 to 6.0 ev," *Physical Review B*, vol. 27, p. 985, 1983.

- [4] (2010). *Optical Parameters of Photoresists*. Available:  
[http://www.microchemicals.eu/technical\\_information/photoresists\\_optical\\_parameters.pdf](http://www.microchemicals.eu/technical_information/photoresists_optical_parameters.pdf)
- [5] Provided by Brewer Science, Inc.
- [6] E. D. Palik, *Handbook of Optical Constants of Solids: Index* vol. 3: Access Online via Elsevier, 1998.

## Appendix B

```
##Xiang Ji, xji3@ncsu.edu
##MSE Dept. NCSU
##Feb. 6th, 2013
##This Python Code is written for the check of phase shift in our gas sensor project

from math import sqrt, exp, cos, sin, pi, atan2
from numpy import *
import matplotlib.pyplot as plt
import copy

# effective refractive index
# Method 1 according to Bernings
# Handbook of Optics, 3rd Edition, Vol. 1, p390, 12.11

def alfa(n0,n1,k1,theta0):
    res=1.0+(n0*sin(theta0)/(n1**2+k1**2))**2*(k1**2-n1**2)
    return res

def beta(n0,n1,k1,theta0):
    res=-2*n1*k1*(n0*sin(theta0)/(n1**2+k1**2))**2
    return res

def cos_theta(n0,n1,k1,theta0):
    a1=alfa(n0,n1,k1,theta0)
    b1=beta(n0,n1,k1,theta0)
    res=sqrt((sqrt(a1**2+b1**2)+a1)/2)-1.0*sqrt((sqrt(a1**2+b1**2)-a1)/2)
    return res

def eta_1s(n0,n1,k1,theta0):
    costheta1=cos_theta(n0,n1,k1,theta0)
    res=(n1-1.0*k1)*costheta1
    return res

def eta_1p(n0,n1,k1,theta0):
```

```

costheta1=cos_theta(n0,n1,k1,theta0)
res=(n1-1.0j*k1)/costheta1
return res

# effective refractive index
# Method 2 according to Abeles method
# Handbook of Optics, 3rd Edition, Vol. 1, p390, 12.11

def ab(n0,n1,k1,theta0):
    s=(n1**2-k1**2-n0**2*sin(theta0)**2)
    a=sqrt((s+sqrt(s**2+4*n1**2*k1**2))/2)
    b=n1*k1/a
    return a,b

def cd(n0,n1,k1,theta0):
    a,b = ab(n0,n1,k1,theta0)
    c=a*(1+n0**2*sin(theta0)**2/(a**2+b**2))
    d=b*(1-n0**2*sin(theta0)**2/(a**2+b**2))
    return c,d

def eta_1s_Abeles(n0,n1,k1,theta0):
    a,b = ab(n0,n1,k1,theta0)
    return a-1.0j*b

def eta_1p_Abeles(n0,n1,k1,theta0):
    c,d = cd(n0,n1,k1,theta0)
    return c-1.0j*d

def rs_rp(n0,n1,k1,theta0,method=1):
    if method==1:
        eta1s=eta_1s(n0,n1,k1,theta0)
        eta1p=eta_1p(n0,n1,k1,theta0)
    elif method==2:
        eta1s=eta_1s_Abeles(n0,n1,k1,theta0)
        eta1p=eta_1p_Abeles(n0,n1,k1,theta0)
    else:
        print 'Please choose a method for effective index calculation'

```

```

    print
    eta1s=1.0
    eta1p=1.0

    eta_0s=n0*cos(theta0)
    eta_0p=n0/cos(theta0)

    rs= (eta_0s-eta1s)/(eta_0s+eta1s)
    rp= (eta1p-eta_0p)/(eta1p+eta_0p)

    return rs,rp

def Get_rs_rp(n0, inc_angle,material,method=1):
    if material == 'gold':
        n1=1.73817 # Au @ 355nm
        k1=1.8491 # Au @ 355nm
    elif material == 'Poly-Si':
        n1=5.55336 # Poly-Si @ 355nm
        k1=2.5515 # Poly-Si @ 355nm
    elif material == 'SC-Si':
        n1=5.610 # SC-Si @ 355nm
        k1=3.014 # SC-Si @ 355nm
    elif material == 'ZnO':
        n1=2.47464 # ZnO @ 355nm
        k1=0.4308 # ZnO @ 355nm
    elif material == 'Glass':
        n1=1.5646 # HT Glass @ 355nm
        k1=0.0 # HT Glass @ 355nm
    else:
        print 'Please choose your material properly'

    rs_list=[]
    rp_list=[]

    Rs__list=[]
    Rp__list=[]

```

```

rs_phase_list=[]
rp_phase_list=[]

rs_list_real=[]
rs_list_imag=[]

rp_list_real=[]
rp_list_imag=[]

for a in range(0,len(inc_angle)):
    rs,rp = rs_rp(n0,n1,k1,inc_angle[a],method)
    rs_list.append(rs)
    rp_list.append(rp)

return rs_list, rp_list

def Get_Rs_Rp_phase(rs_list,rp_list):
    Rs__list=[]
    Rp__list=[]
    rs_phase_list=[]
    rp_phase_list=[]
    for a in range(0,len(rs_list)):
        Rs__list.append(abs(rs_list[a])**2)
        Rp__list.append(abs(rp_list[a])**2)
        rs_phase_list.append(atan2(rs_list[a].imag,rs_list[a].real)/pi*180)
        rp_phase_list.append(atan2(rp_list[a].imag,rp_list[a].real)/pi*180)
    return Rs__list, Rp__list, rs_phase_list, rp_phase_list

def Get_pics(material1, material2, material3,polarization='s'):
    rs_list_1, rp_list_1 = Get_rs_rp(n0, inc_angle,material1)
    Rs__list_1,          Rp__list_1,          rs_phase_list_1,          rp_phase_list_1          =
    Get_Rs_Rp_phase(rs_list_1,rp_list_1)

    rs_list_2, rp_list_2 = Get_rs_rp(n0, inc_angle,material2)
    Rs__list_2,          Rp__list_2,          rs_phase_list_2,          rp_phase_list_2          =
    Get_Rs_Rp_phase(rs_list_2,rp_list_2)

```

```

rs_list_3, rp_list_3 = Get_rs_rp(n0, inc_angle, material3)
Rs__list_3, Rp__list_3, rs_phase_list_3, rp_phase_list_3 =
Get_Rs_Rp_phase(rs_list_3, rp_list_3)

if polarization == 's':
    c=plt.plot(inc_angle,rs_phase_list_1,inc_angle,rs_phase_list_2,inc_angle,rs_phase_list_3)
    plt.xlabel('Incident Angle')
    plt.ylabel('s-polarized Relection Phase')
    plt.legend([material1,material2,material3],'lower right')
    plt.suptitle(material1+' '+material2+' '+material3+' s polarized Reflection Phase
Comparison', fontsize=12)
    plt.savefig((material1+' '+material2+' '+material3+' s polarized Reflection Phase
Comparison.png'),transparent=True)
    plt.close()

    c=plt.plot(inc_angle,Rs__list_1,inc_angle,Rs__list_2,inc_angle,Rs__list_3)
    plt.xlabel('Incident Angle')
    plt.ylabel('s-polarized Relection Coeff')
    plt.legend([material1,material2,material3],'lower right')
    plt.suptitle(material1+' '+material2+' '+material3+' s polarized Reflection Coeff
Comparison', fontsize=12)
    plt.savefig((material1+' '+material2+' '+material3+' s polarized Reflection Coeff
Comparison.png'),transparent=True)
    plt.close()
    return 0
elif polarization == 'p':
    c=plt.plot(inc_angle,rp_phase_list_1,inc_angle,rp_phase_list_2,inc_angle,rp_phase_list_3)
    plt.xlabel('Incident Angle')
    plt.ylabel('p-polarized Relection Phase')
    plt.legend([material1,material2,material3],'lower right')
    plt.suptitle(material1+' '+material2+' '+material3+' p polarized Reflection Phase
Comparison', fontsize=12)
    plt.savefig((material1+' '+material2+' '+material3+' p polarized Reflection Phase
Comparison.png'),transparent=True)
    plt.close()

```

```

c=plt.plot(inc_angle,Rp__list_1,inc_angle,Rp__list_2,inc_angle,Rp__list_3)
plt.xlabel('Incident Angle')
plt.ylabel('p-polarized Relection Coeff')
plt.legend([material1,material2,material3],'lower right')
plt.suptitle(material1+' '+material2+' '+material3+' p polarized Reflection Coeff
Comparison', fontsize=12)
plt.savefig((material1+' '+material2+' '+material3+' p polarized Reflection Coeff
Comparison.png'),transparent=True)
plt.close()
return 1
n0=1.0
inc_angle=arange(0.0,90.0/180.0*pi,0.1/180.0*pi)
material1='gold'
material2='SC-Si'
material3='Glass'
polarization='s'
Get_pics(material1, material2, material3,polarization)

```

## Appendix C

```
%FieldDistribution.m
%Xiang Ji
%xji3@ncsu.edu
%Code written for thin film reflectance calculation
%All rights reserved 2013

clear;clc;
n_ZnO=2.47464; % @ 355nm
n_Si=4.64682; % amorphous silicon @ 355nm
n_Si_poly=5.55336-2.5515i; % polycrystal silicon @ 355nm
n_Pr=1.7123-0.0358i; % AZ5214E @ 365nm unbleached
n_Glass=1.5513; % HT Glass @ 355nm
n_ARC=1.72-0.33i; % WIDE-15B ARC from Brewer Science

n_list=[1.0,n_Pr,n_ZnO,n_S]; %start with n_list(1) = 1.0 as outside layer,
air here
ZnO_Thickness_list=35;

z_FD=(0.0:-1:-350.0)*1e-9;
x_FD=(-500.0:2.0:500.0)*1e-9;

incident_list=[45,-45];
R_list=ones(length(z_FD),length(incident_list)); % store reflection
coefficient for each angle

polarization='p'; % define polarization: p/s
% polarization='s'; % define polarization: p/s

lamda=355.0e-9; % unit in m

y_optical_admittance=2.654419E-3; % unit in SI

k=length(n_list)-1;
% q=(k+1)*ones(length(theta_incident)); %used to locate where internal
'total' reflection happens
l_list=[0.0,300.0,ZnO_Thickness_list,15.0]*1e-9; % unit in m
substrate = sum(l_list)-l_list(length(l_list));

Ex_matrix=ones(length(x_FD),length(z_FD),length(incident_list));
Ey_matrix=ones(length(x_FD),length(z_FD),length(incident_list));
Ez_matrix=ones(length(x_FD),length(z_FD),length(incident_list));
E2_matrix=ones(length(x_FD),length(z_FD));

for x_counter=1:1:length(x_FD)
    x=x_FD(x_counter);
    for z_counter=1:1:length(z_FD)
        z=z_FD(z_counter);
```

```

        for angle_counter=1:1:length(incident_list)
            theta_incident=incident_list(angle_counter)/180.0*pi;
            theta_list=[theta_incident]; % used to store angles in each
layer
            for it = 1:k
                if n_list(it)*sin(theta_list(it))>n_list(it+1)
                    q=it; %need to change
                else
                    theta =
asin(n_list(1)*sin(theta_list(1))/n_list(it+1));
                    % theta =
asin(real(n_list(1))*sin(theta_list(1))/real(n_list(it+1)));
                    theta_list=[theta_list,theta];
                end
            end

[E,n,angle,R]=MatrixCalFD(z,n_list,l_list,theta_list,lamda,y_optical_admit
tance,polarization);
            R_list(z_counter,angle_counter)=R;

[Ex,Ey,Ez]=FD(x,z,E(1),E(2),n,angle,polarization,lamda,substrate);
            Ex_matrix(x_counter,z_counter,angle_counter)=Ex;
            Ey_matrix(x_counter,z_counter,angle_counter)=Ey;
            Ez_matrix(x_counter,z_counter,angle_counter)=Ez;
        end
    end
end

E2_matrix=abs(Ey_matrix(:, :, 1)+Ey_matrix(:, :, 2)).^2+abs(Ex_matrix(:, :, 1)+E
x_matrix(:, :, 2)).^2+abs(Ez_matrix(:, :, 1)+Ez_matrix(:, :, 2)).^2;

substrate='Glass';

h=figure(1);
imagesc(x_FD,z_FD,E2_matrix');
axis xy;
colorbar;
xlabel('x (m)');
ylabel('y (m)');
title('E^{2}');
save(strcat('FD_45_135_',polarization,'_300Pr_35nmZnO_',substrate),'E2_mat
rix');
saveas(h,strcat('FD_45_135_',polarization,'_300Pr_35nmZnO_',substrate,'.jp
g'));

h=figure(2);
imagesc(x_FD,z_FD,(abs(Ex_matrix(:, :, 1)+Ex_matrix(:, :, 2)))');
axis xy;
colorbar;
xlabel('x (m)');
ylabel('y (m)');
title('E_{x}');

```

```

save(strcat('Ex_FD_45_135_',polarization,'_300Pr_35nmZnO_',substrate),'E2_
matrix');
saveas(h,strcat('Ex_FD_45_135_',polarization,'_300Pr_35nmZnO_',substrate,'
.jpg'));

h=figure(3);
imagesc(x_FD,z_FD,(abs(Ey_matrix(:, :,1)+Ey_matrix(:, :,2))));
axis xy;
colorbar;
xlabel('x (m)');
ylabel('y (m)');
title('E_{z}');
save(strcat('Ey_FD_45_135_',polarization,'_300Pr_35nmZnO_',substrate),'E2_
matrix');
saveas(h,strcat('Ey_FD_45_135_',polarization,'_300Pr_35nmZnO_',substrate,'
.jpg'));

h=figure(4);
imagesc(x_FD,z_FD,(abs(Ez_matrix(:, :,1)+Ez_matrix(:, :,2))));
axis xy;
colorbar;
xlabel('x (m)');
ylabel('y (m)');
title('E_{y}');
save(strcat('Ez_FD_45_135_',polarization,'_300Pr_35nmZnO_',substrate),'E2_
matrix');
saveas(h,strcat('Ez_FD_45_135_',polarization,'_300Pr_35nmZnO_',substrate,'
.jpg'));

% FD.m
function
[Ex,Ey,Ez]=FD(x,z,E_plus,E_minus,n,angle,polarization,lamda,substrate)
% Give out Electric field component for field distribution calculation
if (polarization=='s')
    Ex=0.0;
    Ez=0.0;

    if (z<-substrate)

Ey=E_plus*exp(1j*(2*pi*n/lamda)*(x*sin(angle)+(z+substrate)*cos(angle)));
%z direction here is opposite

    else

        Ey=E_plus*exp(1j*(2*pi*n/lamda)*(x*sin(angle)))...
        +E_minus*exp(1j*(2*pi*n/lamda)*(x*sin(angle))); %z direction
here is opposite

    end
end

```

```

else
    Ey=0.0;

    if (z<-substrate)

Ez=E_plus*exp(1j*(2*pi*n/lamda)*(x*sin(angle)+(z+substrate)*cos(angle)))*(
tan(angle)); %z direction here is opposite *tan(angle)

Ex=E_plus*exp(1j*(2*pi*n/lamda)*(x*sin(angle)+(z+substrate)*cos(angle)));
%z direction here is opposite *sign(sin(angle))
    else
        Ez=(E_plus*exp(1j*(2*pi*n/lamda)*(x*sin(angle)))...
-
E_minus*exp(1j*(2*pi*n/lamda)*(x*sin(angle))))*(tan(angle)); %z direction
here is opposite +z*cos(angle) -z*cos(angle)

Ex=E_plus*exp(1j*(2*pi*n/lamda)*(x*sin(angle)))... %*sign(sin(angle))*sign
(sin(angle))
        +E_minus*exp(1j*(2*pi*n/lamda)*(x*sin(angle))); %z
direction here is opposite +z*cos(angle) -z*cos(angle)
    end

end
end

```

```

%For_Error.m

clear;
clc;

%%%%%%%%%%%%%%%%%%%%%%%%%%%%%%%%%%%%%%%%%%%%%%%%%%%%%%%%%%%%%%%%%%%%%%%%
%%%%%%%%%%%%%%%%%%%%%%%%%%%%%%%%%%%%%%%%%%%%%%%%%%%%%%%%%%%%%%%%%%%%%%%%
% start normalizing data from FDTD
%%%%%%%%%%%%%%%%%%%%%%%%%%%%%%%%%%%%%%%%%%%%%%%%%%%%%%%%%%%%%%%%%%%%%%%%
%%%%%%%%%%%%%%%%%%%%%%%%%%%%%%%%%%%%%%%%%%%%%%%%%%%%%%%%%%%%%%%%%%%%%%%%

a=45;
b=135;

load(strcat('E2_',num2str(a),'_',num2str(b),'_p.mat'));
Ex_p_FDTD=Ex;
Ey_p_FDTD=Ey;
Ez_p_FDTD=Ez;
E2_p_FDTD=abs(Ex_p_FDTD.^2)+abs(Ey_p_FDTD.^2)+abs(Ez_p_FDTD.^2);
scale_p_FDTD=sqrt(max(max(E2_p_FDTD))); %scale is used for normalizing
amplitude

load(strcat('E2_',num2str(a),'_',num2str(b),'_s.mat'));
Ex_s_FDTD=Ex;
Ey_s_FDTD=Ey;
Ez_s_FDTD=Ez;
E2_s_FDTD=abs(Ex_s_FDTD.^2)+abs(Ey_s_FDTD.^2)+abs(Ez_s_FDTD.^2);
scale_s_FDTD=sqrt(max(max(E2_s_FDTD))); %scale is used for normalizing
amplitude

%%%%%%%%%%%%%%%%%%%%%%%%%%%%%%%%%%%%%%%%%%%%%%%%%%%%%%%%%%%%%%%%%%%%%%%%
%%%%%%%%%%%%%%%%%%%%%%%%%%%%%%%%%%%%%%%%%%%%%%%%%%%%%%%%%%%%%%%%%%%%%%%%
% start normalizing data from theoretical calculation
%%%%%%%%%%%%%%%%%%%%%%%%%%%%%%%%%%%%%%%%%%%%%%%%%%%%%%%%%%%%%%%%%%%%%%%%
%%%%%%%%%%%%%%%%%%%%%%%%%%%%%%%%%%%%%%%%%%%%%%%%%%%%%%%%%%%%%%%%%%%%%%%%

a=45;
b=135;
z_FD=(-1.0:-1:-350.0)*1e-9;
x_FD=(-500.0:1.0:500.0)*1e-9;

substrate='Silicon';
polarization='p';
load(strcat('FD_',num2str(a),'_',num2str(b),'_',polarization,'_300Pr_35nmZnO_',substrate),'E2_matrix');
load(strcat('Ex_FD_',num2str(a),'_',num2str(b),'_',polarization,'_300Pr_35nmZnO_',substrate),'Ex_matrix');
load(strcat('Ey_FD_',num2str(a),'_',num2str(b),'_',polarization,'_300Pr_35nmZnO_',substrate),'Ey_matrix');
load(strcat('Ez_FD_',num2str(a),'_',num2str(b),'_',polarization,'_300Pr_35nmZnO_',substrate),'Ez_matrix');

```

```

Ex_matrix=Ex_matrix(:, :, 1)+Ex_matrix(:, :, 2);
Ey_matrix=Ey_matrix(:, :, 1)+Ey_matrix(:, :, 2);
Ez_matrix=Ez_matrix(:, :, 1)+Ez_matrix(:, :, 2);
Ex_p_calculation=Ex_matrix;
Ey_p_calculation=Ez_matrix;
Ez_p_calculation=Ey_matrix; %/max(max(abs(Ey_matrix)))
E2_p_calculation=abs(Ex_p_calculation).^2+abs(Ey_p_calculation).^2+abs(Ez_p_calculation).^2;
scale_p_calculation=sqrt(max(max(E2_p_calculation))); %scale is used for
normalizing amplitude

polarization='s';
load(strcat('FD_', num2str(a), '_', num2str(b), '_', polarization, '_300Pr_35nmZnO_', substrate), 'E2_matrix');
load(strcat('Ex_FD_', num2str(a), '_', num2str(b), '_', polarization, '_300Pr_35nmZnO_', substrate), 'Ex_matrix');
load(strcat('Ey_FD_', num2str(a), '_', num2str(b), '_', polarization, '_300Pr_35nmZnO_', substrate), 'Ey_matrix');
load(strcat('Ez_FD_', num2str(a), '_', num2str(b), '_', polarization, '_300Pr_35nmZnO_', substrate), 'Ez_matrix');
Ex_matrix=Ex_matrix(:, :, 1)+Ex_matrix(:, :, 2);
Ey_matrix=Ey_matrix(:, :, 1)+Ey_matrix(:, :, 2);
Ez_matrix=Ez_matrix(:, :, 1)+Ez_matrix(:, :, 2);
Ex_s_calculation=Ex_matrix;
Ey_s_calculation=Ez_matrix;
Ez_s_calculation=Ey_matrix;
E2_s_calculation=abs(Ex_s_calculation).^2+abs(Ey_s_calculation).^2+abs(Ez_s_calculation).^2;
scale_s_calculation=sqrt(max(max(E2_s_calculation))); %scale is used for
normalizing amplitude

polarization='s';
h=figure(1);
imagesc(x_FD, z_FD, E2_s_calculation/(scale_s_calculation^2)-E2_s_FDTD/(scale_s_FDTD^2));
axis xy;
colorbar;
xlabel('x (m)');
ylabel('y (m)');
title(strcat('\Delta E^{2}'));
saveas(h, strcat('FD_ERR_', num2str(a), '_', num2str(b), '_', polarization, '_300Pr_35nmZnO_', substrate, '.jpg'));

polarization='p';

h=figure(2);
imagesc(x_FD, z_FD, E2_p_calculation/(scale_p_calculation^2)-E2_p_FDTD/(scale_p_FDTD^2));
axis xy;
colorbar;
xlabel('x (m)');
ylabel('y (m)');

```

```

title(strcat('\Delta E^{2}'));
saveas(h,strcat('FD_ERR_',num2str(a),'_',num2str(b),'_',polarization,'_300
Pr_35nmZnO_',substrate,'.jpg'));

h=figure(3);
imagesc(x_FD,z_FD,abs(Ex_p_calculation/(scale_p_calculation))-
abs(Ex_p_FDTD/(scale_p_FDTD)));
axis xy;
colorbar;
xlabel('x (m)');
ylabel('y (m)');
title(strcat('\Delta |E_{x}|'));
saveas(h,strcat('Ex_FD_ERR_',num2str(a),'_',num2str(b),'_',polarization,'_
300Pr_35nmZnO_',substrate,'.jpg'));

h=figure(4);
imagesc(x_FD,z_FD,abs(Ey_p_calculation/(scale_p_calculation))-
abs(Ey_p_FDTD/(scale_p_FDTD)));
axis xy;
colorbar;
xlabel('x (m)');
ylabel('y (m)');
title(strcat('\Delta |E_{y}|'));
saveas(h,strcat('Ey_FD_ERR_',num2str(a),'_',num2str(b),'_',polarization,'_
300Pr_35nmZnO_',substrate,'.jpg'));

% h=figure(5);
% imagesc(x_FD,z_FD,abs(Ez_p_calculation/(scale_p_calculation))-
% abs(Ez_p_FDTD/(scale_p_FDTD)));
% axis xy;
% colorbar;
% xlabel('x (m)');
% ylabel('y (m)');
% title(strcat('\Delta |E_{z}|'));
%
% saveas(h,strcat('Ez_FD_ERR_',num2str(a),'_',num2str(b),'_',polarization,'_
300Pr_35nmZnO_',substrate,'.jpg'));

```

```

%For_Plot.m
Thickness_list=(1:0.1:200);
% load('p-polarized ARC on Poly Silicon');
% R_list_p=R_list;
% load('s-polarized ARC on Poly Silicon');
% R_list_s=R_list;

load('p-polarized ARC on Glass');
R_list_p=R_list;
load('s-polarized ARC on Glass');
R_list_s=R_list;

angle=446; %
% angle=619;
% angle=205;
plot(Thickness_list,R_list_p(:,angle),Thickness_list,R_list_s(:,angle));
xlabel('ARC Thickness (nm)');
ylabel('Reflection Coefficient');
legend('p-polarized','s-polarized');

```

```

%MatrixCal.m
function [B,C,R]=MatrixCal(z,nn_list,ll_list,NNiu_list,wavelength,y,
polarization)
% Give out B,C without phase term for reflection coefficient calculation
if (polarization=='s')
    locator=-sum(ll_list);
    Bs=1.0;
    Cs=y*nn_list(length(nn_list))*cos(NNiu_list(length(NNiu_list))); %
for s polarized light

    Bs_tran=Bs;
    Cs_tran=Cs;
    i=length(ll_list)-1;
    while(locator < z && i>1)

        Ni=nn_list(i);
        di=ll_list(i);
        Niu_i=NNiu_list(i);

        eta_i=y*Ni*cos(Niu_i); % for s polarized light

        delta_i=2*pi*Ni*di*cos(Niu_i)/wavelength;

        M11=cos(delta_i);
        M12=1j*sin(delta_i)/eta_i;
        M21=1j*sin(delta_i)*eta_i;
        M22=cos(delta_i);

        Bs=M11*Bs_tran+M12*Cs_tran;
        Cs=M21*Bs_tran+M22*Cs_tran;

        Bs_tran=Bs;
        Cs_tran=Cs;

        i=i-1;
        locator=locator+di;
    end

    B=Bs;
    C=Cs;
    eta_0=y*nn_list(1)*cos(NNiu_list(1));
    Y=Cs/Bs;
    R=(abs((eta_0*Bs-Cs)/(eta_0*Bs+Cs)))^2;
else
    locator=-sum(ll_list);
    Bs=1.0;
    Cs=y*nn_list(length(nn_list))/cos(NNiu_list(length(NNiu_list))); %
for p polarized light
    Bs_tran=Bs;
    Cs_tran=Cs;
    i=length(ll_list)-1;

```

```

while(locator < z && i>1)

    Ni=nn_list(i);
    di=ll_list(i);
    Niu_i=NNiu_list(i);

    eta_i=y*Ni/cos(Niu_i); % for p polarized light

    delta_i=2*pi*Ni*di*cos(Niu_i)/wavelength;

    M11=cos(delta_i);
    M12=1j*sin(delta_i)/eta_i;
    M21=1j*sin(delta_i)*eta_i;
    M22=cos(delta_i);

    Bs=M11*Bs_tran+M12*Cs_tran;
    Cs=M21*Bs_tran+M22*Cs_tran;

    Bs_tran=Bs;
    Cs_tran=Cs;

    i=i-1;
    locator=locator+di;
end

B=Bs;
C=Cs;
eta_0=y*nn_list(1)/cos(NNiu_list(1));
Y=Cs/Bs;
R=(abs((eta_0*Bs-Cs)/(eta_0*Bs+Cs)))^2;

end
end

```

```

% MatrixCalFD.m
function
[E,n,angle,R]=MatrixCalFD(z,nn_list,ll_list,NNiu_list,wavelength,y,
polarization)
% Give out B,C without phase term for reflection coefficient calculation
if (polarization=='s')

    locator=-(sum(ll_list)-ll_list(length(ll_list)));
    Bs=1.0;
    Cs=y*nn_list(length(nn_list))*cos(NNiu_list(length(NNiu_list))); %
for s polarized light

    Bs_tran=Bs;
    Cs_tran=Cs;
    i=length(ll_list)-1;
    substrate_layer=i+1;

    Ni=nn_list(substrate_layer);
    di=ll_list(substrate_layer);
    Niu_i=NNiu_list(substrate_layer);
    eta_i=y*Ni*cos(Niu_i); % for s polarized light

    while( (locator+ll_list(i)) < z && i>1) %

        Ni=nn_list(i);
        di=ll_list(i);
        Niu_i=NNiu_list(i);

        eta_i=y*Ni*cos(Niu_i); % for s polarized light

        delta_i=2*pi*Ni*di*cos(Niu_i)/wavelength;

        M11=cos(delta_i);
        M12=1j*sin(delta_i)/eta_i;
        M21=1j*sin(delta_i)*eta_i;
        M22=cos(delta_i);

        Bs=M11*Bs_tran+M12*Cs_tran;
        Cs=M21*Bs_tran+M22*Cs_tran;

        Bs_tran=Bs;
        Cs_tran=Cs;

        i=i-1;
        locator=locator+di;
    end

    if ( locator <= z && locator>=(-
sum(ll_list)+ll_list(length(ll_list)))) % && z>=substrate

```

```

        Ni=nn_list(i);
        di=z-locator;
        Niu_i=NNiu_list(i);

        eta_i=y*Ni*cos(Niu_i); % for s polarized light

        delta_i=2*pi*Ni*di*cos(Niu_i)/wavelength;

        M11=cos(delta_i);
        M12=1j*sin(delta_i)/eta_i;
        M21=1j*sin(delta_i)*eta_i;
        M22=cos(delta_i);

        Bs=M11*Bs_tran+M12*Cs_tran;
        Cs=M21*Bs_tran+M22*Cs_tran;
    end
    B=Bs;
    C=Cs;
    %    C/eta_i
    eta_0=y*nn_list(1)*cos(NNiu_list(1));
    Y=Cs/Bs;
    R=(abs((eta_0*Bs-Cs)/(eta_0*Bs+Cs)))^2;
    E_plus=0.5*(C/eta_i+B);
    E_minus=0.5*(-C/eta_i+B);
    E=[E_plus,E_minus];
    n=Ni;
    angle=Niu_i;
else
    locator=-(sum(ll_list)-ll_list(length(ll_list)));
    Bs=1.0;
    Cs=y*nn_list(length(nn_list))/cos(NNiu_list(length(NNiu_list))); %
for p polarized light

    Bs_tran=Bs;
    Cs_tran=Cs;
    i=length(ll_list)-1;
    substrate_layer=i+1;

    Ni=nn_list(substrate_layer);
    di=ll_list(substrate_layer);
    Niu_i=NNiu_list(substrate_layer);
    eta_i=y*Ni/cos(Niu_i); % for p polarized light

    while( (locator+ll_list(i)) < z && i>1) %

        Ni=nn_list(i);
        di=ll_list(i);
        Niu_i=NNiu_list(i);

        eta_i=y*Ni/cos(Niu_i); % for p polarized light

```

```

        delta_i=2*pi*Ni*di*cos(Niu_i)/wavelength;

        M11=cos(delta_i);
        M12=1j*sin(delta_i)/eta_i;
        M21=1j*sin(delta_i)*eta_i;
        M22=cos(delta_i);

        Bs=M11*Bs_tran+M12*Cs_tran;
        Cs=M21*Bs_tran+M22*Cs_tran;

        Bs_tran=Bs;
        Cs_tran=Cs;

        i=i-1;
        locator=locator+di;
    end

    if ( locator <= z  && locator>=(-
sum(ll_list)+ll_list(length(ll_list)))) % && z>=substrate

        Ni=nn_list(i);
        di=z-locator;
        Niu_i=NNiu_list(i);

        eta_i=y*Ni/cos(Niu_i); % for p polarized light

        delta_i=2*pi*Ni*di*cos(Niu_i)/wavelength;

        M11=cos(delta_i);
        M12=1j*sin(delta_i)/eta_i;
        M21=1j*sin(delta_i)*eta_i;
        M22=cos(delta_i);

        Bs=M11*Bs_tran+M12*Cs_tran;
        Cs=M21*Bs_tran+M22*Cs_tran;
    end
%     Ni
    B=Bs;
    C=Cs;
%     C/eta_i
    eta_0=y*nn_list(1)*cos(NNiu_list(1));
    Y=Cs/Bs;
    R=(abs((eta_0*Bs-Cs)/(eta_0*Bs+Cs)))^2;
    E_plus=0.5*(C/eta_i+B);
    E_minus=0.5*(-C/eta_i+B);
    E=[E_plus,E_minus];
    n=Ni;
    angle=Niu_i;

end
end

```

```

% MatrixReflectionCal.m

%Xiang Ji
%xji3@ncsu.edu
%Code written for thin film reflectance calculation
%All rights reserved 2013

clear;clc;
n_ZnO=2.47464; % @ 355nm
n_Si=4.64682; % amorphous silicon @ 355nm
n_Si_poly=5.55336-2.5515i; % polycrystal silicon @ 355nm
n_Pr=1.7123-0.0358i; % AZ5214E @ 365nm unbleached
n_Glass=1.5513; % HT Glass @ 355nm
n_ARC=1.72-0.33i; % WIDE-15B ARC from Brewer Science

sub_list=[n_Si,n_Si_poly,n_Glass];
pol_list=['p','s'];

for sub_counter=1:length(sub_list)
n_list=[1.0,n_ARC,sub_list(sub_counter)]; %start with n_list(1) = 1.0 as
outside layer, air here
    for pol_counter=1:length(pol_list)
        polarization=pol_list(pol_counter); % define polarization: p/s

ZnO_Thickness_list=(1:0.1:200);

incident_list=1:0.1:90; % used to store incident angles
R_list=ones(length(ZnO_Thickness_list),length(incident_list)); % store
reflection coefficient for each angle

lamda=355.0e-9; % unit in m

y_optical_admittance=2.654419E-3; % unit in SI

k=length(n_list)-1;
% q=(k+1)*ones(length(theta_incident)); %used to locate where internal
'full' reflection happens
for thickness_counter=1:length(ZnO_Thickness_list)
    l_list=[0.0,ZnO_Thickness_list(thickness_counter),10.0]*1e-9; % unit
in m
    for angle_counter=1:length(incident_list)
        theta_incident=incident_list(angle_counter)/180.0*pi;
        theta_list=[theta_incident]; % used to store angles in each layer
        for it = 1:k
            if n_list(it)*sin(theta_list(it))>n_list(it+1)
                q=it; %need to change
            else

```

```

        theta = asin(n_list(it)*sin(theta_list(it))/n_list(it+1));
%        theta =
asin(real(n_list(1))*sin(theta_list(1))/real(n_list(it+1)));
        theta_list=[theta_list,theta];
    end
end

[Bs,Cs,Ri]=MatrixCal(1.0,n_list,l_list,theta_list,lamda,y_optical_admittan
ce,polarization);
    R_list(thickness_counter,angle_counter)=Ri;
    end
% R=abs()
end

if (n_list(2)==n_ZnO)
    str_a='ZnO';
elseif (n_list(2)==n_ARC)
    str_a='ARC';
end

if (n_list(3)==n_Si_poly)
    str_b='Poly Silicon';
elseif (n_list(3)==n_Si)
    str_b='aSi';
elseif (n_list(3)==n_Glass)
    str_b='Glass';
end

h=figure(1);
imagesc(incident_list,ZnO_Thickness_list,R_list);
colorbar;
axis xy;
axis square;
xlabel('incident angle (deg)');
ylabel(strcat(str_a, ' Thickness (nm)'));
title(strcat(polarization, '-polarized',32,str_a, ' on',32, str_b));
save(strcat(polarization, '-polarized',32,str_a, ' on',32,
str_b, '.mat'), 'R_list');
saveas(h, strcat(polarization, '-polarized',32,str_a, ' on',32,
str_b, '.jpg'));

    end
end

```

```

% SingleCal.m

clear;clc;
n_ZnO=2.47464; % @ 355nm
n_Si=4.64682; % amorphous silicon @ 355nm
% n_Si_poly=5.55336-2.5515i; % polycrystal silicon @ 355nm
n_Si_poly=5.6573-3.0176i; % polycrystal silicon @ 355nm
n_Pr=1.7123-0.0358i; % AZ5214E @ 365nm unbleached
n_Glass=1.5513; % HT Glass @ 355nm
n_ARC=1.72-0.33i; % WIDE-15B ARC from Brewer Science

n_list=[1.0,n_Pr,n_ZnO,n_Si_poly];
l_list=[40.0,300.0,35.0,100.0]*1e-9;
lamda=355.0e-9; % unit in m
y_optical_admittance=2.654419E-3; % unit in SI
k=length(n_list)-1;

Rs_list=[];
Rp_list=[];
incident_list=1:0.1:89;

for incident_counter=1:1:length(incident_list)

    theta_incident=incident_list(incident_counter)/180.0*pi;
    theta_list=[theta_incident]; % used to store angles in each layer
    for it = 1:k
        if n_list(it)*sin(theta_list(it))>n_list(it+1)
            q=it; %need to change
        else
            theta = asin(n_list(it)*sin(theta_list(it))/n_list(it+1));
            %
            theta =
            asin(real(n_list(1))*sin(theta_list(1))/real(n_list(it+1)));
            theta_list=[theta_list,theta];
        end
    end
    polarization='s';

    [Bs,Cs,Ri]=MatrixCal(1.0,n_list,l_list,theta_list,lamda,y_optical_admittan
ce,polarization);
    Rs_list=[Rs_list,Ri];

    polarization='p';

    [Bs,Cs,Ri]=MatrixCal(1.0,n_list,l_list,theta_list,lamda,y_optical_admittan
ce,polarization);
    Rp_list=[Rp_list,Ri];
end

load('G:\Dropbox\My Files\thesis\FDTD Results\For Thesis\on

```

```

ZnO\Final\Rs_list_s_35nmZnO.mat');
load('G:\Dropbox\My Files\thesis\FDTD Results\For Thesis\on
ZnO\Final\Rs_list_p_35nmZnO.mat');
load_incident=1:length(Rp_list1);

h=figure(1);
plot(incident_list, Rs_list, load_incident, Rs_list1, '--
g+', load_incident, Rs_list2, '-.rx');
legend('Calculation result', 'FDTD Rs1', 'FDTD Rs2', 2);
title('s-polarized reflection coefficient');
axis xy;
% axis square;
xlabel('incident angle (deg)');
ylabel('Reflection Coefficient');
save('Rs_300Pr_35nmZnO_polySi', 'Rs_list');
saveas(h, 'Rs_300Pr_35nmZnO_polySi.jpg');

h=figure(2);
plot(incident_list, Rp_list, load_incident, Rp_list1, '--
g+', load_incident, Rp_list2, '-.rx');
legend('Calculation result', 'FDTD Rp1', 'FDTD Rp2', 2);
title('p-polarized reflection coefficient');
xlabel('incident angle (deg)');
ylabel('Reflection Coefficient');
axis xy;
% axis square;
save('Rp_300Pr_35nmZnO_polySi', 'Rp_list');
saveas(h, 'Rp_300Pr_35nmZnO_polySi.jpg');

```